

# HERA Accelerator Studies 2000

Edited by G. H. Hoffstaetter

With Contributions from

DESY:	F. Brinker,	W. Decking,	K. Ehret,
M. Funcke,	E. Gianfelice,	S. Herb,	G. H. Hoffstaetter,
U. Hurdelbrink,	W. Kriens,	C. Montag,	F. Stulle,
E. Vogel,	M. Werner,	A. Xiao,	
CERN:	H. Burkhardt,	F. Schmidt,	R. Tomás,
BNL:	W. Fischer		

November 2000

## Abstract

The HERA accelerator study periods during 2000 were mainly concerned with issues of the luminosity upgrade project and with close investigations of the proton ring. The luminosity upgrade was already an important subjects during the accelerator studies of December 1998 [9] and during the year 1999 [7].

It is planned to reduce the horizontal electron emittance from the current  $41\pi\text{nm}$  to  $22\pi\text{nm}$  during the luminosity upgrade by increasing the RF frequency by about 300Hz and by using a  $72^\circ$  optics. While the luminosity in such an optics was initially too small, luminosity scans indicated that a too large vertical electron beam size limited the luminosity. Decoupling by a vertical closed orbit bump through sextupoles and a minimization of the vertical dispersion then lead to improved luminosity scans and to a satisfactory luminosity for the  $72^\circ$  optics. To estimate the effect of the increased beam-beam forces on the electron beam after the luminosity upgrade, several optics with  $72^\circ$  degrees phase advance per FODO cell but with different beta functions at the interaction points were used to establish luminosity. It turned out that the beam-beam force should not diminish the luminosity for the luminosity upgrade parameters. While increasing the luminosity by the mentioned emittance reduction schemes, the electron beam polarization should not be reduced. Therefore the change of polarization with an RF shift was investigated and a spin matched  $72^\circ$  optics was used to store a polarized beam with up to 65% polarization.

The interaction rates in the HERA-B wires strongly depends on the position of the wires. In order to reduce this sensitivity, it was investigated whether the tails of the proton beam could be populated without a reduction of the luminosity by applying tune modulations to HERA-p. For the first time a transverse bunched beam echo was detected at HERA-p by measurements of the longitudinal oscillation amplitude and of bunch length oscillations in the proton beam. The following other studies with HERA-p were performed in a collaboration with CERN: The dynamic aperture and the detuning of the proton ring was investigated since such a measurement can yield valuable insight for the LHC. In a realistic accelerator synchrotron radiation at low frequencies is suppressed due to shielding by the beam pipe. To study this shielding effect, the energy loss of a low energetic coasting proton beam was measured.

## Contents

<b>1 Observations about the HERA Luminosity</b>	<b>5</b>
1.1 Luminosity for Different Beta Functions for 60° Optics . . . . .	5
1.2 Luminosity with One and Two Interaction Points . . . . .	6
1.3 Luminosity with Different $\beta_y^e$ for 72° Optics . . . . .	7
1.4 Luminosity for Different Proton Bunch Currents . . . . .	8
<b>2 Luminosity Scans for a 60° and a 72° Optics</b>	<b>12</b>
2.1 Luminosity Scans for Beam Size Determination . . . . .	12
2.2 Influence of the Beam–Beam Force . . . . .	14
2.3 Luminosity Scan for the 60° Optics . . . . .	16
2.4 Luminosity Scan for the 72° Optics . . . . .	20
2.5 Size of the Photon Spot in the Luminosity Detectors . . . . .	23
<b>3 Luminosity Scans for a 72° Optics</b>	<b>25</b>
3.1 Improved Luminosity Scans . . . . .	25
3.2 Two Luminosity Scans for the H1 Interaction Point . . . . .	27
3.3 Luminosity Scan for the ZEUS Interaction Point . . . . .	29
3.4 Size of the Photon Spot in the Luminosity Detectors . . . . .	31
<b>4 Measurement of beam Polarization in a 72°/72° optics</b>	<b>33</b>
4.1 Introduction . . . . .	33
4.2 May measurements . . . . .	34
4.3 August measurements . . . . .	35
4.4 Conclusions . . . . .	36
<b>5 Beam Lifetime versus RF Voltage at HERA-e</b>	<b>37</b>
<b>6 Simultaneous Global Orbit and Dispersion Correction</b>	<b>40</b>
6.1 Correction Method . . . . .	40
6.2 Measurement of Dispersion Function . . . . .	40
6.3 Correction of the Dispersion and Orbit . . . . .	41
<b>7 Orbit Effect of a Misaligned Magnet Girder</b>	<b>46</b>
7.1 Introduction . . . . .	46
7.2 Measurements . . . . .	48
7.3 Analysis . . . . .	49
<b>8 Measurement of the Beam Response Matrix of HERA-e</b>	<b>51</b>
8.1 Linear closed orbit fitting . . . . .	51
8.2 Measured transport matrix: $m_{11}$ and $m_{12}$ . . . . .	52
<b>9 Systematic Tune Modulation Frequency Scans</b>	<b>56</b>
9.1 Introduction . . . . .	56
9.2 Experiments . . . . .	56
9.3 Conclusion . . . . .	57

9.4 Acknowledgments . . . . .	61
<b>10 Bunched Beam Echoes in HERA-p</b>	<b>62</b>
10.1 Introduction . . . . .	62
10.2 RF Kick Production . . . . .	63
10.2.1 52 MHz RF-System . . . . .	63
10.2.2 208 MHz RF-System . . . . .	65
10.3 Measurement of Beam Properties . . . . .	67
10.3.1 Single Bunch Phase and Length . . . . .	67
10.3.2 Timing . . . . .	68
10.3.3 Errors of Measured Signals . . . . .	69
10.4 Observed Beam Echoes . . . . .	69
10.5 First Analysis . . . . .	73
10.5.1 Landau Damping . . . . .	73
10.5.2 Echo Strength over $\Delta t$ . . . . .	74
10.5.3 Echo Strength over RF Noise . . . . .	77
10.6 Conclusion . . . . .	78
<b>11 Multi Bunch Oscillations at Different Fill Patterns of HERA-p</b>	<b>79</b>
11.1 Supplying Different Fill Patterns . . . . .	79
11.2 Performed Measurement . . . . .	80
11.3 Results . . . . .	81
<b>12 Dynamic Aperture and Resonant Terms at HERA-p</b>	<b>83</b>
12.1 Introduction . . . . .	83
12.1.1 Participants in the experiment . . . . .	84
12.2 HERA-p Experiment . . . . .	84
12.3 Realistic model of HERA-p . . . . .	89
12.3.1 $\beta$ -beating . . . . .	89
12.3.2 Detuning . . . . .	91
12.4 Discussion of results . . . . .	93
12.4.1 Dynamic aperture study . . . . .	93
12.4.2 Resonant terms . . . . .	95
12.5 Conclusion . . . . .	96
<b>13 Energy Loss Measurement at HERA-p</b>	<b>97</b>
13.1 Introduction . . . . .	97
13.2 Schottky Signal Detection . . . . .	97
13.3 Beam Preparation . . . . .	98
13.4 Revolution Frequency Measurement . . . . .	98
13.5 Dipole Field Measurement . . . . .	98
13.6 Beam Energy Loss . . . . .	99
13.7 Conclusion . . . . .	100

# 1 Observations about the HERA Luminosity

by G. H. Hoffstaetter, DESY Hamburg

Date: 1999, Dec. 17, 3pm to Dec. 18, 1am, Logbook XXXXI, p. 55–60

Date: 1999, Dec. 18, 7am to Dec. 18, 11pm, Logbook XXXXI, p. 70–73

Date: 2000, Aug. 31, 6am to Aug. 31, 3pm, Logbook XLV, p. 60–68

In the luminosity upgrade project for HERA, the beta functions of both beams will be reduced and the currents are planned to be increased. These measures will increase the beam-beam tune shift parameters from  $\Delta\nu_x/\Delta\nu_y$  from 0.012/0.03 to 0.034/0.051 [1, 2]. To find out whether a luminosity reduction due to the increased tune shift has to be expected, several experiments were performed to test whether the luminosity at HERA’s current parameters suffers from the beam-beam force on the electrons. To investigate this, the beam-beam tune shift was varied by choosing different beta functions for a 60° optics, by running with one or with two interaction points, and by colliding positron bunches with different proton bunch currents. None of the presented measurements establishes that the specific luminosity in HERA is currently restricted by the beam-beam force on the electrons.

Since the increased vertical tune shifts did not seem to increase the electron emittances during the accelerator studies in December 1999, new studies were performed in August 2000 where the tune shift was increased dramatically for a 72° optics in order to see when the emittances start to suffer. Since the proton current can not easily be increased and the proton beta functions can hardly be decreased, we chose to increase the beam-beam tune shift of the electrons by increasing the beta functions of the electrons from 0.7 m up to 4 m.

## 1.1 Luminosity for Different Beta Functions for 60° Optics

In order to find out whether the  $e^+$  beam suffers from a too large beam-beam tune shift, luminosity was established for different  $e^+$  beta functions. Table 1.1 shows the specific luminosity  $\mathcal{L}_s^{ZEUS}$  obtained at ZEUS when the beams were not brought into collision in the H1 experiment. The luminosity was recorded for three HERA-e optics with 60° phase advance per FODO cell, each having different beta functions at the interaction point. The proton emittances were obtained with the wire scanner to be  $4\beta\gamma\epsilon_x^p = 18$  mm mrad and  $4\beta\gamma\epsilon_y^p = 13$  mm mrad and the proton current was 76 mA. The nominal beta functions of HERA-p were  $\beta_x^p = 7$  m and  $\beta_y^p = 0.5$  m. The specific luminosity in the optics with  $\beta_x^e = 1.0$  m is scaled to the other beta

$\beta_x^e$	$\beta_y^e$	$\mathcal{L}_s^{ZEUS}$	$\mathcal{L}_s(\beta_x^e, \beta_y^e)$	$\Delta\nu_x^e$	$\Delta\nu_y^e$
0.9m	0.6m	$7.1 \cdot 10^{29}$	$7.10 \cdot 10^{29}$	-0.0106	-0.0311
1.0m	0.7m	$6.78 \cdot 10^{29}$	$6.67 \cdot 10^{29}$	-0.0118	-0.0363
2.2m	0.9m	$5.18 \cdot 10^{29}$	$4.84 \cdot 10^{29}$	-0.0259	-0.0467

**Table 1.1:** The luminosity for different beta functions at the interaction point.

functions by

$$\mathcal{L}_s(\beta_x^e, \beta_y^e) = \mathcal{L}_s^{ZEUS}(1.0m, 0.7m) \frac{\sqrt{\beta_x^p \epsilon_x^p + \epsilon_x^e 1.0m}}{\sqrt{\beta_x^p \epsilon_x^p + \epsilon_x^e \beta_x^e}} \frac{\sqrt{\beta_y^p \epsilon_y^p + \epsilon_y^e 0.7m}}{\sqrt{\beta_y^p \epsilon_y^p + \epsilon_y^e \beta_y^e}}. \quad (1.1)$$

This scaling is expected when the change of the  $e^+$  beam size is only due to the change of the beta function and not due to a blowup of the emittances. The expected luminosities are recorded in table 1.1 for the nominal horizontal emittance  $\epsilon_x^e$  of 41nm and a vertical emittance  $\epsilon_y^e = \epsilon_x^e/20$  as obtained in equation (2.29). The resulting beam-beam tune shift parameters  $\Delta\nu_x^e$  and  $\Delta\nu_y^e$  are also shown. The luminosity does not decrease as strongly as expected with the increasing beta function. While this discrepancy is not yet understood, these measurements certainly do not give a reason to expect that the  $e^+$  emittances increased with increasing beam-beam tune shifts.

## 1.2 Luminosity with One and Two Interaction Points

To check whether the specific luminosity  $\mathcal{L}_s$  diminishes with increasing beam-beam tune shift,  $\mathcal{L}_s$  was measured at the ZEUS detector for a maximized luminosity at the H1 detector and then with separated beams in the H1 experiment. This was done for the three different  $60^\circ$  optics used in section 1.1 which all have different beta functions at the interaction point. The resulting specific luminosities are shown in table 1.2. The differences could be due to the change in the beta function in the ZEUS detector due to the beam-beam force at the H1 interaction point. To test this hypothesis, the specific luminosity  $\mathcal{L}_s^{ZEUS}(\Delta\Phi)$  was computed which would be expected at the ZEUS interaction point when the betatron phase advance to the H1 interaction point was given by  $\Delta\Phi$ ,

$$\mathcal{L}_s^{ZEUS}(\Delta\Phi) = \mathcal{L}_s^{ZEUS \text{ only}} \frac{\sqrt{\beta_x^p \epsilon_x^p + \beta_{x0}^e \epsilon_x^e}}{\sqrt{\beta_x^p \epsilon_x^p + \beta_x^e(\Delta\Phi) \epsilon_x^e}} \frac{\sqrt{\beta_y^p \epsilon_y^p + \beta_{y0}^e \epsilon_x^e}}{\sqrt{\beta_y^p \epsilon_y^p + \beta_y^e(\Delta\Phi) \epsilon_x^e}}, \quad (1.2)$$

$$\beta_{x0}^e = \beta_x^e \left\{ 1 - \frac{2\pi\Delta\nu_x^e}{\sin(2\pi Q_x^e)} \cos(2\pi Q_x^e) \right\}, \quad (1.3)$$

$$\beta_x^e(\Delta\Phi) = \beta_x^e \left\{ 1 - \frac{2\pi\Delta\nu_x^e}{\sin(2\pi Q_x^e)} [\cos(2\pi Q_x^e) + \cos(2|\Delta\Phi| - 2\pi Q_x^e)] \right\} \quad (1.4)$$

and correspondingly for the vertical beta functions, where  $\beta_x^e$  is the beta function for the nominal optics without the beam-beam focusing. Note that  $\Delta\nu_x^e$  and  $\Delta\nu_y^e$

$\beta_x^e$	$\beta_y^e$	$\mathcal{L}_s^{ZEUS}$			$\Delta\nu_x^e$	$\Delta\nu_y^e$
		(without H1)	(with H1)	$\Delta\Phi \in [0, 2\pi]$		
0.9m	0.6m	$7.1 \cdot 10^{29}$	$7.0 \cdot 10^{29}$	$[7.00, 7.20] \cdot 10^{29}$	0.0106	0.0311
1.0m	0.7m	$6.78 \cdot 10^{29}$	$7.0 \cdot 10^{29}$	$[6.67, 6.89] \cdot 10^{29}$	0.0118	0.0363
2.2m	0.9m	$5.18 \cdot 10^{29}$	$5.5 \cdot 10^{29}$	$[4.97, 5.42] \cdot 10^{29}$	0.0259	0.0467

**Table 1.2:** The luminosity for different beta functions at the interaction point.

are the beam-beam tune shift parameters of one interaction point. The proton emittances were obtained with the wire scanner to be  $4\beta\gamma\epsilon_x^p = 18$  mm mrad and  $4\beta\gamma\epsilon_y^p = 13$  mm mrad and the proton current was 76 mA. The nominal beta functions of HERA-p were  $\beta_x^p = 7$  m and  $\beta_y^p = 0.5$  m. One concludes that the increased beam-beam tune shift due to the second interaction point does not seem to reduce the specific luminosity. On the contrary, an increase can be observed which can be due to the beating of the beta function which is induced by the beam-beam force at H1.

### 1.3 Luminosity with Different $\beta_y^e$ for 72° Optics

Since bigger  $e^+$  beta functions lead to an increased electron spot sized at the interaction point, the proton beam sizes are no longer matched when the beam-beam tune shift is increased by increasing the beta functions. To diminish this mismatch, the optics with increased beta functions had 72° focusing in the arcs and nominal emittances of  $\epsilon_x^e = 32$  nm. The luminosity was optimized by varying the decoupling bump, which lead to a emittance coupling of less than 10% according to section 3.

With a proton current of 90mA, a specific luminosity of  $\mathcal{L}_s = 8.8 \cdot 10^{29} \text{ cm}^{-2} \text{ mA}^{-2}$  was reached for a spin matched 72° optics with  $\beta_x^e = 1$  m and  $\beta_y^e = 0.7$  m. The proton emittance was not measured but  $\epsilon_x^p = 15\pi$  mm mrad,  $\epsilon_y^p = 12.5\pi$  mm mrad would lead to this luminosity. Then five different optics with  $\beta_x^e = 2.5$  m,  $\beta_x^e \in 1, 1.5, 2, 3, 4$  m were installed with separated beams at the interaction points and then luminosity was established and optimized for each of these optics. The value of  $\beta_x^e = 2.5$  m was chosen for each of these optics since the corresponding horizontal beam-beam tune shift of  $2\Delta\nu_x^e = 0.082$  is slightly higher than expected for the design proton current of 140mA after the luminosity upgrade. Figure 1.1 shows the luminosity which was achieved at ZEUS for the different  $\beta_y^e$ . The fitted curve does not take into account the optics with  $\beta_y^e = 0.7$  m since this optic has  $\beta_x^e = 1$  m rather than  $\beta_x^e = 2.5$  m as in the other cases. This figure shows also that the luminosity would be significantly larger than what was measured when the beam-beam force is not taken into account.

There can be several reasons for this decrease of the specific luminosity. The electron spot size could have increased due to a blowup of the emittance produced by the beam-beam force, the spot size could also have changed due to a beam-beam beta beat at the interaction point or due to a non Gaussian beam distribution caused by the strongly nonlinear beam-beam potential. To evaluate the change in the spot size, it was assumed that the beta function is unchanged and the photon spot at

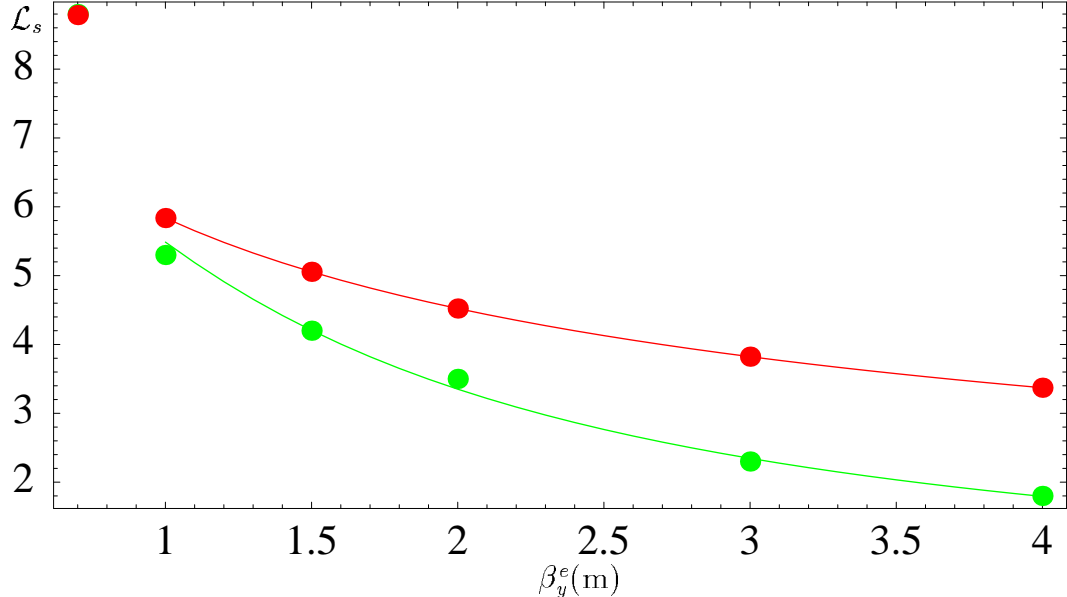


**Figure 1.1:** Bottom (green): The specific luminosity  $\mathcal{L}_s$  in units of  $10^{29} \text{ cm}^{-2} \text{ mA}^{-2}$  for six optics with different beta functions. Top (red): Computed specific luminosity when the beam-beam effect is not taken into account.

the luminosity monitors of H1 and ZEUS was used to determine the emittances according to the formula of section 3.4. The emittances measured at H1 and ZEUS are shown in figure 1.2 and a fit to the average of the two measurements is also shown.

To study whether this strong vertical emittance blowup is responsible for the measured decrease of specific luminosity with increasing  $\beta_y^e$ , figure 1.3 shows the measured luminosity together with the luminosity which is computed for the emittance  $\epsilon_y^e$  of figure 1.2. Since this computation matches the measured luminosity much better, the decrease of luminosity seems to be mainly due to a beam-beam force driven increase of the vertical emittance.

The huge increase of  $\epsilon_y^e$  by up to a factor 8 is due to the enormous linear tune shift produced by the two experiments which is shown in figure 1.4. In fact it is quite astonishing that the electron beam could at all be stored with such large tune shifts. While the luminosity had to be very carefully optimized to avoid beam loss, the lifetime was 2 to 4 hours even at the highest  $\beta_y^e$  of 4m.

## 1.4 Luminosity for Different Proton Bunch Currents

A significant dependence of the specific luminosity on the proton current might hint at a beam-beam force induced increase of the  $e^+$  emittance. To test whether such a dependence exists at the current HERA parameters, the specific luminosity at H1 for each bunch pair was plotted against the proton bunch current in figure 1.5. The bunch by bunch specific luminosity is displayed for each luminosity run of the first four months of the year 2000, where for each run the data were taken shortly after

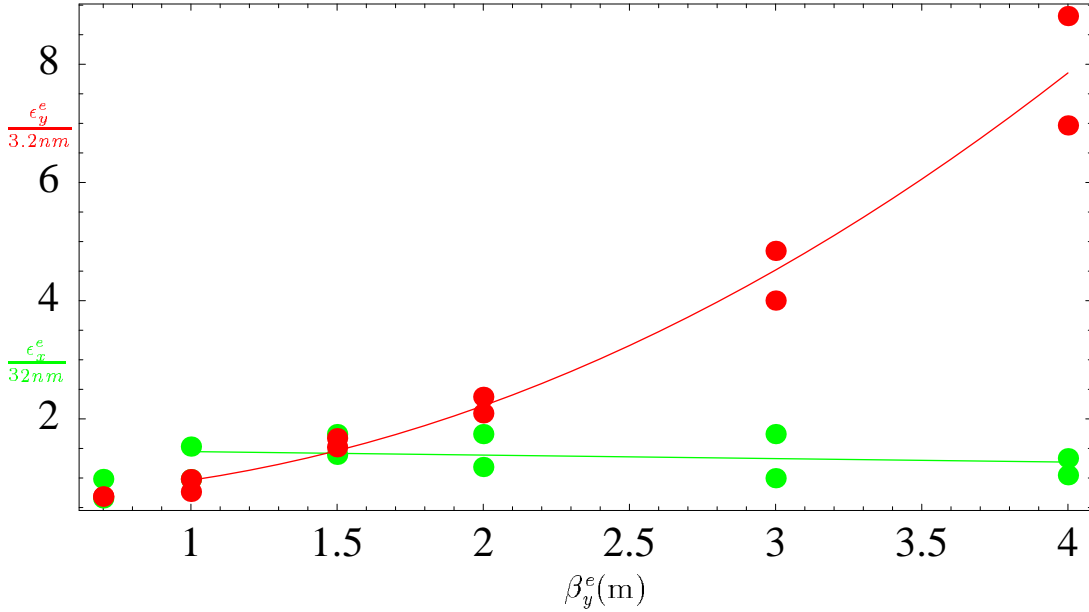


**Figure 1.2:** Top (red): The vertical emittance relative to the computed value of 3.2nm. Bottom (green): The horizontal emittance relative to the computed value of 32nm. While  $\epsilon_x^e$  does not seem to change much, the vertical emittance is blown up by up to a factor of 8.

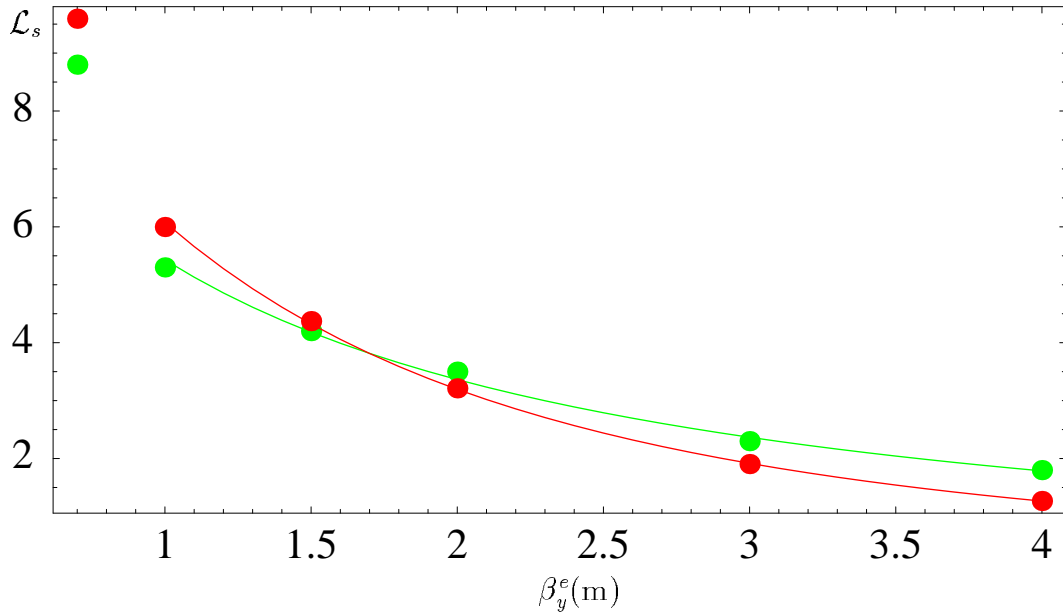


**Figure 1.3:** Top (green): The specific luminosity  $\mathcal{L}_s$  in units of  $10^{29} \text{ cm}^{-2}\text{mA}^{-2}$  for six optics with different beta functions. Bottom (red): Computed specific luminosity when the vertical emittance measured by the photon spot at the luminosity monitors is taken into account, assuming that the vertical beta function is not changed by the beam-beam force.

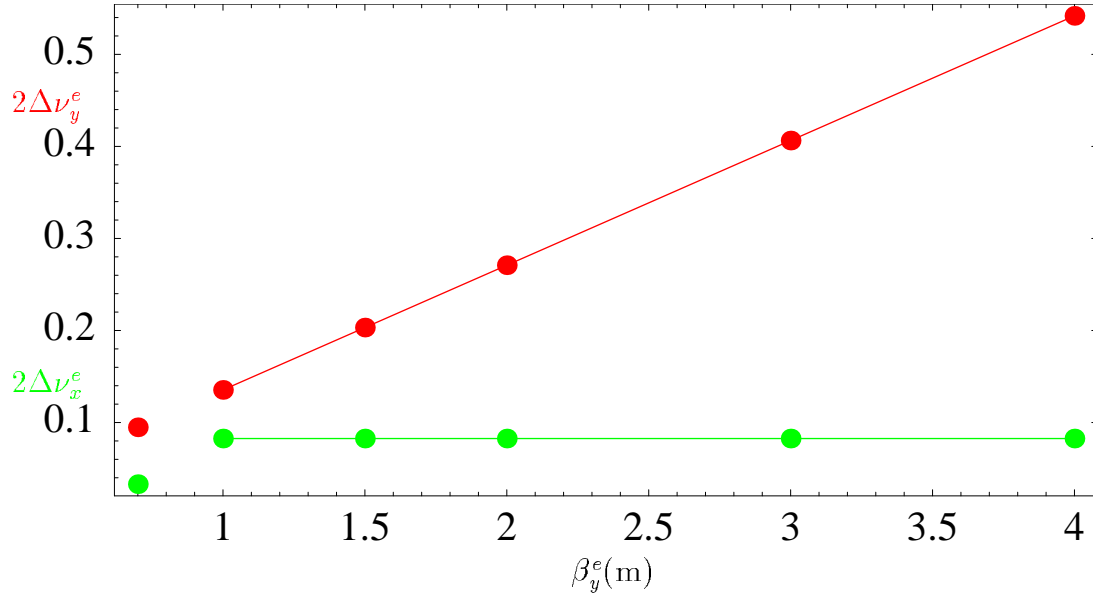


**Figure 1.4:** The computed beam-beam tune shift parameters for the two interaction points for six optics with different beta functions. Top (red): for vertical and Bottom (green) for horizontal motion.

the start of the run. To establish that a beam-beam force induced blowup of the electron beam diminishes the luminosity, a noticeable drop of the luminosity at high proton currents would have to be visible, which is not the case.

It is however interesting to note that some bunches, especially some with relatively low proton currents, have a very high specific luminosity. This could indicate that the normalized proton emittance can be significantly smaller than the average for some transfer conditions which occur only rarely for individual bunches. It turns out that in those cases where an unusually large specific luminosity occurs (or more than 0.00005 in the displayed units), this always happens for the first bunch pair of the 174 colliding bunches. This might, however, be due to an occasional problem in the measurement of the first bunch current. These cases of high specific luminosity are not correlated with extra ordinary large or small electron currents as shown in figure 1.6.

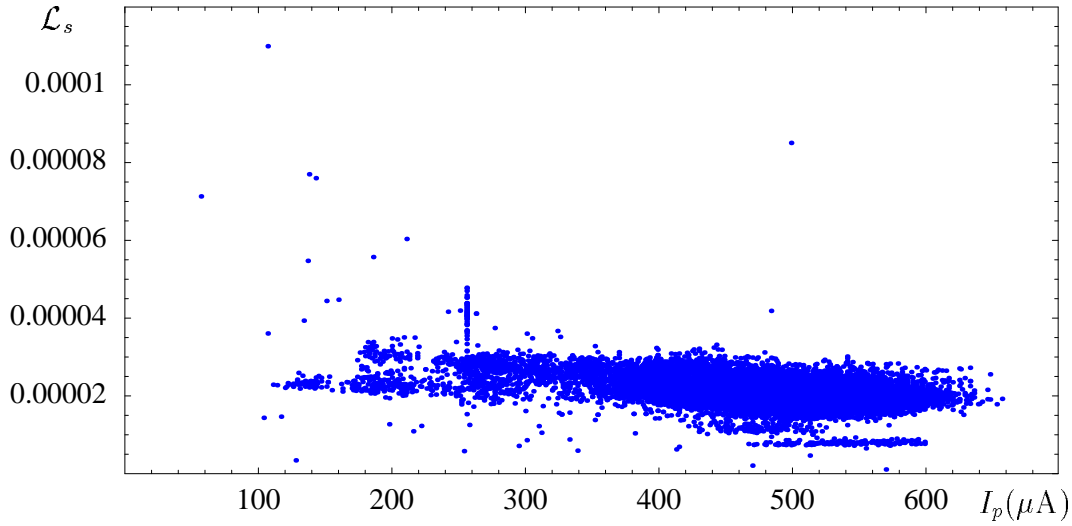


**Figure 1.5:** The specific luminosity  $\mathcal{L}_s$  (arbitrary units) for each colliding bunch against the proton bunch current  $I_p$  ( $\mu\text{A}$ ) as obtained by H1. The data have been taken from e.g. <http://vmepm01.desy.de/y2000/m4/d30/bunch/t23.0BunchParmL> for the year 2000, forth month, 30th day at the time 23:00. These files contain counting rates of the H1 luminosity monitor and have therefore been subsequently corrected for the background signal at non-colliding bunch positions.

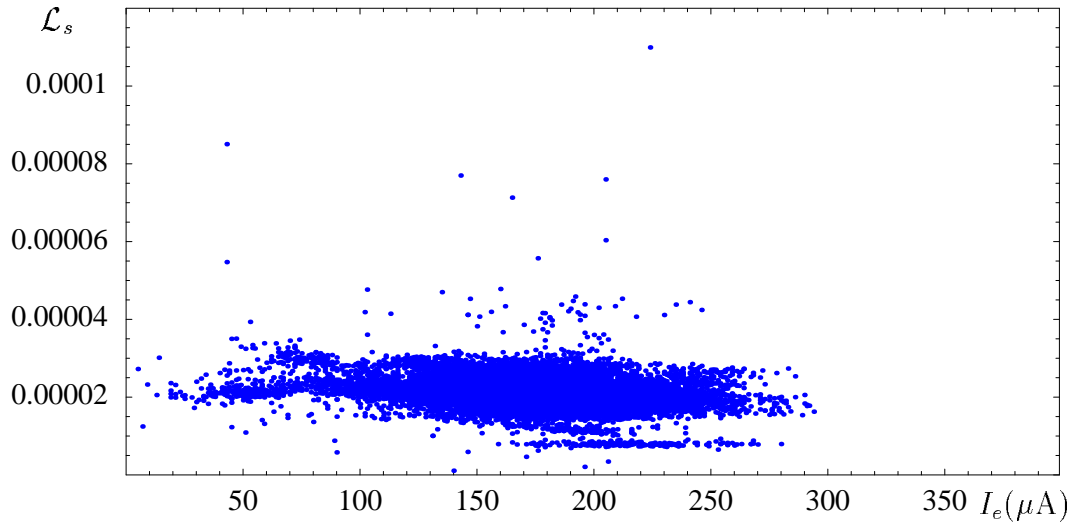


**Figure 1.6:** The specific luminosity (arbitrary units) for each colliding bunch against the electron bunch current  $I_e$  ( $\mu\text{A}$ ) as obtained by H1.

## 2 Luminosity Scans for a 60° and a 72° Optics in HERA-e

by G. H. Hoffstaetter, DESY Hamburg

Date: 1999, Dec. 16, 7am to Dec. 17, 7am, Logbook XXXXI, p. 46–54

Date: 1999, Dec. 18, 2pm to Dec. 18, 11pm, Logbook XXXXI, p. 70–73

It is planned to reduce the horizontal emittance in HERA from currently 41nm during the luminosity upgrade to 22nm [1, 2]. This should be achievable by increasing the RF frequency and the phase advance per FODO cell. A lattice with 72° phase advance per FODO cell in both planes turned out to be most promising because it had the most acceptable dynamic aperture [3] and allows for just the required amount of RF frequency increase.

To test the usability of such an optics in the upgraded HERA-e, a 72° test optic was installed in the current ring and the  $e^+$  and proton beams were brought into luminosity condition. Then the proton beam was shifted with respect to the  $e^+$  beam and the luminosity was recorded as a function of the amplitude of the symmetric bump which shifted the proton beam. While a wire scanner was used to determine the proton beam size, this luminosity scan was used to determine the  $e^+$  emittances. As a reference, a luminosity scan was also produced for the current optics of HERA-e with 60° phase advance per FODO cell.

The beam-beam force acting on the  $e^+$  beam is changed during the luminosity scan. This leads to a varying kick on the  $e^+$  beam and to a varying disturbance to the beta function. These effects are explained and taken into account when determining the emittances of the  $e^+$  beam. The HERA proton beam is assumed to be unaffected by the beam-beam force during the luminosity scan.

### 2.1 Luminosity Scans for Beam Size Determination

The specific luminosity  $\mathcal{L}_s$  for head on collisions of two beams with densities  $\rho_p$  and  $\rho_e$  is given by

$$\mathcal{L}_s = \frac{1}{f q_p q_e} \int_{\infty} \left[ \int_{-\infty}^{\infty} \rho_p(x, y, z) dz \right] \left[ \int_{-\infty}^{\infty} \rho_e(x, y, z) dz \right] dx dy , \quad (2.1)$$

where the circulation frequency  $f$  and the charges  $q_p$  and  $q_e$  of the particles in the two beams have been used. During a luminosity scan, the distance between the center of the two beams is varied. We let the densities  $\rho_p$  and  $\rho_e$  describe a centered beam, i.e.  $\int_{\infty} \vec{r} \rho_i(x, y, z) d\vec{r} = 0$ . Then the luminosity scan in  $x$ -direction is described by

$$\mathcal{L}_s^x(\Delta x) = \frac{1}{f q_p q_e} \int_{\infty} \left[ \int_{-\infty}^{\infty} \rho_p(x, y, z) dz \right] \left[ \int_{-\infty}^{\infty} \rho_e(x - \Delta x, y, z) dz \right] dx dy . \quad (2.2)$$

When  $\bar{\rho}(y) = \int_{-\infty}^{\infty} \rho(x, y, z) dx dz$  is the projected density, the luminosity scan in  $x$  direction gives information about the vertical density:

$$\int_{-\infty}^{\infty} \mathcal{L}_s^x(\Delta x) d\Delta x = \frac{1}{f q_p q_e} \int_{-\infty}^{\infty} \bar{\rho}_p(y) \bar{\rho}_e(y) dy . \quad (2.3)$$

Assuming Gaussian beams for protons:  $\rho_{xp}(x, y, z) = G^{\sigma_{xp}}(x) G^{\sigma_{yp}}(y) \rho_{zp}(z)$ , and equally for electrons, with the following convolution property:

$$G^{\sigma}(x) = \frac{1}{\sqrt{2\pi}\sigma} \exp\left(-\frac{x^2}{2\sigma^2}\right), \quad \int_{-\infty}^{\infty} G^{\sigma_1}(x - \tilde{x}) G^{\sigma_2}(x) dx = G^{\sqrt{\sigma_1^2 + \sigma_2^2}}(\tilde{x}), \quad (2.4)$$

the integral in equation (2.3) evaluates with  $\bar{\rho}_p(y) = G^{\sigma_{yp}}(y)$ ,  $\bar{\rho}_e(y) = G^{\sigma_{ye}}(y)$  to

$$\int_{-\infty}^{\infty} \mathcal{L}_s^x(\Delta x) d\Delta x = \frac{1}{f q_p q_e} \frac{1}{\sqrt{2\pi}(\sigma_{yp}^2 + \sigma_{ye}^2)} . \quad (2.5)$$

A related method which also required integrals over luminosity scans was used at the CERN ISR for luminosity calibration [4, 5]. In the following, two methods will be used to determine the overlap beam sizes  $\Sigma_x = \sqrt{\sigma_{xp}^2 + \sigma_{xe}^2}$  and  $\Sigma_y = \sqrt{\sigma_{yp}^2 + \sigma_{ye}^2}$ .

**Method (a):** The standard deviation  $\langle x^2 \rangle_{\mathcal{L}_s^x}$  of the luminosity scan is obtained by fitting  $a_x$ ,  $b_x$ , and  $c_x$  of a bell curve  $a_x \exp(-b_x(x - c_x)^2)$  to the data. Then one obtains  $\Sigma_x = 1/\sqrt{2b_x}$ . Similarly one obtains  $\Sigma_y = 1/\sqrt{2b_y}$ . Assuming Gaussian beams with the following convolution property:

$$G^{\sigma}(x) = \frac{1}{\sqrt{2\pi}\sigma} \exp\left(-\frac{x^2}{2\sigma^2}\right), \quad \int_{-\infty}^{\infty} G^{\sigma_1}(x - \tilde{x}) G^{\sigma_2}(x) dx = G^{\sqrt{\sigma_1^2 + \sigma_2^2}}(\tilde{x}), \quad (2.6)$$

the luminosity scan data should be approximated by

$$\mathcal{L}_s^x(\Delta x, \Delta y) = \frac{1}{f q_p q_e} \frac{1}{2\pi \Sigma_x \Sigma_y} e^{-\frac{\Delta x}{2\Sigma_x^2}} e^{-\frac{\Delta y}{2\Sigma_y^2}} . \quad (2.7)$$

These curves will be colored green in the following figures.

**Method (b):** It is assumed that both beams have a Gaussian density, which leads to

$$f q_p q_e \int_{-\infty}^{\infty} \mathcal{L}_s^x(\Delta x) d\Delta x = \int_{-\infty}^{\infty} \frac{e^{-\frac{y^2}{2\sigma_{yp}^2}}}{\sqrt{2\pi}\sigma_{yp}} \frac{e^{-\frac{y^2}{2\sigma_{ye}^2}}}{\sqrt{2\pi}\sigma_{ye}} dy = \frac{1}{\sqrt{2\pi} \sqrt{\sigma_{yp}^2 + \sigma_{ye}^2}} . \quad (2.8)$$

In this method, the vertical overlap beam size is obtained from the horizontal luminosity scan with  $\Sigma_y = (\sqrt{2\pi} f q_p q_e \int_{-\infty}^{\infty} \mathcal{L}_s^x(\Delta x) d\Delta x)^{-1}$  and vice versa. The integral is evaluated by fitting  $a_x$ ,  $b_x$ , and  $c_x$  of a bell curve  $a_x \exp(-b_x(x - c_x)^2)$  to the data. Then one obtains  $\Sigma_y = \sqrt{b_x} (\sqrt{2\pi} f q_p q_e a_x)^{-1}$  and similarly  $\Sigma_y = \sqrt{b_x} (\sqrt{2\pi} f q_p q_e a_x)^{-1}$ . Also for these  $\Sigma_x$  and  $\Sigma_y$ , the luminosity scan data should be approximated by equation (2.7). These curves will be colored red in the following figures.

The HERA proton beam size  $\langle x^2 \rangle_p$  is obtained by fitting a Gaussian to wire scanner data. Together with the luminosity scan, the  $e^+$  beam size is then determined.

## 2.2 Influence of the Beam–Beam Force

Here we will consider two effects of the beam–beam force on the luminosity scan. Firstly the beam–beam kick leads to a displacement of the  $e^+$  beam from the proton beam which adds to the displacement which is produced by the symmetric bump during the scan. Secondly the strength of the beam–beam lens changes during the luminosity scan. This leads to a changing beta function and therefore a changing  $e^+$  beam size during the luminosity scan. The beam–beam potential for a Gaussian proton beam with beam sizes  $\sigma_{xp}$  and  $\sigma_{yp}$  at the interaction point is given by [6]

$$U(x, y) = \int_0^\infty \frac{e^{-\frac{x^2}{2(\sigma_{xp}^2+t)} - \frac{y^2}{2(\sigma_{yp}^2+t)}}}{\sqrt{\sigma_{xp}^2 + t} \sqrt{\sigma_{yp}^2 + t}} dt . \quad (2.9)$$

The kick on an  $e^+$  passing the proton beam in the distance  $(x, y)$  from its center is given by  $\delta\vec{r}' = -C_{bb}\partial_r U(x, y)$  with  $C_{bb} = \frac{q_p n_p r_e}{q_e \gamma_e}$ ,  $r_e = 2.8$  fm being the classical electron radius and  $\gamma_e$  being the positrons' relativistic factor. The number of protons in the colliding bunch is given by  $n_p$ .

When the one turn transport matrix without the beam–beam interaction is denoted by  $\underline{M}_0$  and the beam–beam kick  $\Delta x'$  is given, the position and slope deviation at the interaction point satisfy

$$\underline{M} \begin{pmatrix} \delta x \\ \delta x' \end{pmatrix} + \begin{pmatrix} 0 \\ \Delta x' \end{pmatrix} = \begin{pmatrix} \delta x \\ \delta x' \end{pmatrix} , \quad \begin{pmatrix} \delta x \\ \delta x' \end{pmatrix} = (\underline{1} - \underline{M})^{-1} \begin{pmatrix} 0 \\ \Delta x' \end{pmatrix} . \quad (2.10)$$

With the tunes  $Q_x^e$ ,  $Q_y^e$  and the beta functions  $\beta_x^e$ ,  $\beta_y^e$  at the interaction point of the electron ring without beam–beam force, this leads to  $\delta x = \frac{\beta_x^e}{2\tan(\pi Q_x^e)} \Delta x'$ . When the symmetric bump separates the beams by the amount  $\Delta x_0$ , the actual distance  $\Delta x$  between the beams is given by the implicit solution of

$$\Delta x = \Delta x_0 + \delta x = \Delta x_0 - \frac{\beta_x^e}{2\tan(\pi Q_x^e)} C_{bb} \partial_r U(\Delta x, 0) . \quad (2.11)$$

The luminosity scan therefore should not be interpreted as a function of  $\delta$  but as a function of the implicit solution  $\Delta x$  in order to eliminate the effect of the beam–beam kick.

Additionally one can take account of the beam–beam lens and its disturbance of the beta function. This leads to a focusing error at the interaction point which is characterized by  $\delta k_x = -C_{bb}\partial_x^2 U(x, y)$  and  $\delta k_y = -C_{bb}\partial_y^2 U(x, y)$ . In  $x$ -direction, the one turn matrix with beam–beam lens is given by

$$\underline{M} = \begin{pmatrix} 1 & 0 \\ -\frac{\delta k_x}{2} & 1 \end{pmatrix} \underline{M}_0 \begin{pmatrix} 1 & 0 \\ -\frac{\delta k_x}{2} & 1 \end{pmatrix} . \quad (2.12)$$

This leads to  $\text{tr}(M) = \text{tr}(M_0) - \delta k_x M_{012} = 2\cos(2\pi Q_x^e) - \delta k_x \beta_x^e \sin(2\pi Q_x^e)$  and  $M_{12} = M_{012} = \beta_x^e \sin(2\pi Q_x^e)$ . The beta function with the beam–beam lens is then

given by  $\beta_{bbx}^e = M_{12}/\sqrt{1 - [\frac{1}{2}\text{tr}(M)]^2}$  leading to

$$\begin{aligned}\delta\beta_x^e(x, y) &= \frac{\beta_{bbx}^e - \beta_x^e}{\beta_x^e} = \frac{\sin(2\pi Q_x^e)}{\sqrt{1 - [\cos(2\pi Q_x^e) - \frac{\delta k_x}{2}\beta_x^e \sin(2\pi Q_x^e)]^2}} - 1 \\ &= \frac{1}{\sqrt{1 - (\frac{\delta k_x \beta_x^e}{2})^2 + \frac{\delta k_x \beta_x^e}{\tan(2\pi Q_x^e)}}} - 1.\end{aligned}\quad (2.13)$$

After the overlap beam sizes  $\Sigma_x$  and  $\Sigma_y$  have been determined by applying method (a) to the luminosity scan data which has been corrected for the beam–beam kick, one can then use the proton emittances obtained from the wire scanner to compute the  $e^+$  emittances by

$$\epsilon_x^e = \frac{\Sigma_x^2 - \beta_x^p \epsilon_x^p}{\beta_x^e [1 + \delta\beta_x^e(0, 0)]} \quad (2.14)$$

and by the corresponding equation for the  $y$ -direction. For two Gaussian beams with overlap beam sizes  $\Sigma_x$  and  $\Sigma_y$  which do not change during the luminosity scan, equation (2.2) leads to

$$\mathcal{L}_s^x(\Delta x) = \frac{1}{f q_p q_e} \frac{1}{2\pi \Sigma_x \Sigma_y} e^{-\frac{\Delta x^2}{2\Sigma_x^2}}. \quad (2.15)$$

Assuming the  $e^+$  emittances from equation (2.14) to be invariant during the luminosity scan, but taking the varying beam–beam lens into account therefore leads to

$$\mathcal{L}_s^x(\Delta x) = \frac{1}{f q_p q_e} \frac{1}{\Sigma_x(\Delta x) \Sigma_y(\Delta x)} \exp\left(-\frac{\Delta x^2}{2\Sigma_x(\Delta x)^2}\right), \quad (2.16)$$

$$\Sigma_x(\Delta x) = \sqrt{\epsilon_x^p \beta_x^p + \epsilon_x^e \beta_x^e [1 + \delta\beta_x^e(\Delta x, 0)]}, \quad (2.17)$$

$$\Sigma_y(\Delta x) = \sqrt{\epsilon_y^p \beta_y^p + \epsilon_y^e \beta_y^e [1 + \delta\beta_y^e(\Delta x, 0)]}. \quad (2.18)$$

This difference between the plain Gaussian luminosity scan curve and equation (2.18) is not taken into account when fitting a Gaussian to luminosity scan data. To correct for the difference between equation (2.15) and (2.18), this difference is subtracted from the specific luminosity data. The obtained data points which are now corrected for the beam–beam kick and for the beam–beam lens should be described better by a Gaussian than the original data. Finally the standard deviation of the Gaussian fitted to these manipulated data points is used to compute the overlap beam sizes by the methods (a).

The beam–beam forces and the strength of the beam–beam lens will now be computed. With  $\Delta = \sigma_x^2 - \sigma_y^2$  and  $\sigma_x > \sigma_y$  one obtains the following derivatives of the beam–beam potential in equation (2.9) which will be used to determine the

beam-beam kicks and the varying beta functions:

$$\partial_x U|_{y=0} = -x \int_0^\infty \frac{e^{-\frac{x^2}{2(\sigma_{xp}^2+t)}}}{\sqrt{\sigma_{xp}^2+t}} dt . = -x \int_0^{\frac{1}{\sigma_x^2}} \frac{e^{-\frac{x^2}{2}t}}{\sqrt{1-t\Delta}} dt \quad (2.19)$$

$$= -\frac{x}{\Delta} e^{-\frac{x^2}{2\Delta}} \int_{\frac{\sigma_y^2}{\sigma_x^2}}^1 \frac{e^{\frac{x^2}{2\Delta}t}}{\sqrt{t}} dt = -2\sqrt{\frac{2}{\Delta}} e^{-\frac{x^2}{2\Delta}} \int_{\frac{x}{\sqrt{2\Delta}} \frac{\sigma_y}{\sigma_x}}^{\frac{x}{\sqrt{2\Delta}}} e^{t^2} dt . \quad (2.20)$$

With the error function  $\text{erf}(x) = \frac{2}{\sqrt{\pi}} \int_0^x \exp(-x^2) dx$  and with  $\text{erfi}(x) = \frac{2}{\sqrt{\pi}} \int_0^x \exp(x^2) dx$  this leads to

$$\begin{aligned} \partial_x U|_{y=0} &= -\sqrt{\frac{2\pi}{\Delta}} e^{-\frac{x^2}{2\Delta}} [\text{erfi}(\frac{x}{\sqrt{2\Delta}}) - \text{erfi}(\frac{x}{\sqrt{2\Delta}} \frac{\sigma_y}{\sigma_x})] , \\ \partial_x^2 U|_{y=0} &= \sqrt{\frac{2\pi}{\Delta}} \frac{x}{\Delta} e^{-\frac{x^2}{2\Delta}} [\text{erfi}(\frac{x}{\sqrt{2\Delta}}) - \text{erfi}(\frac{x}{\sqrt{2\Delta}} \frac{\sigma_y}{\sigma_x})] - \frac{2}{\Delta} [1 - e^{-\frac{x^2}{2\sigma_x^2}} \frac{\sigma_y}{\sigma_x}] \quad (2.21) \\ \partial_y U|_{y=0} &= 0 , \end{aligned}$$

$$\begin{aligned} \partial_y^2 U|_{y=0} &= - \int_0^{\frac{1}{\sigma_x^2}} \frac{e^{-\frac{x^2}{2}t}}{\sqrt{1-t\Delta}} dt = -\frac{x}{\sqrt{2\Delta}} \frac{2}{\Delta} e^{-\frac{x^2}{2\Delta}} \int_{\frac{x}{\sqrt{2\Delta}} \frac{\sigma_y}{\sigma_x}}^{\frac{x}{\sqrt{2\Delta}}} \frac{e^{t^2}}{t^2} dt \quad (2.23) \\ &= -\frac{x}{\sqrt{2\Delta}} \frac{2}{\Delta} e^{-\frac{x^2}{2\Delta}} \left\{ \left[ -\frac{e^t}{t} dt \right]_{\frac{x}{\sqrt{2\Delta}} \frac{\sigma_y}{\sigma_x}}^{\frac{x}{\sqrt{2\Delta}}} + 2 \int_{\frac{x}{\sqrt{2\Delta}} \frac{\sigma_y}{\sigma_x}}^{\frac{x}{\sqrt{2\Delta}}} e^{t^2} dt \right\} \\ &= -\sqrt{\frac{2\pi}{\Delta}} \frac{x}{\Delta} e^{-\frac{x^2}{2\Delta}} [\text{erfi}(\frac{x}{\sqrt{2\Delta}}) - \text{erfi}(\frac{x}{\sqrt{2\Delta}} \frac{\sigma_y}{\sigma_x})] - \frac{2}{\Delta} [e^{-\frac{x^2}{2\sigma_x^2}} \frac{\sigma_x}{\sigma_y} - 1] . \end{aligned}$$

Either by a similar integration or by using  $i\text{erfi}(-ix) = \text{erf}(x)$  one obtains

$$\partial_x U|_{x=0} = 0 , \quad (2.24)$$

$$\partial_x^2 U|_{x=0} = \frac{2}{\Delta} \left( \sqrt{\frac{\pi}{2\Delta}} y e^{\frac{y^2}{2\Delta}} [\text{erf}(\frac{y}{\sqrt{2\Delta}} \frac{\sigma_x}{\sigma_y}) - \text{erf}(\frac{y}{\sqrt{2\Delta}})] + e^{-\frac{y^2}{2\sigma_y^2}} \frac{\sigma_y}{\sigma_x} - 1 \right) , \quad (2.25)$$

$$\partial_y U|_{x=0} = -\sqrt{\frac{2\pi}{\Delta}} e^{\frac{y^2}{2\Delta}} [\text{erf}(\frac{y}{\sqrt{2\Delta}} \frac{\sigma_x}{\sigma_y}) - \text{erf}(\frac{y}{\sqrt{2\Delta}})] , \quad (2.26)$$

$$\partial_y^2 U|_{x=0} = -\frac{2}{\Delta} \left( \sqrt{\frac{\pi}{2\Delta}} y e^{\frac{y^2}{2\Delta}} [\text{erf}(\frac{y}{\sqrt{2\Delta}} \frac{\sigma_x}{\sigma_y}) - \text{erf}(\frac{y}{\sqrt{2\Delta}})] + e^{-\frac{y^2}{2\sigma_y^2}} \frac{\sigma_x}{\sigma_y} - 1 \right) \quad (2.27)$$

The Laplace equation for the projected electrostatic potential of the proton beam with charge  $\lambda$  per unit length is implicit in these formulas due to

$$(\partial_x^2 + \partial_y^2) \frac{\lambda}{4\pi\epsilon_0} U(x, y)|_{x=0} = -\frac{\lambda}{4\pi\epsilon_0} \frac{2}{\sigma_x \sigma_y} e^{-\frac{y^2}{2\sigma_y^2}} = -\frac{\lambda}{\epsilon_0} \int_{-\infty}^{\infty} \rho(0, y, z) dz . \quad (2.28)$$

### 2.3 Luminosity Scan for the 60° Optics

A luminosity scan was performed at the ZEUS detector with the current 60° optics after the proton beam was completely separated from the  $e^+$  beam in the H1 experiment. The proton current was only 39.2mA and the measured proton emittances

were  $4\beta\gamma\epsilon_x^p = 22\text{mm mrad}$  and  $4\beta\gamma\epsilon_y^p = 14\text{mm mrad}$ . The nominal beta functions at the experiment were  $\beta_x^p = 1\text{m}$ ,  $\beta_y^p = 0.5\text{m}$ ,  $\beta_x^e = 0.9\text{m}$ ,  $\beta_y^e = 0.6\text{m}$ . The fractional  $e^+$  tunes were controlled by a phase locked loop system to 0.142 in the horizontal and to 0.211 in the vertical plane. The phase locked loop regulates the coherent frequency of the beam's dipole moment. As derived in [6, 8] this frequency is approximately by half the beam-beam tune shifts lower than the tunes without the beam-beam force  $Q_x^e$  and  $Q_y^e$ . With the tune shift parameter of  $\Delta Q_x^e = -C_{bb}\partial_x^2 U(0, 0)\frac{\beta_x^e}{4\pi} = 0.0045$  and  $\Delta Q_y^e = -C_{bb}\partial_y^2 U(0, 0)\frac{\beta_y^e}{4\pi} = 0.014$ , the tunes for the following simulations were therefore  $Q_x^e = 0.144$  and  $Q_y^e = 0.218$ .

The resulting beam-beam kicks and disturbances of the beta functions are shown in figure 2.1.

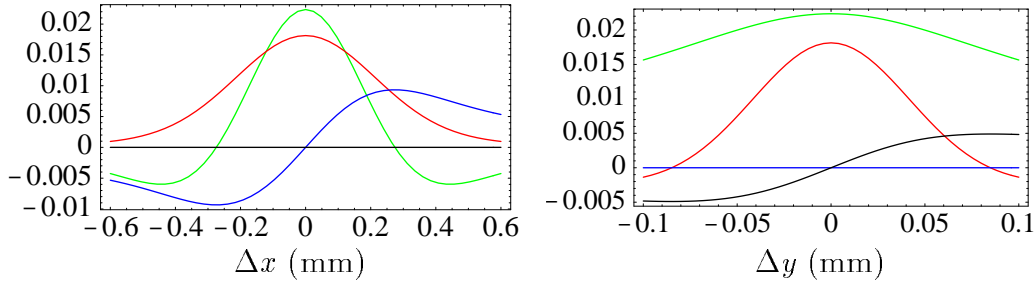


**Figure 2.1:** Perturbations due to the beam-beam effect during the luminosity scan for the 60° optics. The bottom curves describe the beam-beam kicks  $\delta x_{bb}$  (blue) and  $\delta y_{bb}$  (black) in mm. The highest (red) and the second highest (green) curves describe the relative change of the beta functions  $\delta\beta_y^e$  and  $\delta\beta_x^e$  respectively.

The data of the horizontal and the vertical luminosity scan is given by the points in the first two graphs of figure 2.2, where the luminosity is shown as a function of the amplitudes  $\Delta x_0$  and  $\Delta y_0$  of the symmetric bump which is used to separate the two beams.

The upper (green) curve shows the luminosity which would be expected by equation (2.15) when  $\Sigma_x$  and  $\Sigma_y$  are computed by method (a), whereas the lower (red) curve shows the luminosity which would be expected when method (b) was used. For Gaussian beams the two methods should lead to equivalent results and their deviation shows that the luminosity scan is not yet evaluated in a satisfactory way.

The next two graphs in figure 2.2 show the expected luminosity for method (a) and method (b) when applied to the data which has been corrected for the beam-beam kick. Above the green curve there is a hardly visible blue curve which describes the expected luminosity with a beta function which changes during the luminosity scan due to the beam-beam lens. In this case the difference is very small and when this effect is subtracted from the data before obtaining  $\Sigma_x$  and  $\Sigma_y$  the curves hardly change, as shown in the last two graphs of figure 2.2. The  $e^+$  emittances finally obtained by method (a) are

$$\epsilon_x^e = 50\text{nm} , \quad \epsilon_y/\epsilon_x = 5\% . \quad (2.29)$$

The nominal emittance is only 41nm. A too low RF frequency has been measured

by various methods as reported in [9, 10] and an emittance of 50nm correspond to an RF frequency which is by 120Hz too low.

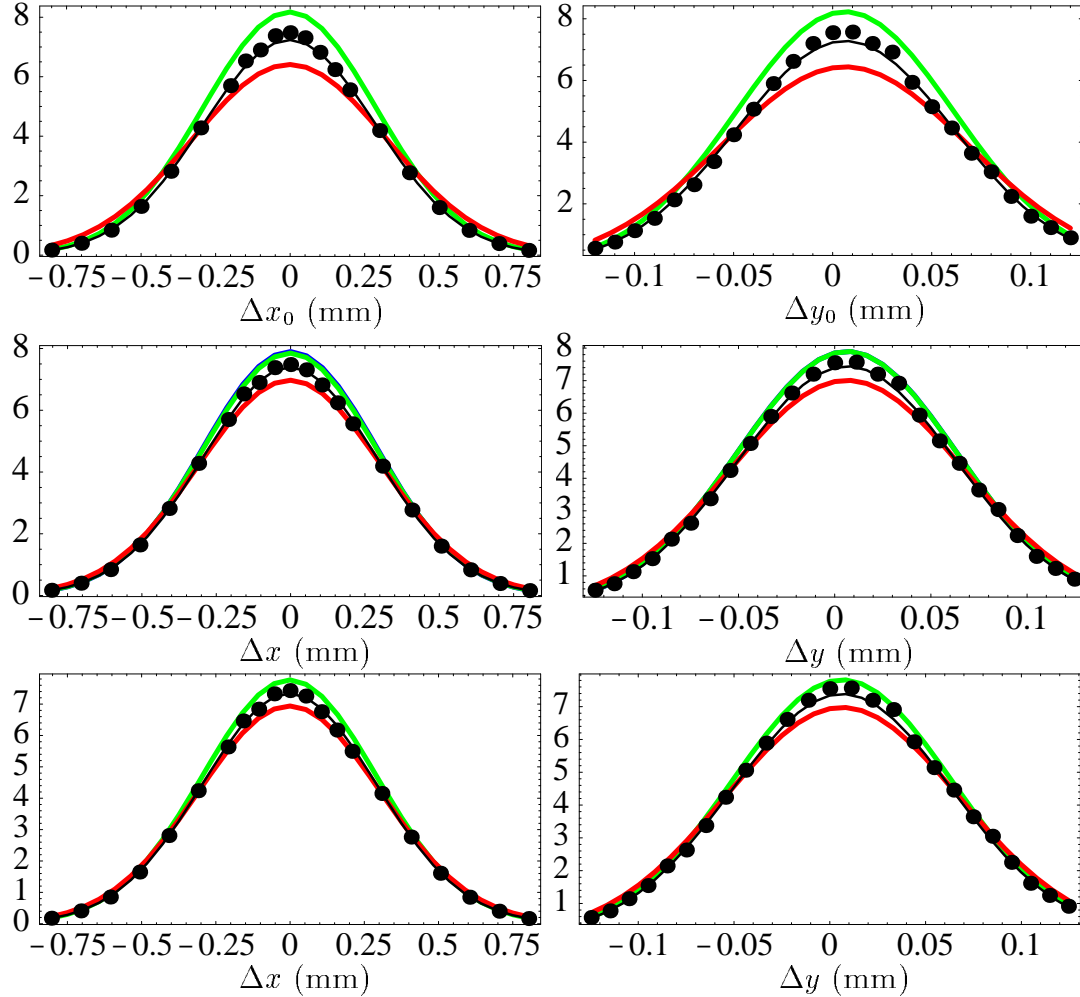


**Figure 2.2:** The luminosity scan at ZEUS for the  $60^\circ$  optics. Left: The horizontal luminosity scan. Right: The vertical luminosity scan. Top: the luminosity data (dots) and a Gaussian fit (black) together with the luminosity (green, upper curve) expected by equation (2.15) when obtaining  $\Sigma_x$  and  $\Sigma_y$  by method (a) from the width of the fit and the luminosity (red, lower curve) expected by equation (2.15) when obtaining  $\Sigma_x$  and  $\Sigma_y$  by method (b) from the area under the fit. Middle: The corresponding curves after correcting for the varying beam-beam kick. The curve (blue) slightly above the curve from method (a) additionally contains the effect of the varying beam-beam lens. Bottom: The corresponding curves after correcting for the varying beam-beam lens.

In the last two graphs, the curves for method (a) and method (b) agree much better than in the first two graphs, demonstrating the importance of including the changing beam-beam kick during the luminosity scan. One can try to make an incorrectly measured proton emittance responsible for the remaining mismatch between the two methods. To investigate the sensitivity of the curves to the proton emittance,  $\epsilon_x^p$  and  $\epsilon_y^p$  were varied until the beam-beam force was so strong that

method (a) and (b) lead to equivalent luminosity scan curves as shown in figure 2.3. The proton emittance which had to be assumed was  $4\beta\gamma\epsilon_x^p = 9\text{mm mrad}$  and  $4\beta\gamma\epsilon_y^p = 9\text{mm mrad}$ . This shows for one part that the curves are not very sensitive to the proton emittance measurement and to the other part that the mismatch in the curves can not be due to an incorrect measurement of the proton emittances since these are certainly not as small as 9mm mrad.

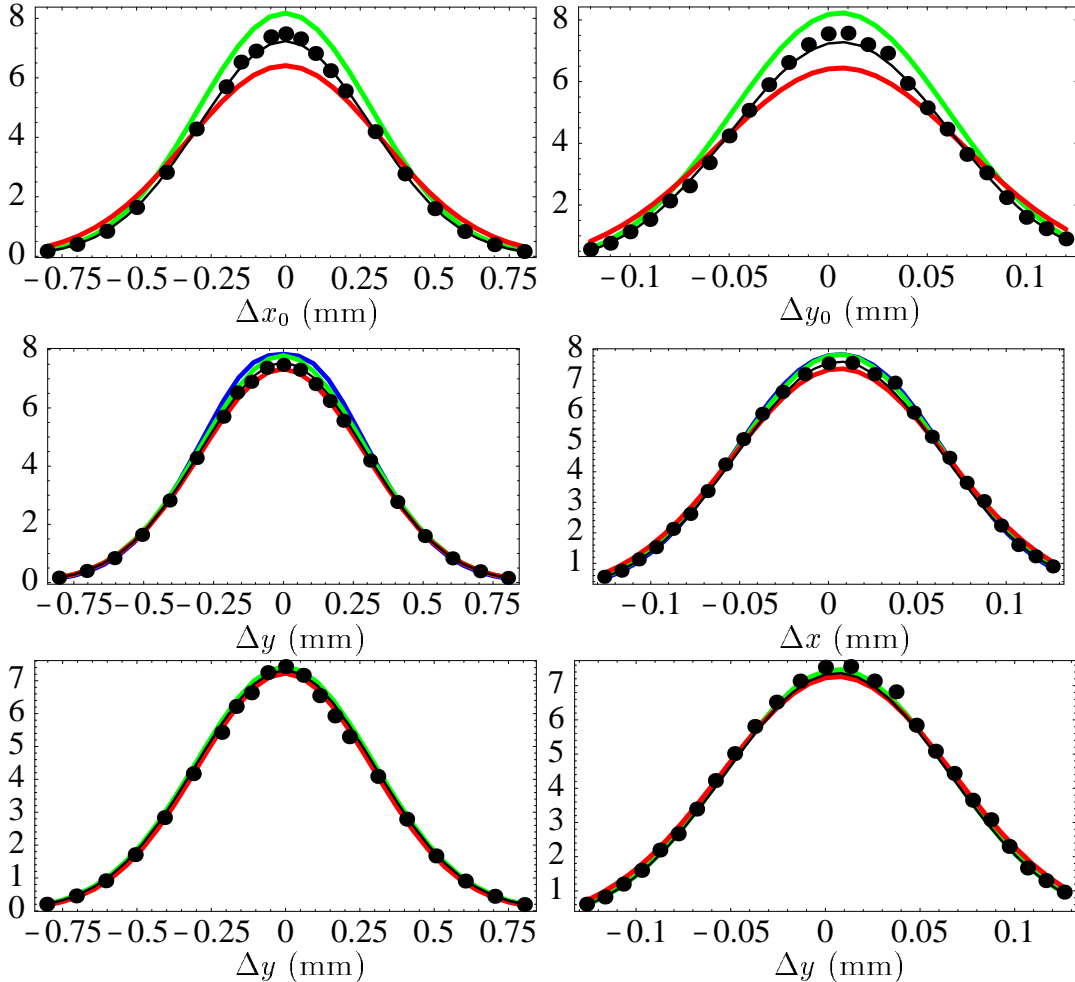


**Figure 2.3:** The luminosity scan at ZEUS for the 60° optics when assuming unrealistically small proton emittances of 9mm mrad. Left: The horizontal luminosity scan. Right: The vertical luminosity scan. Top: the luminosity data (dots) and a Gaussian fit (black) together with the luminosity (green, upper curve) expected by equation (2.15) when obtaining  $\Sigma_x$  and  $\Sigma_y$  by method (a) from the width of the fit and the luminosity (red, lower curve) expected by equation (2.15) when obtaining  $\Sigma_x$  and  $\Sigma_y$  by method (b) from the area under the fit. Middle: The corresponding curves after correcting for the varying beam-beam kick. The curve (blue) above the curve from method (a) additionally contains the effect of the varying beam-beam lens. Bottom: The corresponding curves after correcting for the varying beam-beam lens.

## 2.4 Luminosity Scan for the 72° Optics

For the luminosity scan performed for the 72° optics the proton current was 65.7mA and the proton emittances were measured to be  $4\beta\gamma\epsilon_x^p = 26\text{mm mrad}$  and  $4\beta\gamma\epsilon_y^p = 17\text{mm mrad}$ . The nominal beta functions at the interaction point were  $\beta_x^p = 1\text{m}$ ,  $\beta_y^p = 0.5\text{m}$ ,  $\beta_x^e = 1\text{m}$ ,  $\beta_y^e = 0.7\text{m}$ . The fractional  $e^+$  tunes were again controlled by a phase locked loop system to 0.142 in the horizontal and to 0.211 in the vertical plane. With the tune shift parameter of  $\Delta Q_x^e = 0.007$  and  $\Delta Q_y^e = 0.023$ , the tunes for the following simulations were therefore  $Q_x^e = 0.145$  and  $Q_y^e = 0.222$ .

The beam-beam kicks and the disturbances of the beta functions are shown in figure 2.4.

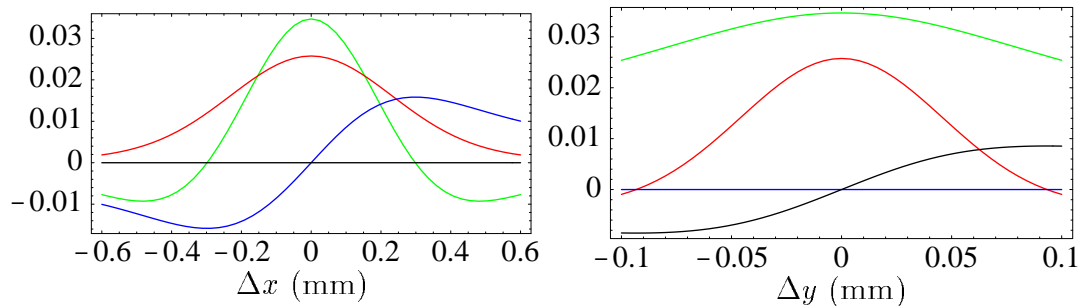


**Figure 2.4:** Perturbations due to the beam-beam effect during the luminosity scan for the 72° optics. The bottom curves describe the beam-beam kicks  $\delta x_{bb}$  (blue) and  $\delta y_{bb}$  (black) in mm. The highest (red) and the second highest (green) curves describe the relative change of the beta functions  $\delta\beta_y^e$  and  $\delta\beta_x^e$  respectively.

The curves for a luminosity scan with the 72° optic in the ZEUS detector in figure 2.5 do not match the luminosity scan data as well as for the 60° optics but again it is apparent that a correction for the beam-beam kick is mandatory and that a correction for the change of the beam-beam lens over the luminosity scan is not relevant at the given HERA parameters. The  $e^+$  emittances which one finally obtains are

$$\epsilon_x^e = 25\text{nm} , \quad \epsilon_y/\epsilon_x = 22\% . \quad (2.30)$$

During this experiment the collision at the H1 detector was not avoided but the luminosity at this experiment was kept constant at a maximum value. This leads to an additional disturbance of the HERA-e beta functions of about 3% as shown in figure 2.4. This effect would therefore allow for an emittance which is 3% larger and thus closer to the nominal value of  $\epsilon_x^e = 33\text{nm}$ . However with an RF frequency which is more than 100Hz too low, the emittance should be even larger than the nominal value.

In figure 2.6 an equivalent luminosity scan was performed at the H1 detector while the luminosity at ZEUS was kept maximal. The resulting emittances are

$$\epsilon_x^e = 31\text{nm} , \quad \epsilon_y/\epsilon_x = 21\% . \quad (2.31)$$

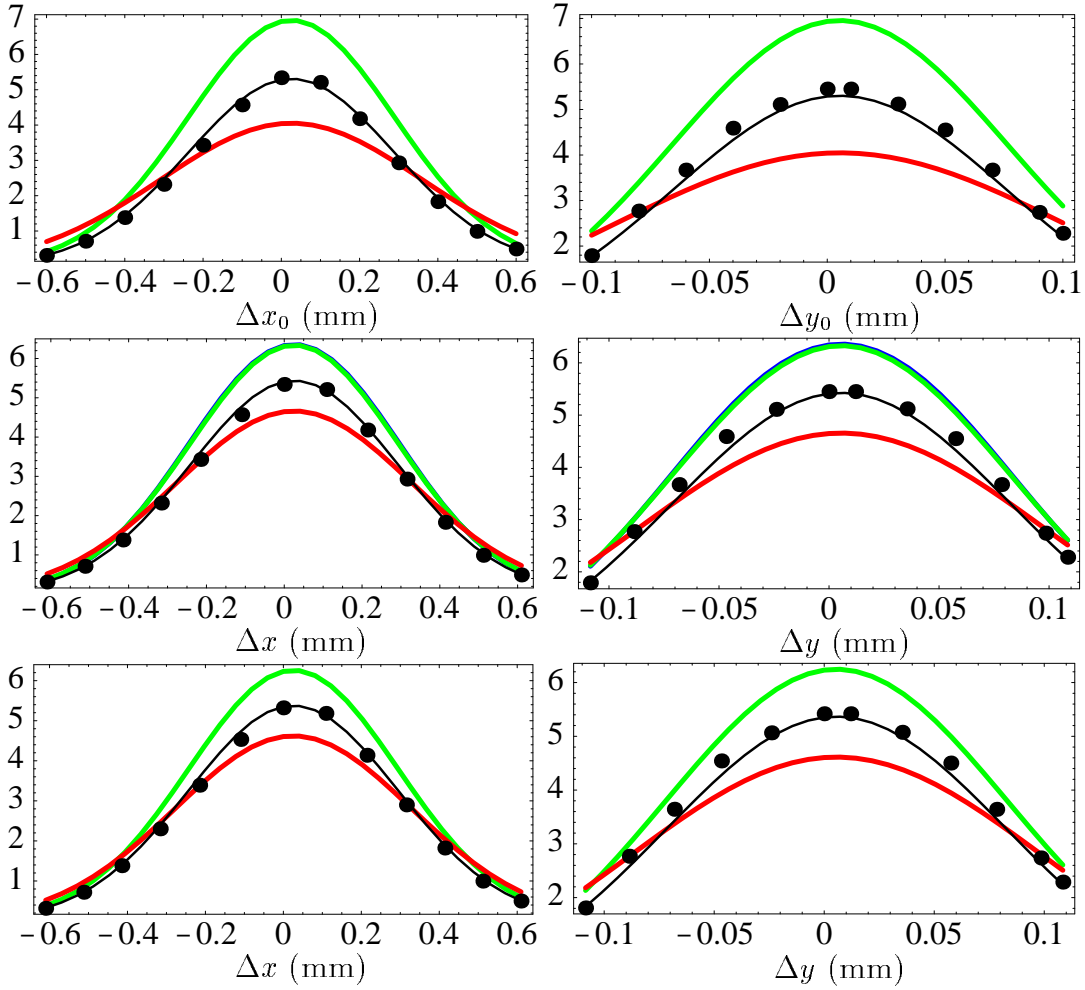


**Figure 2.5:** The luminosity scan at ZEUS for the 72° optics. Left: The horizontal luminosity scan. Right: The vertical luminosity scan. Top: the luminosity data (dots) and a Gaussian fit (black) together with the luminosity (green, upper curve) expected by equation (2.15) when obtaining  $\Sigma_x$  and  $\Sigma_y$  by method (a) from the width of the fit and the luminosity (red, lower curve) expected by equation (2.15) when obtaining  $\Sigma_x$  and  $\Sigma_y$  by method (b) from the area under the fit. Middle: The corresponding curves after correcting for the varying beam-beam kick. The curve (blue) slightly above the curve from method (a) additionally contains the effect of the varying beam-beam lens. Bottom: The corresponding curves after correcting for the varying beam-beam lens.

Especially the emittance ratio agrees rather well with that obtained for the luminosity scan at ZEUS. It also agrees well with the ratio obtained by scraping the tails of the  $e^+$  distribution as reported in [11, 12]. We therefore conclude that the luminosity of the 72° optics was probably lower than expected because of the large vertical  $e^+$  spot size at the interaction point. In future experiments the vertical spot size should be minimized by means of dispersion correction and decoupling bumps in HERA-e.

Again it was checked whether an incorrectly determined proton emittance could

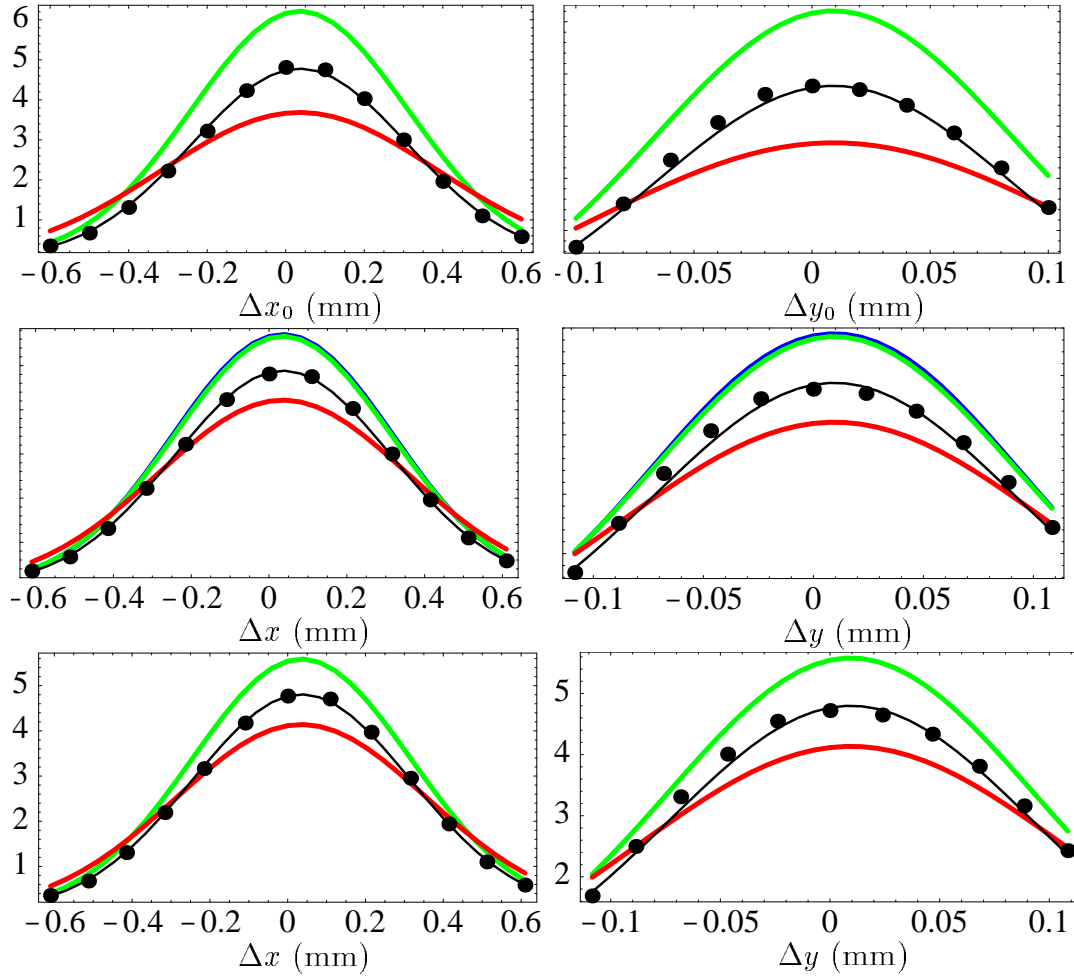


**Figure 2.6:** The luminosity scan at H1 for the  $72^\circ$  optics. Left: The horizontal luminosity scan. Right: The vertical luminosity scan. Top: the luminosity data (dots) and a Gaussian fit (black) together with the luminosity (green, upper curve) expected by equation (2.15) when obtaining  $\Sigma_x$  and  $\Sigma_y$  by method (a) from the width of the fit and the luminosity (red, lower curve) expected by equation (2.15) when obtaining  $\Sigma_x$  and  $\Sigma_y$  by method (b) from the area under the fit. Middle: The corresponding curves after correcting for the varying beam-beam kick. The curve (blue) slightly above the curve from method (a) additionally contains the effect of the varying beam-beam lens. Bottom: The corresponding curves after correcting for the varying beam-beam lens.

be responsible for the mismatch of method (a) and method (b). To bring the two methods into agreement in figure 2.7, the beam-beam force had to be increased strongly by choosing  $4\beta\gamma\epsilon_x^p = 4.5\text{mm mrad}$  and  $4\beta\gamma\epsilon_x^p = 4.5\text{mm mrad}$ . These emittances are far too small to be realistic and the proton emittance is therefore not responsible for the mismatch between the two methods of determining  $\Sigma_x$  and  $\Sigma_y$ .

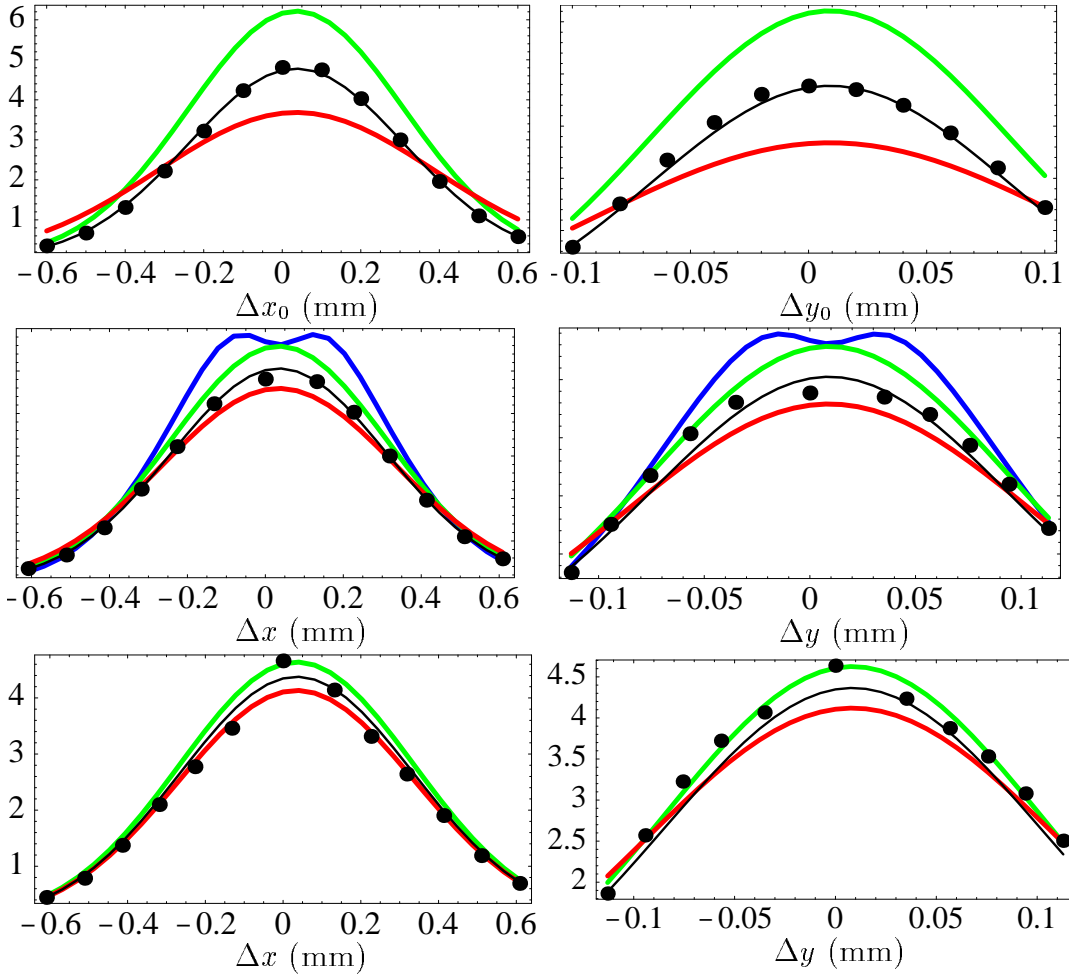


**Figure 2.7:** The luminosity scan at H1 for the 72° optics when assuming unrealistically small proton emittances of 4.5mm mrad. Left: The horizontal luminosity scan. Right: The vertical luminosity scan. Top: the luminosity data (dots) and a Gaussian fit (black) together with the luminosity (green, upper curve) expected by equation (2.15) when obtaining  $\Sigma_x$  and  $\Sigma_y$  by method (a) from the width of the fit and the luminosity (red, lower curve) expected by equation (2.15) when obtaining  $\Sigma_x$  and  $\Sigma_y$  by method (b) from the area under the fit. Middle: The corresponding curves after correcting for the varying beam-beam kick. The curve (blue) above the curve from method (a) additionally contains the effect of the varying beam-beam lens. Bottom: The corresponding curves after correcting for the varying beam-beam lens.

## 2.5 Size of the Photon Spot in the Luminosity Detectors

In [13] the size of the photon spot in the ZEUS and H1 luminosity monitors were used to compute the emittance of the  $e^+$  beam. A comparison with theoretical expectations and with the synchrotron light spot lead to the suspicion that the emittance can not be very accurately obtained from the photon spot in the luminosity detector. Nevertheless, the photon spot sizes  $\sigma_{phx}$  and  $\sigma_{phy}$  were recorded during the luminosity scans. The bremsstrahlung of the positrons created in the interaction region

		$\sigma_{phx}$	$\epsilon_x^e$	$\sigma_{phy}$	$\frac{\epsilon_y^e}{\epsilon_x^e}$
$60^\circ$	ZEUS	2.15cm	35.4nm	0.59cm	4.2%
$72^\circ$	ZEUS	1.98cm	33.3nm	0.98cm	16.3%
$72^\circ$	H1	1.55cm	20.2nm	0.88cm	21.3%

**Table 2.1:** The emittances obtained from the size of the photon spot in the luminosity monitors.

is radiated in a cone with angle  $\vartheta$  which depends on the scattering particle and is approximately  $\frac{1}{\gamma}$ . At ZEUS this radiation is detected  $L = 107.6$ m downstream by a detector with resolution  $r = 1.5$ mm, where the rms photon spot size  $\sigma_{phx}$  is related to the  $e^+$  emittance by

$$\epsilon_x^e = \beta_x^e \frac{\sigma_{phx}^2 - r^2 - (L\vartheta)^2}{L^2 + \beta_x^{e2}} . \quad (2.32)$$

The vertical emittance is obtained correspondingly. In contrast to the more general evaluation in [13], here it was assumed that the dispersion, its slope,  $\alpha_x$ , and  $\alpha_y$  vanish at the interaction point. The so obtained emittances stated in table (2.1) support the conclusion that a large ratio  $\epsilon_y^e/\epsilon_x^e$  is responsible for the too low luminosity of the  $72^\circ$  optics.

**Acknowledgment:** We appreciate the help of E. Gianfelice who took the data of the luminosity scans.

### 3 Optimized Luminosity Scans for a Spinmatched 72° Optics in HERA-e

by G. H. Hoffstaetter, DESY Hamburg

Date: 2000, Aug. 27, 11pm to Aug. 28, 11am, Logbook XLV, p. 33–40

Date: 2000, Aug. 29, 11pm to Aug. 30, 6am, Logbook XLV, p. 56–59

As described in section 2 luminosity scans can be used to determine the emittances of the HERA electron beam. Previous luminosity scans for the 72° optics have shown that the luminosity was lower than expected due to a large vertical electron spot sizes at the interaction points of the H1 and ZEUS collider experiments. Therefor the 72° optics was again installed in HERA-e and the luminosity was optimized by adjustment of the decoupling bump, by minimizing the crossing angle of the two beams, and by correcting the vertical dispersion as described in section 6. The decoupling bump turned out to be the main parameter by which the luminosity could be increased, in spite of the fact that this bump was computed for the standard optics with 60° phase advance per FODO cell.

Luminosity scans were performed as in section 2. As compared to these earlier experiments the luminosity scan was performed more accurately and more data points were taken, so that a new and more accurate method of evaluating luminosity scan data could be applied. In contrast to the previously used evaluation where Gaussian distributions had to be assumed, the new method is independent of the beam distributions. To be able to correct as accurately as possible for the beam-beam kick and the beam-beam beta beat, luminosity was only established at one experiment during each scan and the tune controller was switched off. For the evaluation of the data, the HERA proton beam is assumed to be unaffected by the beam-beam force during the luminosity scan.

#### 3.1 Improved Luminosity Scans

As described in equation (2.2) the luminosity scan in  $x$ -direction for a distance  $\Delta x$  between the two beam centers leads to the specific luminosity of

$$\mathcal{L}_s^x(\Delta x) = \frac{1}{f q_p q_e} \int_{\infty} \left[ \int_{-\infty}^{\infty} \rho_p(x, y, z) dz \right] \left[ \int_{-\infty}^{\infty} \rho_e(x - \Delta x, y, z) dz \right] dx dy . \quad (3.1)$$

For product densities  $\rho(x, y, z) = \rho_x(x)\rho_y(y)\rho_z(z)$ , the second moments  $\langle x^2 \rangle_e$  and  $\langle y^2 \rangle_e$  of the second beam can be obtained by a luminosity scan, when the second

order moments of the first beam are known since the second order moment of the luminosity scan is given by

$$\begin{aligned}
 < x^2 >_{\mathcal{L}_s^x} &= \frac{\int_{-\infty}^{\infty} \mathcal{L}_s^x(\Delta x) \Delta x^2 d\Delta x}{\int_{-\infty}^{\infty} \mathcal{L}_s^x(\Delta x) d\Delta x} \\
 &= \frac{\int_{-\infty}^{\infty} \int_{-\infty}^{\infty} \rho_{xp}(x) \rho_{yp}(y) \rho_{xe}(x - \Delta x) \rho_{ye}(y) dx dy \Delta x^2 d\Delta x}{\int_{-\infty}^{\infty} \rho_{yp}(y) \rho_{ye}(y) dy} \\
 &= \int_{-\infty}^{\infty} \int_{-\infty}^{\infty} \rho_{xp}(x) \rho_{xe}(\tilde{x}) (x - \tilde{x})^2 dx d\tilde{x} = < x^2 >_p + < x^2 >_e .
 \end{aligned} \tag{3.2}$$

Here it has been used that the first moment  $< x >$  of a centered beam vanishes. It is important to note that this relation of the second order moments holds for all product densities and no specific knowledge on  $\rho_p$  is required to determine  $< x^2 >_e$ . In section 2, the two methods (a) and (b) had been used to determine the overlap beam sizes  $\Sigma_x = \sqrt{< x^2 >_p + < x^2 >_e}$  and  $\Sigma_y = \sqrt{< y^2 >_p + < y^2 >_e}$ .

**Method (a):** The standard deviation  $< x^2 >_{\mathcal{L}_s^x}$  of the luminosity scan is obtained by fitting  $a$ ,  $b$ , and  $c$  of a bell curve  $a \exp(-b(x - c)^2)$  to the data. Then one obtains  $\Sigma_x = 1/\sqrt{2b}$  and similarly  $\Sigma_y$ .

**Method (b):** It is assumed that both beams have a Gaussian density, which leads to

$$f q_p q_e \int_{-\infty}^{\infty} \mathcal{L}_s^x(\Delta x) d\Delta x = \int_{-\infty}^{\infty} \frac{e^{-\frac{y^2}{2\sigma_{yp}^2}}}{\sqrt{2\pi}\sigma_{yp}} \frac{e^{-\frac{y^2}{2\sigma_{ye}^2}}}{\sqrt{2\pi}\sigma_{ye}} dy = \frac{1}{\sqrt{2\pi}\sqrt{\sigma_{py}^2 + \sigma_{ey}^2}} . \tag{3.3}$$

In this method, the vertical overlap beam size is obtained from the horizontal luminosity scan with  $\Sigma_y = (\sqrt{2\pi} f q_p q_e \int_{-\infty}^{\infty} \mathcal{L}_s^x(\Delta x) d\Delta x)^{-1}$  and vice versa. The integral is again obtained from fitting a bell curve  $a \exp(-b(x - c)^2)$  for which the integral evaluates to  $a2\sqrt{\pi b}$ .

**Method (c):** Only assuming product distributions for the two beams, equation (3.2) is used to find

$$\Sigma_x = \frac{\int_{-\infty}^{\infty} \mathcal{L}_s^x(\Delta x) \Delta x^2 d\Delta x}{\int_{-\infty}^{\infty} \mathcal{L}_s^x(\Delta x) d\Delta x} , \quad \Sigma_y = \frac{\int_{-\infty}^{\infty} \mathcal{L}_s^y(\Delta y) \Delta y^2 d\Delta y}{\int_{-\infty}^{\infty} \mathcal{L}_s^y(\Delta y) d\Delta y} . \tag{3.4}$$

To check how well the data of the luminosity scan can be approximated by a Gaussian, two checks can be performed. (1) One can compare the data with the curve of equation (2.7). This Gaussian Luminosity scan curve, colored green in the following figures, has the  $\Sigma_x$  and  $\Sigma_y$  of equation (3.4). However, it might not have the integral  $\int_{-\infty}^{\infty} \mathcal{L}_s^x(\Delta x) d\Delta x$  which one obtains from the data. (2) One can alternatively assume Gaussian beam distributions and compute  $\Sigma_y = (\sqrt{2\pi} f q_p q_e \int_{-\infty}^{\infty} \mathcal{L}_s^x(\Delta x) d\Delta x)^{-1}$  and similarly  $\Sigma_x$  by integrating the luminosity scan data. Subsequently one can compare

the resulting curve of equation (2.7), colored red in the following figures, with the data points.

The range of applicability of the first two methods (a) and (b) is restricted since it is required that the luminosity scan data can be fitted well by a bell curve, and in case of (b) each beam distribution has to be approximately Gaussian. Method (c) does not have this restriction. On the other hand, these two methods have the advantage that they can be evaluated even when the data points of the luminosity scan are too sparse to allow for an accurate evaluation of the integrals in equation (3.4). The most accurate method (c) requires many data points which go up to large scan amplitudes  $\Delta x$  and  $\Delta y$ .

The HERA proton beam size  $\langle x^2 \rangle_p$  is obtained by fitting a Gaussian to wire scanner data. Together with the luminosity scan, the  $e^+$  beam size is then determined.

### 3.2 Two Luminosity Scans for the H1 Interaction Point

When the  $72^\circ$  optics was newly installed again after it had not been used for 6 month, the luminosity was increased by optimizing the decoupling bump only and the following luminosity scan was performed. The proton current was 90.4mA and the proton emittances were measured to be  $4\beta\gamma\epsilon_x^p = 20.7\text{mm mrad}$  and  $4\beta\gamma\epsilon_y^p = 14.5\text{mm mrad}$ . The nominal beta functions at the interaction point were  $\beta_x^p = 1\text{m}$ ,  $\beta_y^p = 0.5\text{m}$ ,  $\beta_x^e = 1\text{m}$ ,  $\beta_y^e = 0.7\text{m}$ . The fractional  $e^+$  tunes were initially set to 0.179 in the horizontal and to 0.245 in the vertical plane. Due to the beam-beam force the tunes were allowed to change during the luminosity scan. This has the advantage that the tune of the ring alone does not change and the beam-beam kick on the closed orbit can be computed more easily. As derived in [8] the tunes in the ring without beam-beam kick are larger by about half the tune shift parameter of  $\Delta Q_x^e = 0.0122$  and  $\Delta Q_y^e = 0.0383$ . The tunes for the following simulations were therefore  $Q_x^e = 0.185$  and  $Q_y^e = 0.264$ .

The beam-beam kicks and the disturbances of the beta functions are shown in figure 3.1.

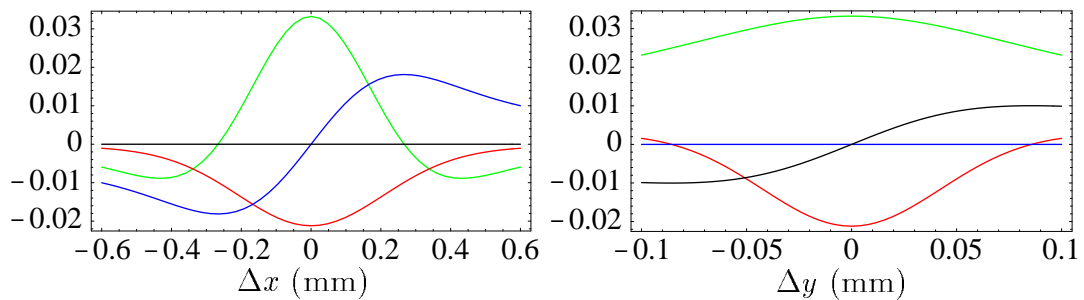


**Figure 3.1:** Perturbations due to the beam-beam effect during the first luminosity scan at H1. The bottom curves describe the beam-beam kicks  $\delta x_{bb}$  (blue) and  $\delta y_{bb}$  (black) in mm. The highest (red) and the second highest (green) curves describe the relative change of the beta functions  $\delta\beta_y^e$  and  $\delta\beta_x^e$  respectively.

The curves for the first luminosity scan at H1 in figure 3.2 match the luminosity scan data quite well when the beam-beam kick and the beam-beam beta beat as well as the corrected tune are taken into account. The two top figures show that a correction for the beam-beam kick is mandatory. A correction for the change of the beam-beam lens over the luminosity scan has been taken into account but it is not very relevant at the given HERA parameters. When assuming that the RF frequency is the center frequency of the ring, the horizontal emittance is computed to  $\epsilon_x = 31\text{nm}$ . The  $e^+$  emittance which one finally obtains from this luminosity scan is however much larger,

$$\epsilon_x^e = 58\text{nm} , \quad \epsilon_y/\epsilon_x = 4.6\% . \quad (3.5)$$

It has to be noted however that the proton emittance has a large error due to the quite inaccurate data from the wire scanner.

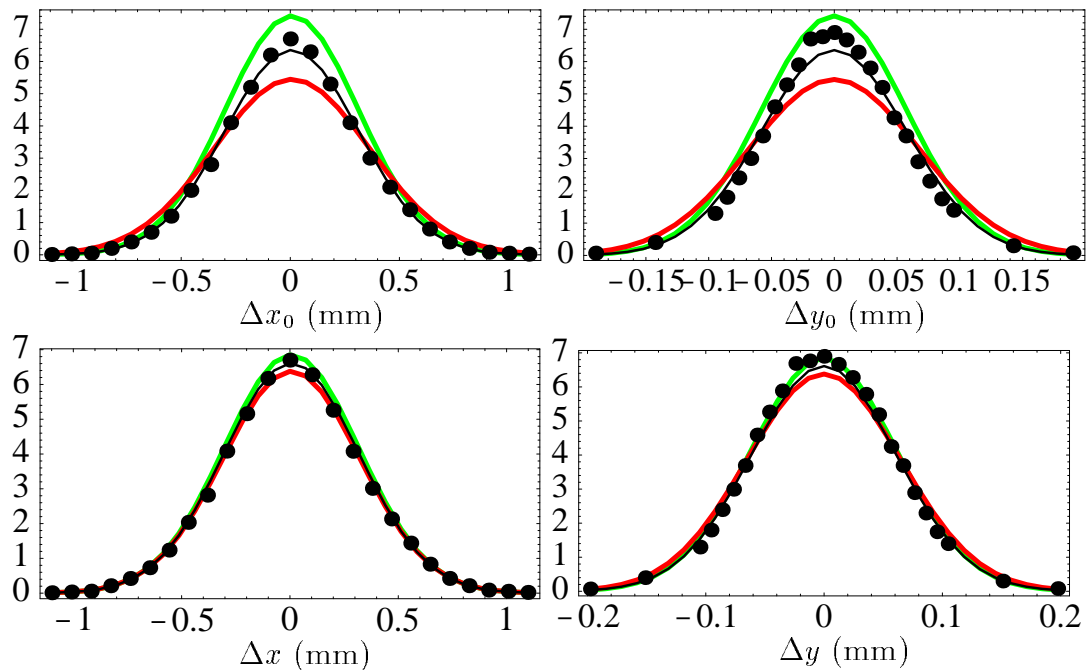


**Figure 3.2:** First luminosity scan at H1. Left: The horizontal luminosity scan. Right: The vertical luminosity scan. Top: the luminosity data (dots) and a bell curve fit (black) together with the luminosity (green, upper curve) expected by equation (2.15) when obtaining  $\Sigma_x$  and  $\Sigma_y$  by method (c) from the standard deviation of the fit and the luminosity (red, lower curve) expected by equation (2.15) when obtaining  $\Sigma_x$  and  $\Sigma_y$  by the area under the fit as also described in method (c). Bottom: The corresponding curves after correcting for the varying beam-beam kick and for the varying beam-beam lens.

In figure 3.4 an equivalent luminosity scan was performed at the H1 detector two days later, after the vertical dispersion beat had been corrected as described in section 6 and after the crossing angles of the beams had been minimized. During these two day the polarization of the  $e^+$  beam had been optimized to 63% and therefore the closed orbit was corrected well. The beams were again separated

by a vertical bump for the proton beam at ZEUS. The proton current was 90mA and the proton emittances were measured to be  $4\beta\gamma\epsilon_x^p = 23\text{mm mrad}$  and  $4\beta\gamma\epsilon_y^p = 30\text{mm mrad}$ . A second measurement of the unusually large vertical emittance revealed that the wire of the vertical wire scanner was broken. Furthermore this vertical proton emittance is larger than  $\Sigma_y$  obtained by the luminosity scan. Therefore  $4\beta\gamma\epsilon_y^p = 25\text{mm mrad}$  was assumed for the following evaluations. The fractional  $e^+$  tunes were initially set to 0.141 in the horizontal and to 0.227 in the vertical plane. For the tune shift parameter of  $\Delta Q_x^e = 0.0105$  and  $\Delta Q_y^e = 0.0263$ . The tunes for the following simulations were therefore  $Q_x^e = 0.146$  and  $Q_y^e = 0.240$ . The beam-beam kicks and the disturbances of the beta functions are shown in figure 3.3. The resulting horizontal emittance for this second luminosity scan at H1 is very close to the theoretical value of  $\epsilon_x^e = 32\text{nm}$  and the emittance ratio, which had been very large in the luminosity scans described in section 2, has been reduced very effectively:

$$\epsilon_x^e = 32\text{nm} , \quad \epsilon_y/\epsilon_x = 2.1\% . \quad (3.6)$$

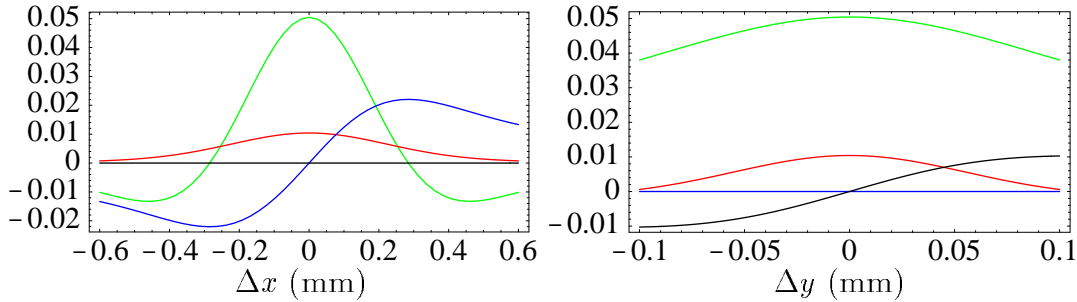


**Figure 3.3:** Perturbations due to the beam-beam effect during the second luminosity scan at H1. The bottom curves describe the beam-beam kicks  $\delta x_{bb}$  (blue) and  $\delta y_{bb}$  (black) in mm. The highest (red) and the second highest (green) curves describe the relative change of the beta functions  $\delta\beta_y^e$  and  $\delta\beta_x^e$  respectively.

### 3.3 Luminosity Scan for the ZEUS Interaction Point

The luminosity at ZEUS was optimized to a higher value than at H1 and therefore the luminosity scan presented here probably describes well optimized running conditions better than the previous luminosity scans.

This luminosity scan was performed just after the second scan at the H1 interaction point and therefore the electron ring was just as well optimized as during the previously described luminosity scan. The proton current was 90mA and again the proton emittances  $4\beta\gamma\epsilon_x^p = 23\text{mm mrad}$  and  $4\beta\gamma\epsilon_y^p = 25\text{mm mrad}$  were used for the evaluation. The fractional  $e^+$  tunes were initially set to 0.146 in the horizontal and to 0.231 in the vertical plane. Due to the tune shift parameter of  $\Delta Q_x^e = 0.0105$  and  $\Delta Q_y^e = 0.0263$  the tunes for the following simulations were  $Q_x^e = 0.151$  and

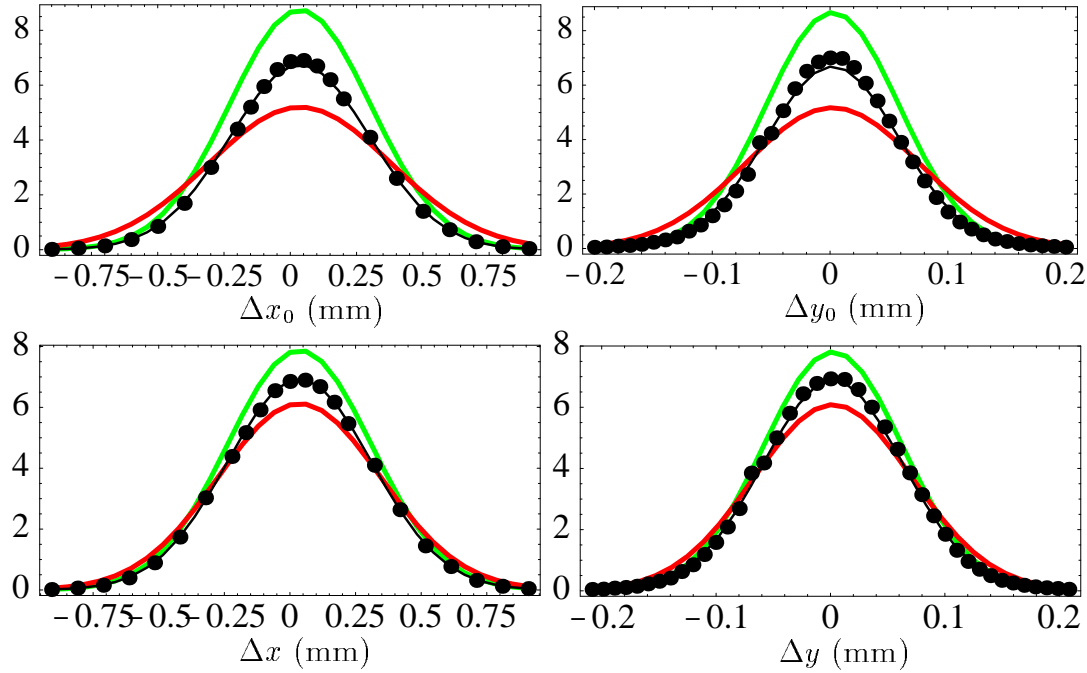


**Figure 3.4:** Second luminosity scan at H1. Left: The horizontal luminosity scan. Right: The vertical luminosity scan. Top: the luminosity data (dots) and a bell curve fit (black) together with the luminosity (green, upper curve) expected by equation (2.15) when obtaining  $\Sigma_x$  and  $\Sigma_y$  by method (c) from the standard deviation of the fit and the luminosity (red, lower curve) expected by equation (2.15) when obtaining  $\Sigma_x$  and  $\Sigma_y$  by the area under the fit as also described in method (c). Bottom: The corresponding curves after correcting for the varying beam-beam kick and for the varying beam-beam lens.

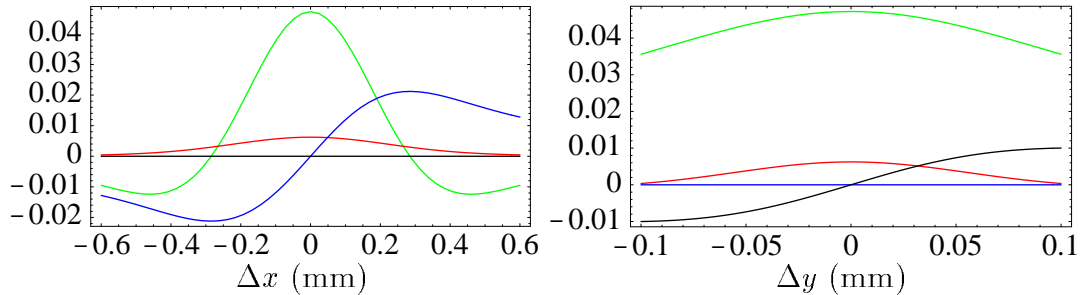


**Figure 3.5:** Perturbations due to the beam-beam effect during the luminosity scan at ZEUS. The bottom curves describe the beam-beam kicks  $\delta x_{bb}$  (blue) and  $\delta y_{bb}$  (black) in mm. The highest (red) and the second highest (green) curves describe the relative change of the beta functions  $\delta\beta_y^e$  and  $\delta\beta_x^e$  respectively.

$Q_y^e = 0.244$ . The beam-beam kicks and the disturbances of the beta functions are shown in figure 3.5.

The curves for the first luminosity scan at ZEUS in figure 3.6 match the luminosity scan data extremely well when the beam-beam kick and the beam-beam beta beat as well as the corrected tune are taken into account. The two top figures show

again that a correction for the beam-beam kick is mandatory. The correction for the change of the beam-beam lens over the luminosity scan has been taken into account but it is not very relevant at the given HERA parameters. The  $e^+$  emittance which one finally obtains from this luminosity scan is again quite close to the theoretical value of  $\epsilon_x^e = 31\text{nm}$ ,

$$\epsilon_x^e = 28\text{nm} , \quad \epsilon_y / \epsilon_x = 3.3\% . \quad (3.7)$$

As already shown by the luminosity scans at the H1 interaction point the emittance ratio shows again that the vertical beam size at the interaction point can efficiently be minimized in the  $72^\circ$  optics.

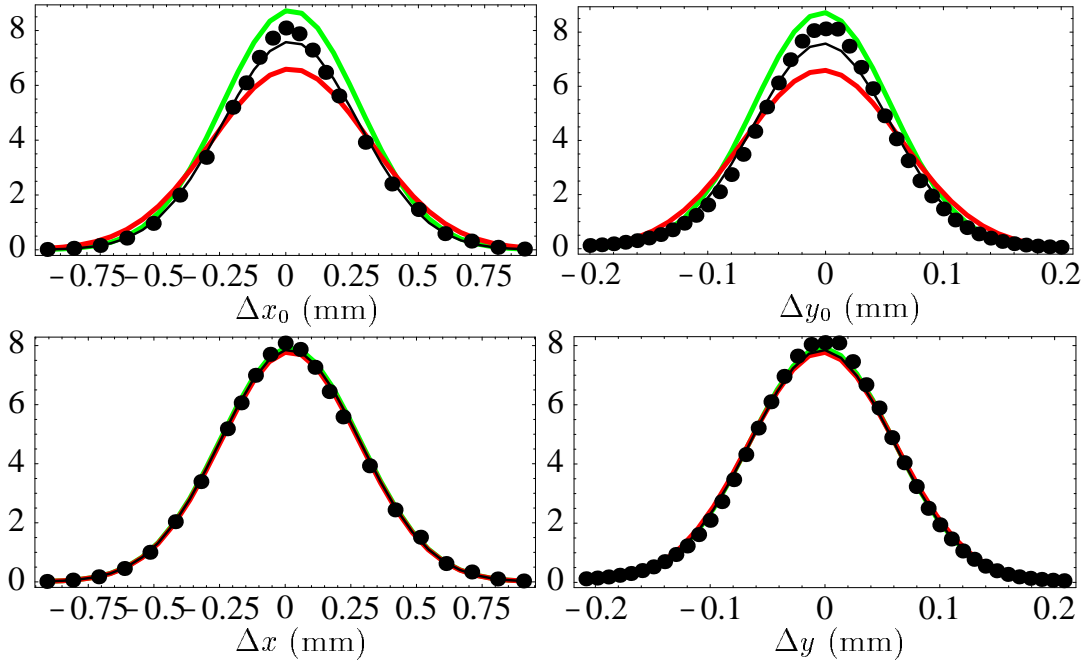


**Figure 3.6:** Luminosity scan at ZEUS. Left: The horizontal luminosity scan. Right: The vertical luminosity scan. Top: the luminosity data (dots) and a bell curve fit (black) together with the luminosity (green, upper curve) expected by equation (2.15) when obtaining  $\Sigma_x$  and  $\Sigma_y$  by method (c) from the standard deviation of the fit and the luminosity (red, lower curve) expected by equation (2.15) when obtaining  $\Sigma_x$  and  $\Sigma_y$  by the area under the fit as also described in method (c). Bottom: The corresponding curves after correcting for the varying beam-beam kick and for the varying beam-beam lens.

### 3.4 Size of the Photon Spot in the Luminosity Detectors

In [13] the size of the photon spot in the ZEUS and H1 luminosity monitors were used to compute the emittance of the  $e^+$  beam. A comparison with theoretical expectations and with the synchrotron light spot lead to the suspicion that the emittance can not be very accurately obtained from the photon spot in the luminosity detector.

		$\sigma_{phx}$	$\epsilon_x^e$	$\sigma_{phy}$	$\frac{\epsilon_y^e}{\epsilon_x^e}$
72°	H1	1.65cm	23.5nm	0.50cm	6.4%
72°	H1	1.65cm	23.5nm	0.48cm	5.9%
72°	ZEUS	2.10cm	38.1nm	0.55cm	4.8%

**Table 3.1:** The emittances obtained from the size of the photon spot in the luminosity monitors.

Nevertheless, the photon spot sizes  $\sigma_{phx}$  and  $\sigma_{phy}$  were recorded during the luminosity scans. The bremsstrahlung of the positrons created in the interaction region is radiated in a cone with angle  $\vartheta$  which depends on the scattering particle and is approximately  $\frac{1}{\gamma}$ . At ZEUS this radiation is detected  $L = 107.6\text{m}$  downstream by a detector with resolution  $r = 1.5\text{mm}$ , where the rms photon spot size  $\sigma_{phx}$  is related to the  $e^+$  emittance by

$$\epsilon_x^e = \beta_x^e \frac{\sigma_{phx}^2 - r^2 - (L\vartheta)^2}{L^2 + \beta_x^{e2}} . \quad (3.8)$$

In contrast to the more general evaluation in [13], here it was assumed that the dispersion, its slope,  $\alpha_x$ , and  $\alpha_y$  vanish at the interaction point. The so obtained emittances are stated in table (3.1). These emittance estimates support the conclusion that the ratio  $\epsilon_y^e/\epsilon_x^e$  has been reduced in the 72° optics to a satisfactory amount and that the large value for  $\epsilon_x^e$  obtained from the first luminosity scan at H1 is due to a large error of the corresponding proton wire scanner data. This allows the conclusion that the horizontal electron emittance is reduced to a satisfactory value by the stronger focusing of 72° rather than the standard 60° per FODO cell.

**Acknowledgment:** We appreciate the help of M. Bieler, P. Wesolowski, and R. Onken who took the data of the luminosity scans.

## 4 Measurement of beam Polarization in a $72^\circ/72^\circ$ spin matched optics

by E. Gianfelice, DESY Hamburg

Date: 2000, May. 13, 7am to May. 13, 4pm, Logbook XXXXIII, p. 129–131

Date: 2000, Aug. 27, 11pm to Aug. 29, 3pm, Logbook XLV, p. 45–55

In order to reach the  $e^\pm$  horizontal emittance of  $2.2 \times 10^{-8}$  rad m for the luminosity upgrade, beside an increase of the phase advance in the FODO cells from 60 to 72 degrees, it is planned to operate the machine with a RF frequency offset of about 250 Hz (corresponding to an energy offset of -0.1%). This means that the horizontal closed orbit will be non-zero by design.

The question arose which will be the impact of such an offset on the beam polarization. Machine studies aiming to explore this topics were carried out on May, 13 and on August, 30.

### 4.1 Introduction

The code SITF [14] was modified in order to simulate the RF offset by a momentum offset by requiring the 6-dimensional closed orbit to satisfy the additional conditions

$$\frac{\delta p}{p} = \text{constant}, \quad c\delta t = \alpha_p \frac{\delta p}{p} L \quad (4.1)$$

The (linear) polarization calculations show nearly no effect even in presence of realistic orbit distortions, whereas the non linear calculations with SITROS [14] show a dramatic drop of polarization (see figure 4.1 (a) and (b)).

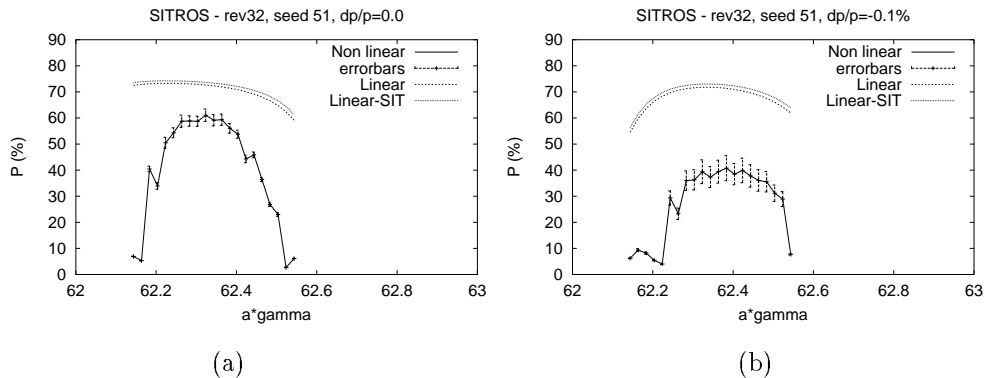


**Figure 4.1:** Polarization (linear and non-linear calculation) vs.  $a\gamma$  for a luminosity upgrade distorted optics (a) without RF shift and (b) in presence of a -0.1% energy error.

To clarify the quantitatively large disagreement between linear and non-linear calculations, a direct measurement of the effect was suitable.

According to the relation

$$\frac{\Delta p}{p} = \frac{\gamma_t^2 \gamma^2}{\gamma_t^2 - \gamma^2} \frac{\Delta f_{RF}}{f_{RF}} \quad (4.2)$$

the RF frequency shift produces also a shift of the energy. For  $\Delta f_{RF}=250$  Hz, the energy changes by -20 MeV for the 60°/60° optics ( $\gamma_t^2=1470.6$ ), and by -25 MeV for the 72°/72° one ( $\gamma_t^2=1832.9$ ). Such changes would have a large impact on the beam polarization. Therefore, for keeping the energy constant, the main dipole must be retuned by an amount given by

$$\Delta I_B = \gamma_t^2 I_B \frac{\Delta f_{RF}}{f_{RF}} . \quad (4.3)$$

The measurements were done without proton beam. It is known, indeed, that under beam-beam conditions polarization is very sensitive to energy and tunes. It is likely that under luminosity conditions an additional empirical dipole current optimization would have been needed. Moreover as long as the beams are synchronized it is not possible to change the RF frequency by large amounts.

## 4.2 May measurements

The May measurements were performed at the end of a luminosity run by using the usual 60°/60° luminosity optics. The starting polarization under luminosity conditions was around 53%. After dumping the proton beam at 12h00, polarization was clearly increasing; from figure 4.2 one can argue that the asymptotic polarization would have been around 60%; as the measurement would take anyway some hours and we were expecting to observe a large effect of the RF shift, we did not wait until polarization reached its asymptotic value.

As indicated by figure 4.3 the effect of the proton dump would overlap with the RF scan effect for the first hour.

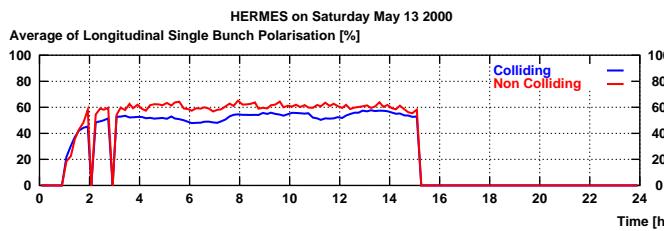


**Figure 4.2:** Measured Polarization vs. time.

The RF frequency offset was increased in steps up to 500 Hz. It was planned to change the dipole current in tree steps ( $\pm 0.45$  A around the linearly computed value) to account for a possible uncertainty in restoring the beam energy. In practice for each RF frequency step, only the lower of the tree dipole steps was performed. The results are quoted in table 4.1 .

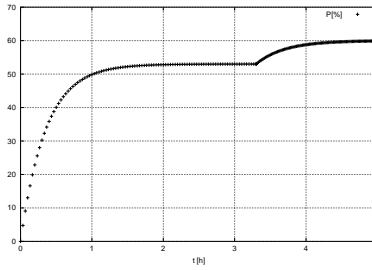


**Figure 4.3:** Polarization vs. time; a machine change after 3.3 hours leads from 53% to 60% polarization (simulation).

**Table 4.1:** May measurements

$t$	$\Delta f_{RF}$ (Hz)	$dp/p$ (%)	$ \Delta I_B $ (A)	$E_{TV}$ (GeV)	$\langle x \rangle$ (mm)	$P$ (%)
12h29	50	-0.015	0.488	27.599	-0.24	> 57
12h57	150	-0.044	2.319	27.606	-0.36	57
13h33	250	-0.073	4.150	27.614	-0.49	56
13h55	400	-0.117	6.958	27.626	-0.68	55
14h44	500	-0.147	9.277	27.637	-0.80	53

### 4.3 August measurements

In August, during dedicated machine studies, it was possible to establish a  $72^\circ/72^\circ$  spin matched luminosity test optics. According to the simulations results [15], the closed orbit was corrected down to  $x_{rms} \approx z_{rms} \approx 0.8$  mm; by optimizing energy and harmonic bumps was possible to reach about 60% beam polarization within 24 hours (see figure 4.4). Later, on the 30th, the effect of the RF shift on polarization was measured.

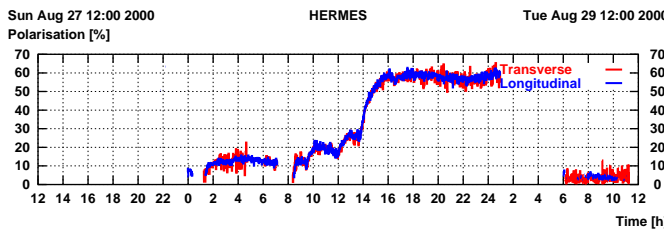


**Figure 4.4:** Polarization during optimization (energy and harmonic bumps scan). of the new  $72^\circ/72^\circ$  spin matched optics

The results are quoted in table 4.2. In the beginning of the measurement the injection tunes were kept by mistake. This is why the polarization values for  $\Delta f_{RF}=0$  and 100 Hz are missed. This time, for the reason explained above, for each RF step a small energy scan was performed.

**Table 4.2:** August measurements

$t$	$\Delta f_{RF}$ (Hz)	$dp/p\text{(\%)}$	$ \Delta I_B $ (A)	$E_{TV}$ (GeV)	$\langle x \rangle$ (mm)	$P$ (%)
8h18	200	-0.073	4.16	-	-0.28	$59.7 \pm 0.7$
8h52	200	-0.073	4.61	-	-0.30	$62.1 \pm 0.7$
9h00	300	-0.110	6.46	27.621	-0.43	$61.1 \pm 0.6$
9h32	300	-0.110	6.91	27.624	-0.43	$61.5 \pm 0.5$
9h54	350	-0.128	7.621	27.627	-0.50	$61.3 \pm 0.5$
10h33	350	-0.128	8.071	27.629	-0.50	$60.1 \pm 0.6$
11h00	400	-0.147	8.757	27.632	-0.57	$60.2 \pm 0.6$
11h33	400	-0.147	9.220	27.634	-0.57	$59.6 \pm 0.5$
12h05	400	-0.147	9.670	27.636	-0.57	$59.7 \pm 0.6$
12h28	500	-0.183	11.070	27.642	-0.70	$58.4 \pm 0.5$
12h58	500	-0.183	11.520	-	-0.71	$58.3 \pm 0.5$
13h30	500	-0.183	11.970	27.645	-0.71	$58.0 \pm 0.5$

#### 4.4 Conclusions

May and August measurements both clearly indicate that the effect of a RF frequency shift is not as large as expected in consequence of the non-linear calculations and that operating the machine with a RF frequency offset should be not a problem for polarization.

## 5 Measurements of Beam Lifetime versus RF Voltage at HERA-e

by F. Brinker and E. Gianfelice, DESY Hamburg

Date: 2000, May. 9, 1pm to May. 9, 11pm, Logbook XXXXIII, p. 107–110

On the 9th May evening, at the end of a luminosity run ( $I_e \approx 13$  mA), the lifetime of the  $e^+$  beam versus RF voltage has been measured. For polarization operation low betatron and synchrotron tunes are convenient; usually we set the cavity voltage so that  $f_s = 2.75$  kHz. The aim of the measurement was to find out how much we can lower the RF voltage before the  $e^+$  beam lifetime is reduced significantly. Usually the beam lifetime, limited by the scattering with the residual gas, is about 12 h at 15 mA.

The measured lifetime (current luminosity file with  $x_{rms} = 1.1$  mm, a typical value for luminosity operation) vs. RF voltage is shown in figure 5.1 together with the quantum lifetime computed with PETROS (ideal machine).

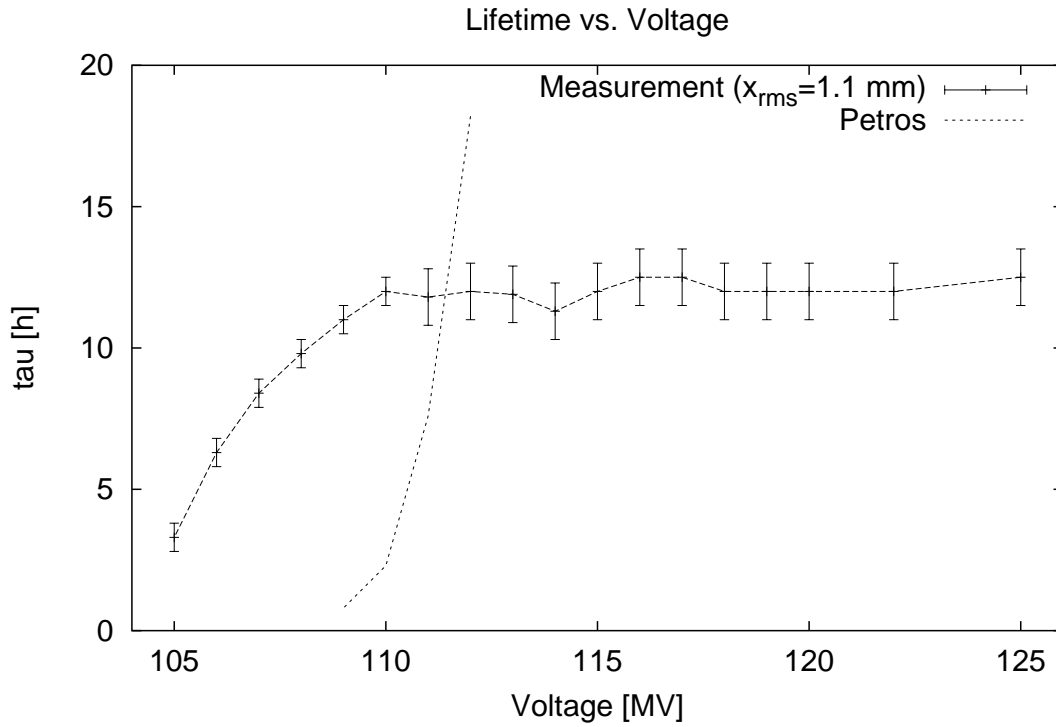


**Figure 5.1:** Lifetime vs. voltage

Figure 5.2 shows the measured synchrotron frequencies vs. RF voltage (the longitudinal FB was off) together with the theoretical values.

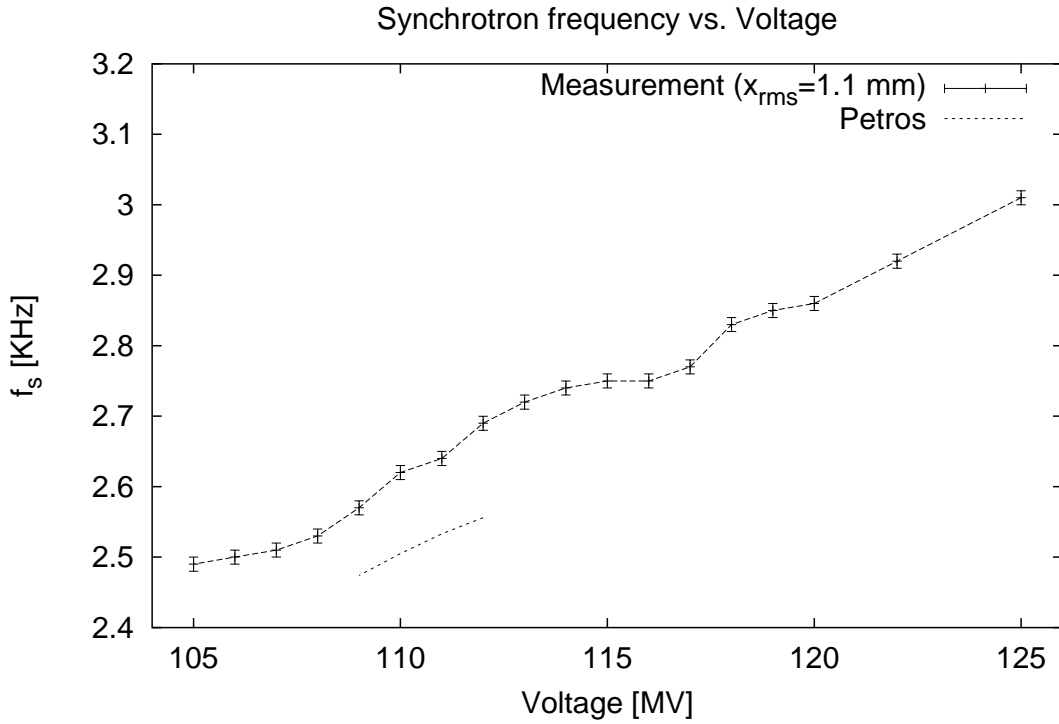


**Figure 5.2:** Synchrotron frequency vs. voltage

From the synchrotron frequency data one would get in average  $\alpha_p \approx 7.7 \times 10^{-4}$ ; the theoretical value is  $6.82 \times 10^{-4}$ . The measurement has been performed also after dumping the proton beam without significant change of the results. The measurement was repeated after turning on one horizontal corrector (NL593 CH) to estimate the effect of a longitudinal emittance increase due to a possible horizontal orbit shift. The results are shown in figure 5.3 for  $x_{rms} = 1.9$  mm. The synchrotron frequency did not change by distorting the orbit, indicating that the momentum compaction factor did not change.

The conclusion is that the actual circumferential voltage is somewhat underestimated: both lifetime and synchrotron tune are larger than one would expect even with a perfectly phased cavity system. When the polarization synchrotron frequency is set, the effect of an orbit shift may be harmful; the operator should watch out that  $x_{rms}$  never exceeds let us say 1.5 mm, which is suitable anyway also for the luminosity operation.

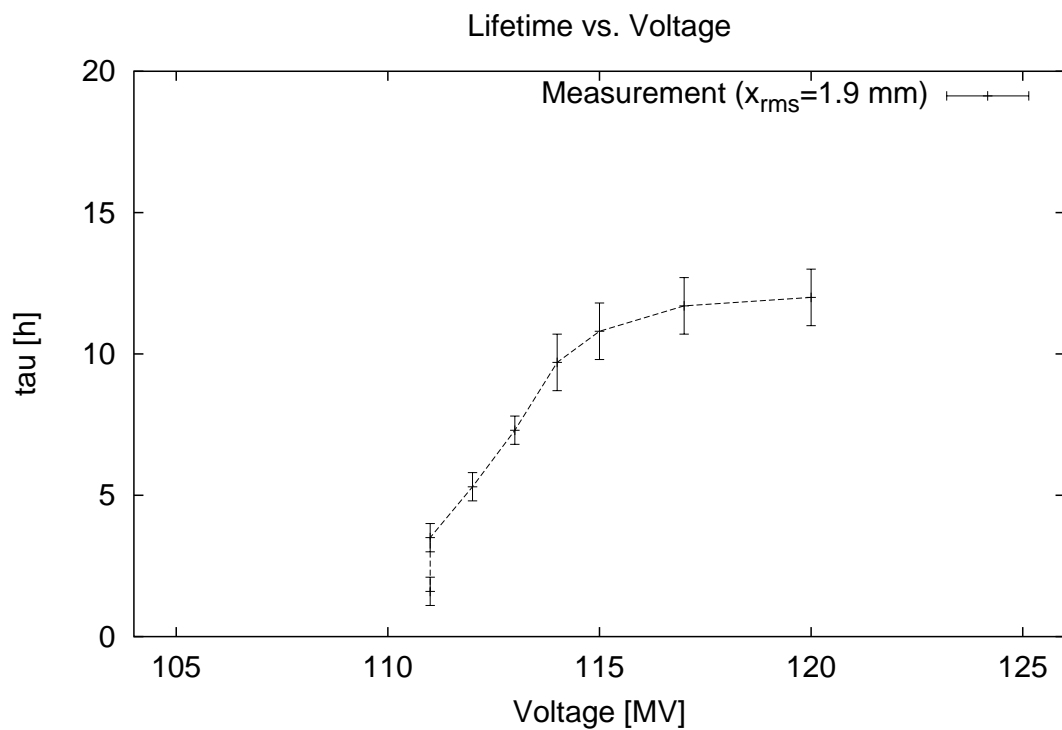


**Figure 5.3:** Lifetime vs. voltage for  $x_{rms} = 1.9\text{mm}$

## 6 Simultaneous Global Orbit and Dispersion Correction

by W. Decking, DESY Hamburg

Date: 2000, Aug. 02, 3pm to 6pm,

Date: 2000, Aug. 27, 12pm to 6pm, Logbook XLV, p. 40–44

We describe a global orbit and dispersion correction scheme based on the theoretical orbit and dispersion response functions and a solution of the normal equations with singular value decomposition.

### 6.1 Correction Method

A kick  $\theta_i$  applied at the steerer  $i$  changes the orbit  $x_j$  and the dispersion  $D_j$  at the beam position monitor  $j$ . The transformation of kick into orbit or dispersion is called the orbit response function  $S_{ij}$  respectively dispersion response function  $R_{ij}$ . The change of orbit and dispersion in all beam position monitors (BPMs) can be written in matrix notation as:

$$\begin{pmatrix} \mathbf{S} \\ \mathbf{R} \end{pmatrix} \vec{\theta} = \begin{pmatrix} \vec{x} \\ \vec{D} \end{pmatrix}.$$

The response matrices can be obtained analytically based on the knowledge of the optical functions, by direct measurement, and through model calculations using an optics program.

The correction algorithm now tries to simultaneously minimize in a least square sense the following equation:

$$\left| \begin{pmatrix} \mathbf{S} \\ \mathbf{R} \end{pmatrix} \vec{\theta} - \begin{pmatrix} \vec{\delta x} \\ \vec{\delta D} \end{pmatrix} \right| = \chi^2$$

where  $\vec{\delta x}$  and  $\vec{\delta D}$  are the desired changes in orbit and dispersion, usually the difference between the measured and the design value. This over-determined system of linear equations is solved with the help of singular value decomposition (SVD). SVD allows to sort the linear combinations of variables in order of their contribution to reduce  $\chi^2$ .

### 6.2 Measurement of Dispersion Function

The dispersion has been measured in the usual way by varying the RF frequency and recording the difference orbits. The RF frequency was changed in up to 10 steps between 0Hz and 500Hz. The dispersion at each BPM was obtained by fitting a straight line through the measurement points. Figure 6.1 shows a typical result for one BPM with a large horizontal dispersion. The results for all BPMs are displayed

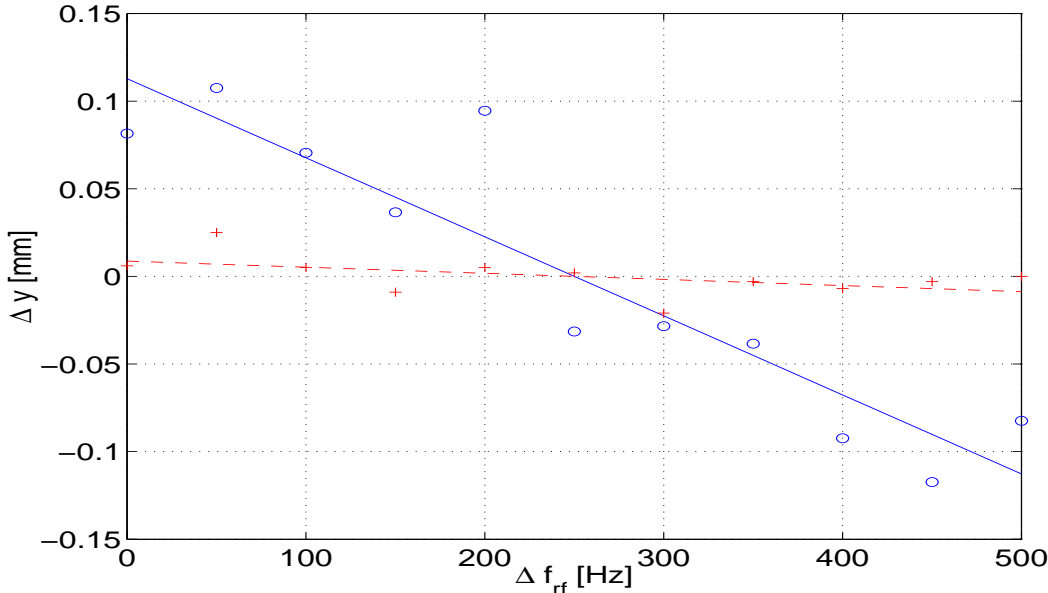


**Figure 6.1:** The orbit difference at two BPMs for different RF frequencies. Circles and crosses represent measurements, while the straight lines are linear fits to the data.

in figure 6.2 together with the theoretical dispersion. The error bars are calculated from the linear fits.

For three different corrector magnets we have measured the orbit and dispersion response matrix and compared it with the model calculations. The current of the corrector magnet was changed by  $\approx 0.1\text{A}$  and the dispersion was measured before and after the change. The amplitude of the measured orbit response function has been fitted in such a way that its rms value is the same as for the theoretical function. This procedure should yield the corrector conversion factor. The amplitude of the measured dispersion response has been treated the same way. The two thus obtained factors should be the same. In all three measurements the factor obtained from the dispersion measurement is two times smaller than the one obtained from the orbit measurement. The reason for this has still to be determined. Figure 6.3 shows the comparison of the response functions for one corrector. The agreement of the orbit response is extremely good, which means that the accelerator model agrees with the real machine. The agreement of the dispersion response is not quite as accurate.

### 6.3 Correction of the Dispersion and Orbit

The dispersion and orbit has been corrected simultaneously in the optics which is referred to as HESPIN7272. The correction algorithm was extended by adding a weighting factor between the orbit and dispersion correction. This factor should take care of the amplitude difference between the orbit ( $y_{rms} \approx 1\text{mm}$ ) and dispersion ( $D_{y,rms} \approx 40\text{mm}$ ). The dispersion could be corrected down to  $D_{y,rms} \approx 20\text{mm}$  with no change in the rms of the vertical orbit. For this correction only the largest 50 singular values have been used. The largest 20 singular values contribute strongest

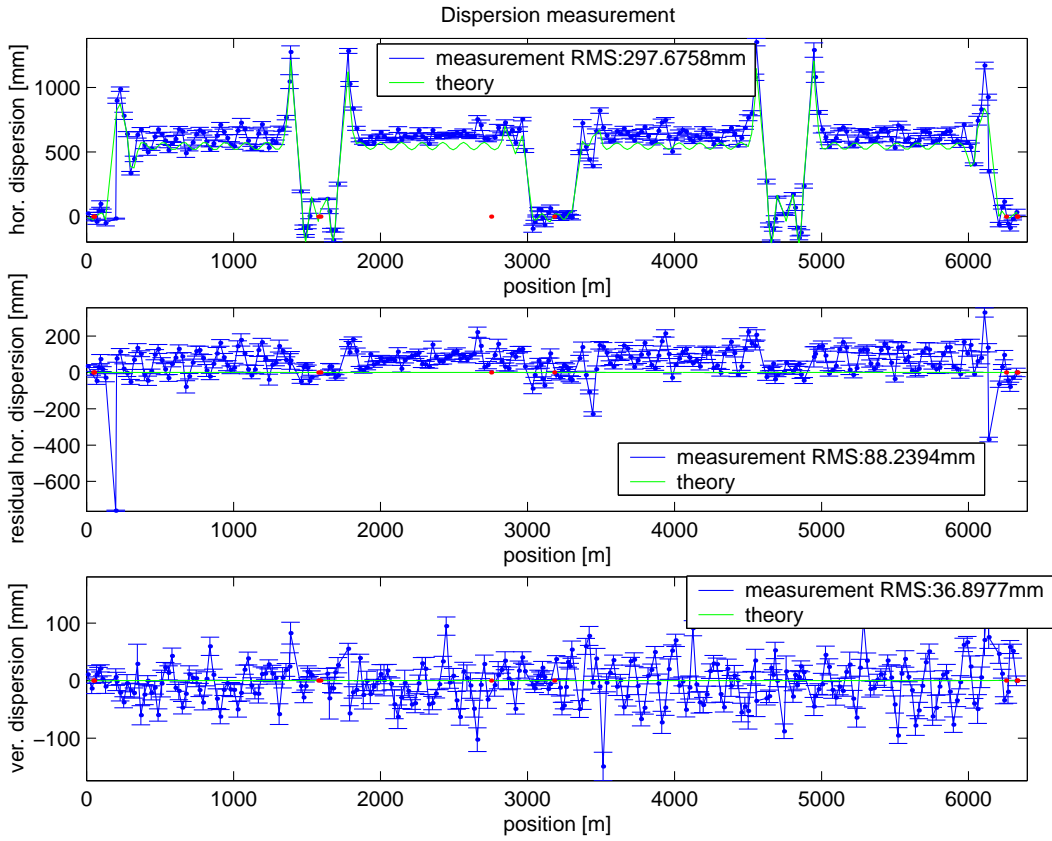


**Figure 6.2:** Result of dispersion measurement with optic HEINJ on August 02. Upper curve is the horizontal dispersion, middle curve the residual horizontal dispersion after subtracting the theoretical dispersion, and lower curve the vertical dispersion.

to the correction (see figure 6.4)

Figure 6.5 shows the result of the dispersion correction.

The corrector changes are rather small ( $\Delta I_{VC;rms} \approx 0.017\text{mA}$ , or  $\Delta\theta_{VC;rms} \approx 0.0025\text{mrad}$ ). This may point towards problems with the stability of such a correction.

The correction algorithm and the routines to analyze the dispersion measurements have been programmed in MATLAB. For routine operation they should be included in the standard orbit correction package.

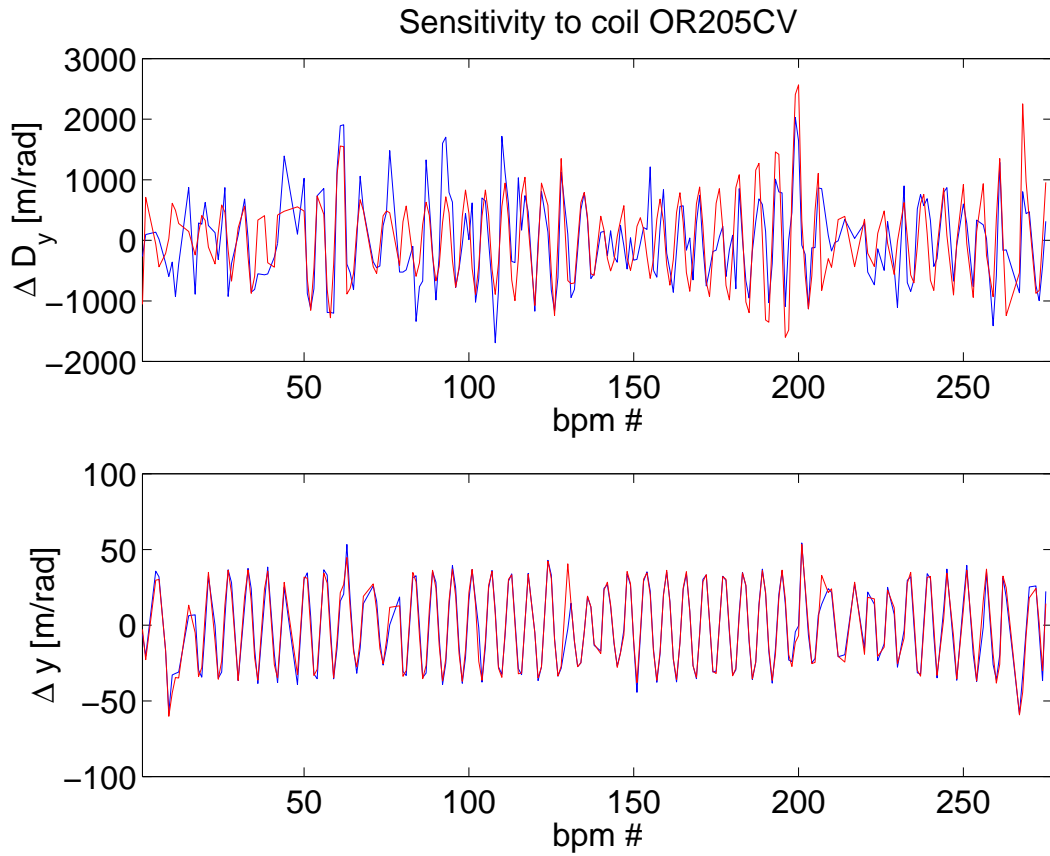


**Figure 6.3:** Comparison of the dispersion response (upper) and orbit response matrix (lower) for corrector OR205CV. Black curve is the measurement, while gray curve shows the model calculation.

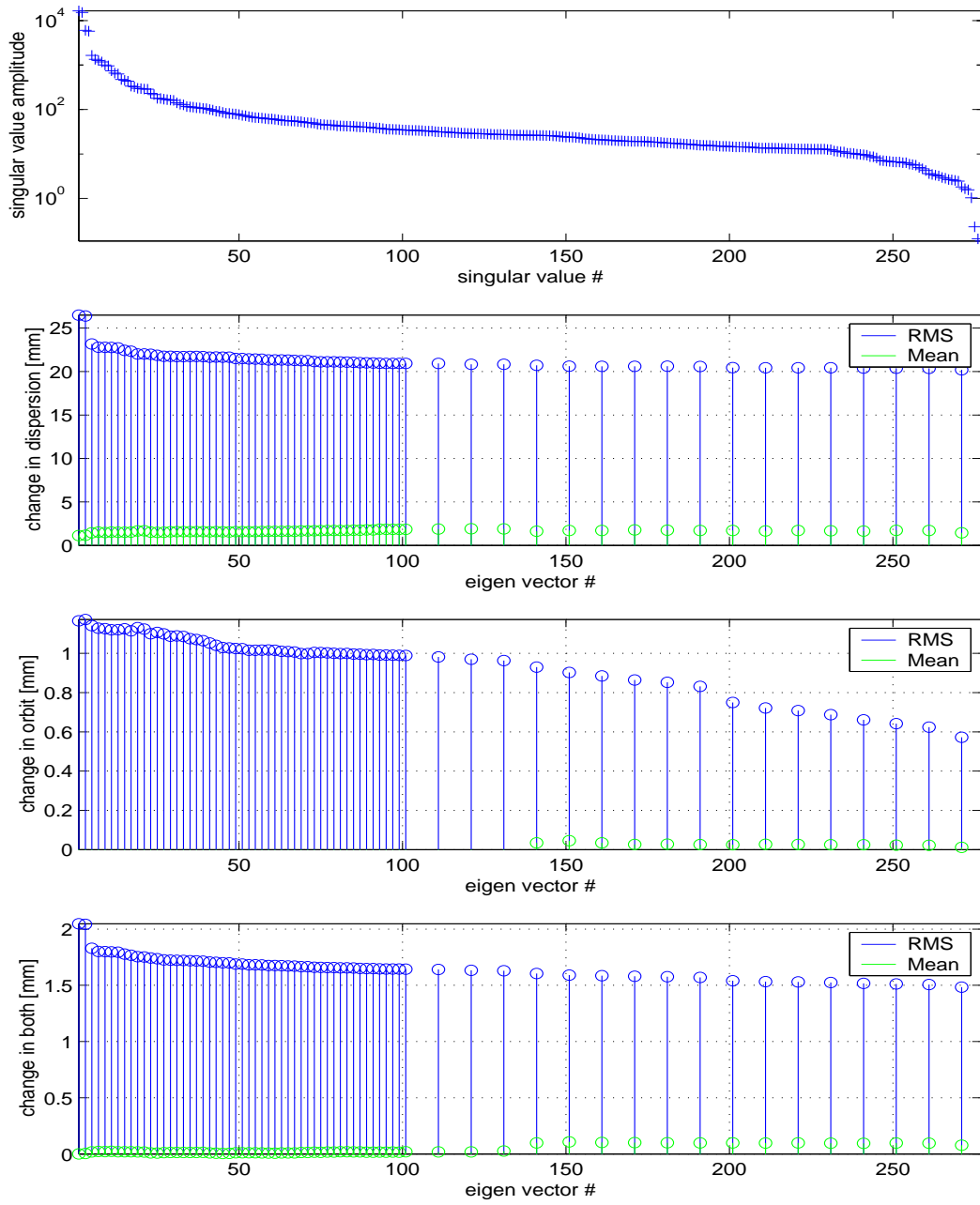


**Figure 6.4:** Singular value amplitude (upper) and cumulative effect of a correction using a certain number of eigenvalues on the dispersion (upper middle), orbit (lower middle), and the combination of both (lower). The weighting between dispersion and orbit contribution to the correction was 0.1.

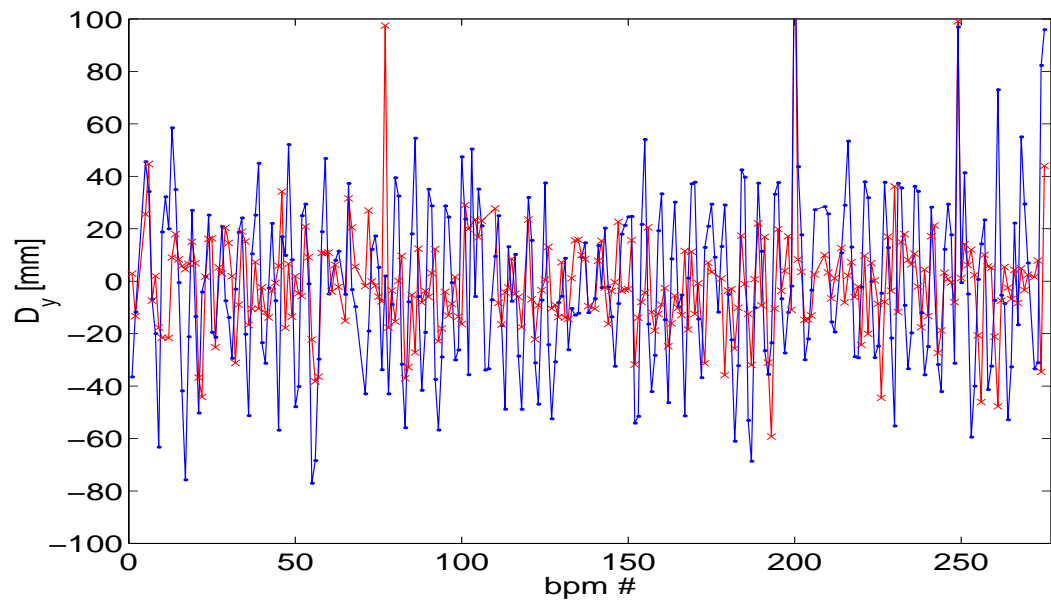


**Figure 6.5:** Vertical Dispersion before (black) and after correction (gray).

## 7 Orbit Effect of a Misaligned Magnet Girder

by F.Stulle, DESY Hamburg

Date: 1999, Dec. 16, 7am to Dec. 17, 7am, Logbook XXXXI, p. 46–54

Date: 1999, Dec. 18, 2pm to Dec. 18, 11pm, Logbook XXXXI, p. 70–73

For the upgraded HERA interaction regions a major concern will be to keep the transverse position of the magnet girders carrying the low- $\beta$ -quadrupoles within the tighter tolerances. These magnet girders can be moved by stepper motors, once the size of their misalignment is known. Therefore a special, beam independent measurement system will be installed which can measure the magnet positions directly. Additionally it would be good to get the misalignments from an analysis of the beam position monitors. Since the normal orbit correction algorithms are not well suited for finding the exact location of errors, a new method was developed which can locate orbit errors by analyzing the phase and the amplitude of the betatron oscillation. To test this algorithm a magnet girder was moved to simulate an error.

### 7.1 Introduction

Standard orbit correction algorithms try to minimize the effect of orbit distortions without locating the true position of the errors (e.g. MICADO [16]). This has been a good approach in most cases but might not be sufficient if other issues besides orbit distortions have to be considered. For example, synchrotron radiation in the upgraded HERA interaction regions can be more harmful than large orbit deviations along the ring. For these reasons an algorithm capable of locating errors has been developed.

Based on the principles of linear beam optics, phase jumps in the closed orbit can be used to detect misaligned quadrupoles. Additionally errors in quadrupole strength and sextupole misalignment will lead to similar effects if closed orbit distortions are present [17]. The orbit  $Y(\Phi)$  is a superposition of oscillations generated by kicks of the form  $\Delta x' = k l \Delta x$  produced by off-center quadrupoles of strength  $k$  and length  $l$ . In general the distorted orbit can be calculated by:

$$\frac{Y(\phi)}{\sqrt{\beta(\Phi)}} = \frac{1}{2 \sin \pi Q} \sum_i \sqrt{\beta_i} \Delta x'_i \cos(|\Phi_i - \Phi| - \pi Q) \quad (7.1)$$

In this normalized form it is possible to write  $Y(\Phi)$  as an oscillation with amplitude  $A(\Phi)$  and phase angle  $\delta(\Phi)$  depending on the position in terms of the betatron phase  $\Phi$  of the unperturbed optics. Then the effect of a single distortion is a harmonic

oscillation of constant amplitude  $B_i$  but with a phase angle  $\psi_i(\Phi)$  depending on the position:

$$\begin{aligned} \frac{Y(\phi)}{\sqrt{\beta(\Phi)}} &= A(\Phi) \cos(\Phi + \delta(\Phi)) \\ &= \sum_i B_i \cos(\Phi + \psi_i(\Phi)) \end{aligned}$$

The amplitudes  $B_i$  and phase angles  $\psi_i(\Phi)$  of the different distortions vary with the strength and location of the kicks.

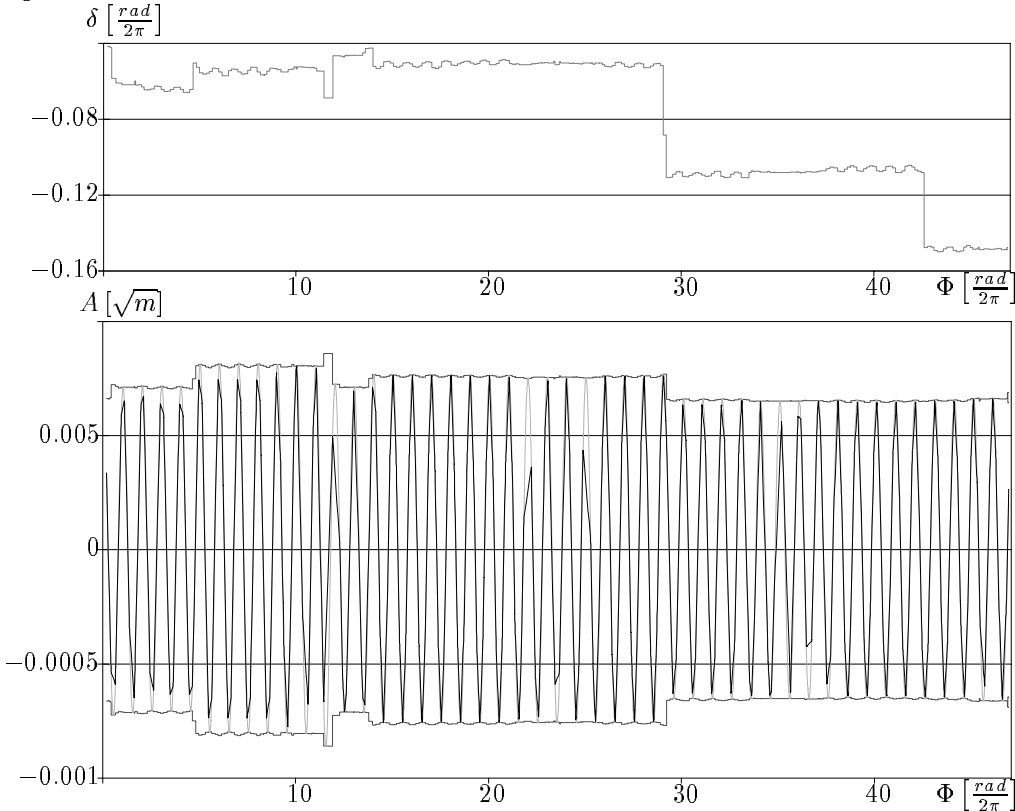


**Figure 7.1:** In the upper plot the phase angle  $\delta$  is plotted, the lower plot shows the amplitude  $A$ , the calculated oscillation (dashed) and the BPM-values (solid). In this simulated data for the HERA electron ring seven errors were applied. They can be found as steps in the phase angle  $\delta$  at  $\Phi = 0.5, 4.7, 11.6, 12.1, 14.0, 29.2, 42.7 \frac{rad}{2\pi}$ . The error at  $\Phi = 42.7 \frac{rad}{2\pi}$  does not change the amplitude.

At the position of an error there will be a phase jump in the corresponding oscillation and therefore also in the superimposed orbit oscillation. Moreover, in general a change in the amplitude will occur. By calculating the phase angle  $\delta(\Phi)$  and the amplitude  $A(\Phi)$  from the normalized BPM-values it is possible to locate these phase jumps and amplitude changes and thus locate errors.

The values of  $A$  and  $\delta$  are calculated by fitting  $A_i \cos(\Phi + \delta_i)$  to every two consecutive normalized BPM-values  $y_i$  and  $y_{i+1}$ . One thereby assumes that no error

occurs between  $\Phi_i$  and  $\Phi_{i+1}$ , and therefore  $A_i$  and  $\delta_i$  should have the same values at both positions:

$$\begin{aligned} y_i &= A_i \cos(\Phi_i + \delta_i) \\ y_{i+1} &= A_i \cos(\Phi_{i+1} + \delta_i) \end{aligned}$$

By solving the system of two equations one finds the following solutions for the amplitude and the phase angle:

$$\begin{aligned} A_i &= \frac{\sqrt{y_i^2 + y_{i+1}^2 - 2y_i y_{i+1} \cos(\Phi_{i+1} - \Phi_i)}}{\sin(\Phi_{i+1} - \Phi_i)} \\ \delta_i &= \begin{cases} \arccos \frac{y_i}{A_i} - \Phi_i \\ -\arccos \frac{y_i}{A_i} - \Phi_i \end{cases} \end{aligned}$$

The results can be plotted against the betatron phase  $\Phi$  (Fig. 7.1). Almost every kick by misaligned quadrupols will show up as a step in the graphs of the phase angle and the amplitude. Only in some special cases the step can be absent in one of them, but never in both.

In a similar way it is also possible to detect localized sources of coupling and focusing perturbations as is shown in [17].

## 7.2 Measurements

The idea of the measurements during the machine studies was, to test the new algorithm with real HERA data. Since the reason for its development was to find out if a magnet girder is misaligned, a magnet girder was moved to simulate an error. During the machine studies the movement of the girder could only be observed by the wire measurement system (ODM) and the hydrostatic leveling system (HLS), since the magnet girders are behind the concrete shielding. These two independent measurements are necessary because it is not known how far the girder will move with the steps of the motor and if the stepper motors will move with every single impulse from the control panel. Therefore both systems should be available to avoid mechanical damage of the detector and of the vacuum system. At ZEUS the ODM was broken, so it was chosen to move the girder at the left side of the H1 detector. For this movement the two motors at the front end of the girder were used. They are placed under the A-shaped support carrying the girder (Fig. 7.2).

It was planned to take all data before the ramp of the electrons at 12GeV, starting with reference values for all systems involved (i.e. ODM, HLS and BPM) when no changes were made to the machine. Then the beam should be dumped to move the girder. The movement of the girders had to be controled from an electronic rack in the HERA tunnel. This was the only possibility to connect the two SEDAC cassettes which control the stepper motors. Two control panels were needed to move the two motors at the same time, to avoid horizontal movement of the girder. Now the beam was planned to be re-injected to take the next set of data. This procedure should have been repeated some times and from the analysis of the resulting set of data one would have seen if the effect of the girder movement was as expected.

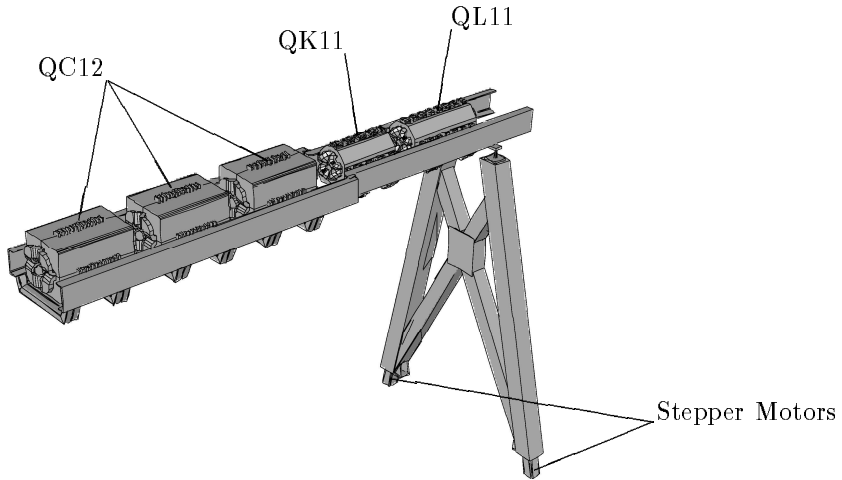


**Figure 7.2:** On the girders five quadrupole magnets are mounted. The stepper motors used for the movement are shown.

On the scheduled shift the wire measurement system was broken. The only working measurement system was the hydrostatic leveling system. Nevertheless it was decided to start the girder movement. Since the whole procedure for one girder position includes dumping the electron beam, moving the girder and re-injecting the beam it was only possible to take the reference data and the data for one girder position.

### 7.3 Analysis

The girder at the left side of H1 was lifted with the stepper motors under the support at the front end until the dial gauge of the HLS changed by  $0.1\text{mm}$ . Since the dial gauge is nearer to the detector than the support, the real movement was only  $0.08\text{mm}$ . This corresponds with a movement of the magnets QL11, QK11, QC12, QC12, QC12 by  $0.09\text{mm}$ ,  $0.07\text{mm}$ ,  $0.04\text{mm}$ ,  $0.02\text{mm}$  and  $-0.01\text{mm}$ .

The orbit distortion was small and the rms-amplitude of the difference orbit was only  $0.3\text{mm}$ . Therefore the noise in the calculated amplitude  $A$  is quiet large, however the noise in the phase angle  $\delta$  is smaller (Fig. 7.3).

Comparing the two amplitudes in Fig. 7.3(bottom) the simulated amplitude seems to be smaller than the average of the measured amplitudes, that would mean the girder has moved a bit more then expected. Calculating the movement of the girder from the measured values results in  $0.09\text{mm}$  for the raise of the support. This value corresponds to a value measured by the dial gauge of  $0.11\text{mm}$  which lies within the accuracy of the dial gauge of  $\pm 0.01\text{mm}$ .

Since the five magnets on the girder are approximately at the same betatron phase, it is not possible to see that the error does not occur in a single magnet but consists of five errors. The four rear magnets are shifted less than the magnet QL11 and partly cancel each others effect because they have different polarity and one is shifted in the opposite direction. This is why the magnet QL11 has by far the

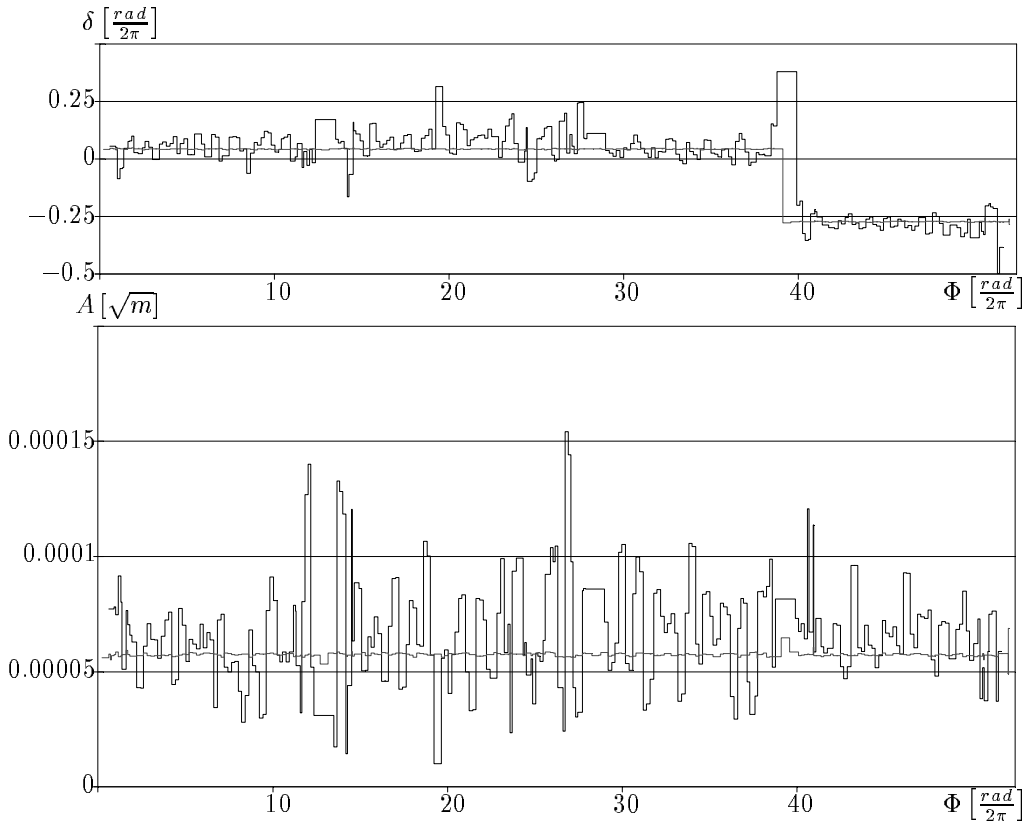


**Figure 7.3:** The phase angle  $\delta$  calculated from the measured data (solid) in the upper plot has a step at the location of the girder and agrees well with the simulated graph (dashed). The measured amplitude shown in the lower plot (solid) has a large variation but its average also corresponds quite well with the simulated graph (dashed).

largest influence on the orbit.

The height of the step in the phase angle  $\delta$  corresponds well with the simulated data, the single high value in the region of the error is a systematic characteristic of this algorithm for the calculation of the phase angle  $\delta$  and the amplitude  $A$ .

## 8 Measurement of the Beam Response Matrix of HERA-e

by A. M. Xiao, DESY Hamburg

Date: 2000, Aug. 26, 7am to Aug. 26, 3pm, Logbook XLV, p. 30–31

Revealing beam optic properties and restoring them for a real accelerator, are becoming more interesting topics in both theory and practice. Some new methods [18, 19] have been presented in recent years. The common point of these methods is to measure a beam response matrix for various kinds of disturbances, and then to compare it with the matrix obtained from optical theory.

To obtain this beam response matrix for HERA, an automatic system for controlling the steering magnets and for taking BPM data was set up, so that we could measure the closed beam orbit changes for a change of each steering magnet. To increase the accuracy, we stored the average of 15 orbit measurements for 1 changed steering magnet. This procedure for measuring the whole response matrix required about 3 hours.

A code was written to fit these measurements to linear transport matrices. In those regions where these matrices disagree with the theoretical transport matrices, magnet errors might be revealed.

### 8.1 Linear closed orbit fitting

The closed beam orbit changes  $b_{i,j} \cdot \theta_j$  at the  $i$ th BPM was stored after the  $j$ th steering magnet had been changed to produce an angle of  $\theta_j$  in the closed orbit. Scanning all steering magnets around the ring, the beam response matrix has been built for all BPMs and for all steering magnets, at both the vertical and horizontal plane:

$$B = \begin{bmatrix} B_{M \times K_x}^x & B_{M \times K_y}^x \\ B_{M \times K_x}^y & B_{M \times K_y}^y \end{bmatrix} = \{b_{i,j}\} , \quad (8.1)$$

where  $M$  is the total number of BPMs;  $K_x$  ( $K_y$ ) is the total number of steering magnets in the horizontal (vertical) plane.  $B^x$  ( $B^y$ ) denotes the measured horizontal (vertical) response matrix and the lower indices describe the dimensionalities of the matrices.

After having measured the matrix  $B$ , the first thing we would like to know is if it can be described by linear theory. In un-coupled linear optics theory, the response function due to a kick error can be written as

$$b_{i,j} = \frac{\sqrt{\beta_i \beta_j}}{2 \sin(\pi \mu)} \cdot \cos(|\varphi_i - \varphi_j| - \pi \mu) . \quad (8.2)$$

The matrix element  $b_{i,j}$  is the response function at the  $i$ th BPM,  $\mu$  is the tune,  $\beta_i$ ,  $\beta_j$ ,  $\varphi_i$  and  $\varphi_j$  are the optical beta functions and the betatron phase advances at the positions of BPMs and steering magnets, respectively. For the following analysis we assume all matrices not to be coupled, i.e.  $B_{M \times K_y}^x = 0$  and  $B_{M \times K_x}^y = 0$ .

In each direction (horizontal or vertical), we have totally  $M \times K$  such equations, but only  $2K + 2M + 1$  unknown variables ( $\beta_i$ ,  $\beta_j$ ,  $\varphi_i$ ,  $\varphi_j$  and  $\mu$ ). In order to obtain these variables, the nonlinear equations (8.2) of these variables have to be solved. We have used Newton's method to solve these equations. Since these equations are over determined, they can not be solved directly, but we rather minimized the difference between the left and right side of equation (8.2) in a least square sense. To simplify the procedure, a subset of  $B$  is used in our fitting routine. One could choose a subset  $\bar{b}_{k \times m}$  of any size as long as  $k \times m \geq 2k + 2m + 1$ . We have chosen

$$\bar{b}_{6 \times 7} = \begin{bmatrix} b_{m_i, k_i} & \cdots & b_{m_i, k_i+7} \\ \vdots & & \vdots \\ b_{m_i+6, k_i} & \cdots & b_{m_i+6, k_i+7} \end{bmatrix}. \quad (8.3)$$

The complete matrix  $B$  has been covered with  $6 \times 7$  patches by letting  $k_i$  vary from 1 to  $K_x - 7$  (or  $K_y - 7$ ), and  $m_i$  from 1 to  $M - 6$ . As final results of  $\mu$ ,  $\beta_i$ ,  $\beta_j$ ,  $\varphi_i$  and  $\varphi_j$  we took the average of the results from each patch. The RMS fitting error

$$\text{Err} = \sqrt{\frac{\sum_{i=1}^6 \sum_{j=1}^7 (b_{i,j}^{\text{ft.}} - b_{i,j}^{\text{meas.}})^2}{42}} \quad (8.4)$$

has also been calculated. The results show that for some patches of the BPM response matrix of HERA the fitting errors are less than 0.06 mm, which is about the BPM resolution; for other sections the fitting results couldn't converge to such small values, see figure 8.1.

## 8.2 Measured transport matrix: $m_{11}$ and $m_{12}$

After fitting the measured data to linear optics, we found that the fitted optics is in some regions almost the same as the theoretical optics, so these regions can be treated as perfect (no magnet errors) and the theoretical transport matrices can be used to obtain initial values  $(x_0, x'_0)$  at the entrance plane  $l_0$  of this perfect section,

$$x_i^{\text{meas.}} = m_{11}^{\text{theo.}}(l_0, l_i) \cdot x_0 + m_{12}^{\text{theo.}}(l_0, l_i) \cdot x'_0. \quad (8.5)$$

Here  $m_{11}$  and  $m_{12}$  are the theoretical transport matrix elements from the start point at  $l_0$  to the  $i$ th BPM at  $l_i$  where  $x_i$  is measured. From there on we treat our ring as a transport line starting at the point  $l_0$ . In order to reduce errors, we used 10 BPMs to fit  $x_0$  and  $x'_0$  at the first BPM in a least square sense,  $|X^{\text{meas.}} - M \cdot X_0|^2 \rightarrow \text{minimal}$  with

$$X^{\text{meas.}} = \begin{pmatrix} x_0^{\text{meas.}} \\ \vdots \\ x_{10}^{\text{meas.}} \end{pmatrix}, \quad \begin{bmatrix} m_{11}^{\text{theo.}}(l_0, l_0) & m_{11}^{\text{theo.}}(l_0, l_0) \\ \vdots & \vdots \\ m_{11}^{\text{theo.}}(l_0, l_{10}) & m_{11}^{\text{theo.}}(l_0, l_{10}) \end{bmatrix} \cdot \begin{pmatrix} x_0 \\ x'_0 \end{pmatrix} = M \cdot X_0. \quad (8.6)$$

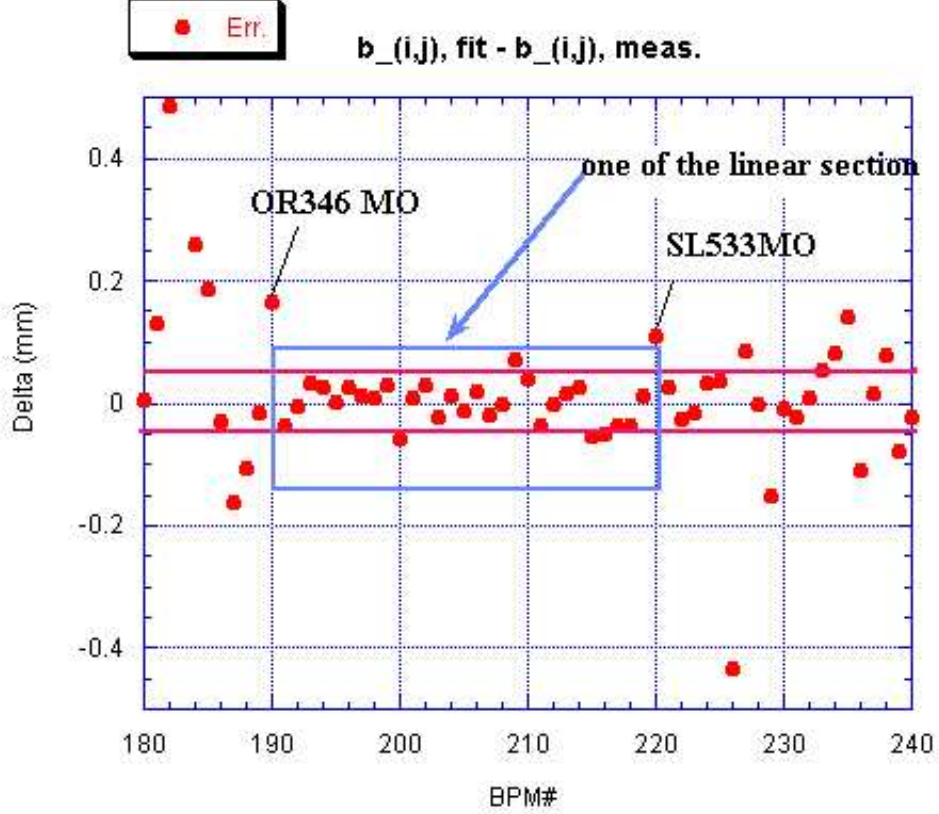


**Figure 8.1:** The difference between the theoretical and the measured BPM response matrix elements  $b_{i,j}$ . This difference can be used to identify parts of HERA which correspond very closely to linear optics theory.

The singular value decomposition (SVD) method was used to find a least square solution of  $X_0$ . In this method, the  $10 \times 2$  matrix  $M$  is decomposed into the product  $U_{2 \times 10} W_{2 \times 2} V_{2 \times 2}^T$  of a column orthogonal matrix, a diagonal matrix and a orthogonal matrix. The least square solution is then given by  $X_0 = V_{2 \times 2} W_{2 \times 2}^{-1} U_{2 \times 10}^T X^{\text{meas.}}$ . This can easily be shown to be equivalent to the following representation of the least square solution:  $X_0 = (M^T M)^{-1} M^T X^{\text{meas.}}$ .

In the experiment, we have set  $\sqrt{\beta_j^{\text{theo.}}} \cdot \theta_j$  to the same value for all steering magnets, and linear optics therefore predicts the following closed orbit at the section  $l_0$ :

$$x_{0,j} = \frac{\sqrt{\beta_0 \beta_j}}{2 \sin(\pi \mu)} \cdot \theta_j \cdot \cos(|\varphi_0 - \varphi_j| - \pi \mu) = A_j \sqrt{\beta_0} \cdot \cos(\varphi_0 + \phi_j) , \quad (8.7)$$

$$x'_{0,j} = -\frac{A_j}{\sqrt{\beta_0}} [\alpha_0 \cos(\varphi_0 + \phi_j) + \sin(\varphi_0 + \phi_j)] , \quad (8.8)$$

$$A_j = \frac{\sqrt{\beta_j} \theta_j}{2 \sin(\pi \mu)} . \quad (8.9)$$

Here  $\beta_0$  and  $\alpha_0$  are the Twiss parameters at the start point  $l_0$  of the perfect section. For an ideal machine, all  $A_j$  would be the same, and if we plot  $x'_{0,j}$  vs.  $x_{0,j}$  for all steering magnets, all points would be positioned on the ellipse

$$(x_0, x'_0) \begin{pmatrix} \gamma_0 & \alpha_0 \\ \alpha_0 & \beta_0 \end{pmatrix} \begin{pmatrix} x_0 \\ x'_0 \end{pmatrix} = A_i^2. \quad (8.10)$$

Since the optic functions at the position of the corrector  $j$  do not always agree with the design values, the edge of ellipse will spread to some width, see figure 8.2. This width indicates beta-beat or phase errors at the position of the correctors. This information is quite useful for a closed beam orbit correction procedure.

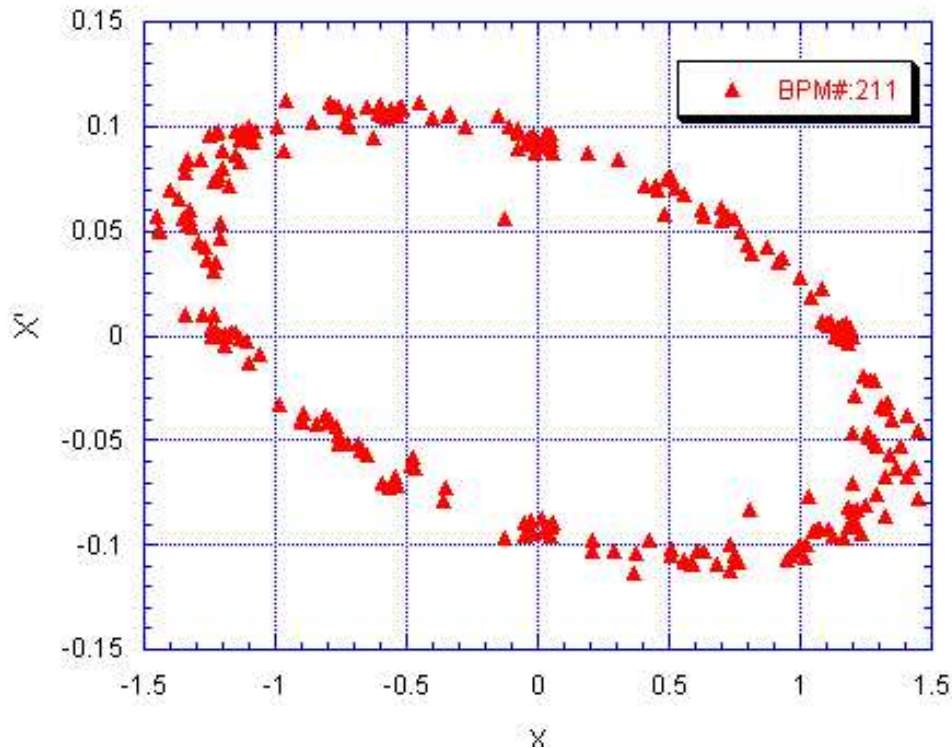


**Figure 8.2:** Initial beam ellipse at BPM# 211.

As before, the initial orbit conditions  $(x_0^j, x'_0^j)$  at  $l_0$  were obtained from the BPM readings  $x_i$  between BPM# 202 to BPM# 211 for each changed corrector magnet  $j$ . Then the transport matrix elements  $m_{11(l_0, l_i)}$  and  $m_{12(l_0, l_i)}$  were obtained by solving the linear equations for several  $j$  in a least square sense,

$$x_{i,j}^{\text{meas.}} = m_{11}^{\text{meas.}}(l_0, l_i) \cdot x_0^j + m_{12}^{\text{meas.}}(l_0, l_i) \cdot x'_0^j. \quad (8.11)$$

The resulting matrix elements are shown in figure 8.3.

In this figure, we see some disagreements between the measured  $m_{11}$  and  $m_{12}$  and the theoretical values. This disagreement can give us a clue about errors around the ring. A simulation routine is under development to find such errors. After that, we could restore the optic of HERA-e closer to its design value. This work is under way and will be reported later.

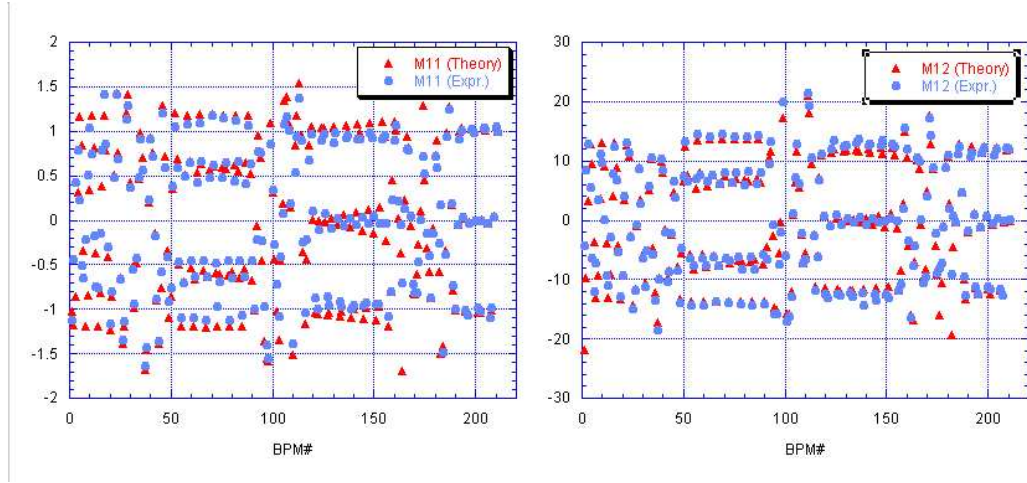


**Figure 8.3:** Transport matrix  $m_{11}$  and  $m_{12}$  from BPM# 211.

**Acknowledgment:** We appreciate the help of J. Maass who set up the automatic magnet controlling and data taking code.

C. Montag, K. Ehret, M. Funcke

## 9 Systematic Tune Modulation Frequency Scans

Date: 2000, Aug. 29, 7am to Aug. 29, 3pm, Logbook XLV, p. 51

During the machine study period in September 2000 the effect of various tune modulation frequency parameters on the HERA-B interaction rate stability was systematically studied.

### 9.1 Introduction

In order to stabilize the interaction rate at the internal wire target of the HERA-B experiment, various methods have been tested in recent years. Since HERA is not operated in any dedicated mode for HERA-B only but simultaneously has to provide colliding beams for the two experiments H1 and ZEUS, any “tail shaping” activities must not lead to any detrimental effects such as luminosity degradation or enhanced background. As previous experiments [20] indicated, these conditions are fulfilled by the application of tune modulation in the presence of beam-beam interactions.

Tune modulation creates resonance sidebands in the transverse plane. The corresponding resonance condition can be expressed as [21]

$$k_x \cdot Q_x + k_y \cdot Q_y + l \cdot \frac{f_{\text{mod}}}{f_{\text{rev}}} = m, \quad k_x, k_y, l, m \quad \text{integer}, \quad (9.1)$$

where  $Q_x$ ,  $Q_y$  are the horizontal and vertical betatron tune, and  $f_{\text{mod}}$ ,  $f_{\text{rev}}$  are the modulation frequency and the revolution frequency, respectively.

### 9.2 Experiments

During the previous machine study period in December 1999 the feasibility of stabilizing the HERA-B interaction rate by means of tune modulation was studied [20]. Only very few parameter sets could be tried due to lack of time. Therefore a more systematic study has been performed in September 2000.

In both experiments the tunes were set to  $Q_x = .297$  horizontally and  $Q_y = .292$  vertically. Since the aim was to resonantly excite particles in the transverse beam tails without disturbing the beam core, the beam-beam tune shift has to be taken into account in the resonance condition, equation (9.1). With tune shifts of  $\Delta Q_y = -0.5 \cdot 10^{-3}$  and  $\Delta Q_x = -1.2 \cdot 10^{-3}$ , the betatron tunes of particles in the tails are therefore  $Q_{x,\text{tail}} = Q_x - \Delta Q_x = .2982$  and  $Q_{y,\text{tail}} = Q_y - \Delta Q_y = .2925$ . The closest even order resonances are therefore  $Q_{x,\text{res}} = 3/10 = 0.3$  and  $Q_{y,\text{res}} = 4/14 = 0.286$ . The resonance condition is thus fulfilled for  $f_{\text{mod}} \approx 85 \text{ Hz}$  in the horizontal and  $f_{\text{mod}} \approx 320 \text{ Hz}$  in the vertical plane.

Figure 9.1 shows the HERA-B interaction rates achieved with disabled wire position control, i. e. at a fixed target wire position. These measurements already indicate a strong dependency of the interaction rate on the frequency set chosen. For

example, the HERA-B interaction rate achieved with two simultaneously applied modulation frequencies of 10 Hz and 190 Hz and a total magnet current of 1.03 A is significantly larger than the corresponding value for 10 Hz only and an even higher magnet current of 1.25 A. It was therefore expected that this effect should also be observable in the resulting interaction rate stability when the target wire position feedback is operational. For this purpose a proton beam of some 90 mA in 180 bunches was brought into collision with a 20 mA positron beam, and the resulting relative interaction rate width

$$\sigma_{\text{rel}} = \frac{\sqrt{\langle (\dot{N}_{\text{interaction}} - \langle \dot{N}_{\text{interaction}} \rangle)^2 \rangle}}{\langle \dot{N}_{\text{interaction}} \rangle} \quad (9.2)$$

at the target wire “Above I” was measured. A frequency modulation signal consisting of two sinusoidal signals,

$$U(t) = \hat{U} \cdot [\sin(2\pi f_1 t) + \sin(2\pi f_2 t)] \quad (9.3)$$

was applied at the additional input of the quadrupole magnet power supplies QP40 and QP42 in HERA West.

Since the HERA-B target wire position feedback is based on a sampling rate of 10 Hz, the lower frequency component  $f_1$  was set to 12 Hz in order to avoid artificial effects. Figure 9.2 shows the resulting relative rms rate widths for three different tune modulation amplitudes and a frequency range  $f_2 = 0 \dots 500$  Hz. In contrast to the measurements with fixed wire position (Fig. 9.1), no frequency dependency was detected. Even a single 12 Hz modulation without any second frequency component leads to similar interaction rate stabilization. The interaction rate width  $\sigma_{\text{rel}}$  depends strongly on the tune modulation depth  $\hat{U}$ . A similar effect might also be achieved by dipole kicks resulting from orbit distortions in the modulated quadrupoles, but this simple explanation can be excluded as follows.

When the tune modulation is switched on, the filling pattern of the electron beam is clearly reflected in the HERA-B interaction rates – the larger the bunch charge of the electron bunch, the larger the interaction rate at the corresponding proton bunch, Figure 9.3. The non-colliding “pilot-bunches” at the end of each 60 bunch train practically do not contribute to the interaction rate. Without tune modulation the dependency of the interaction rate on the bunch current of the corresponding electron bunch is much weaker. For example, the interaction rate of the non-colliding pilot bunches is only about a factor of two smaller than the average interaction rate of colliding bunches. This is a clear indication that the observed effect is indeed dominated by the beam-beam interaction in combination with tune modulation, and not just an orbit effect due to dipole fields caused by orbit distortions in the modulated quadrupoles.

### 9.3 Conclusion

In contrast to previous measurements in 1999 [20], no frequency dependence of the HERA-B interaction rate stability could be detected during the HERA machine

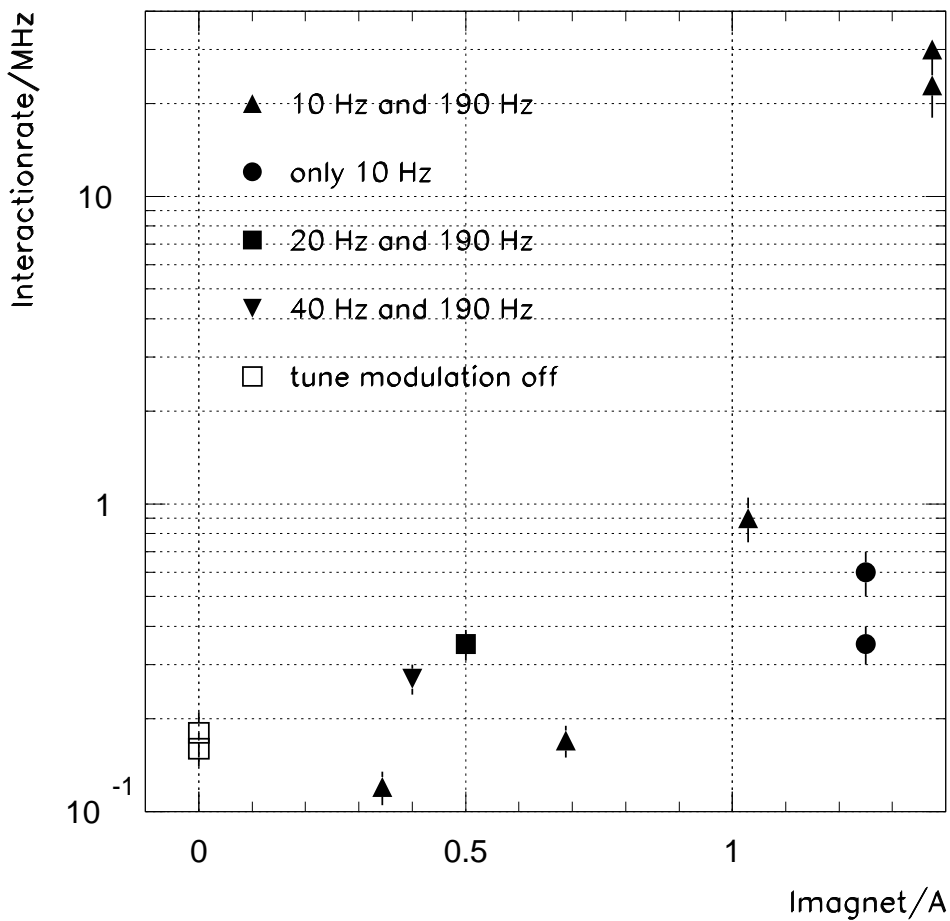


**Figure 9.1:** Interaction rates with fixed wire for different tune modulation parameters [20]. For each setting, the input signal voltages for each frequency component are identical, but their sum might be varied. Due to the strong frequency dependency of the magnet power supply output current, the resulting total tune modulation amplitude is different for different frequency parameter sets.

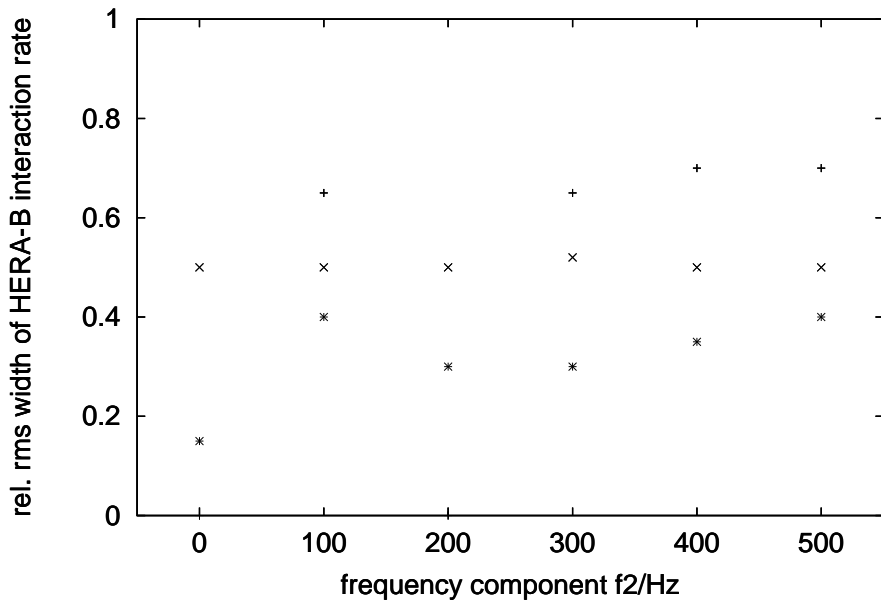


**Figure 9.2:** Interaction rate stability for different tune modulation frequencies  $f_2$  and three different amplitudes  $\hat{U}$  (+ : 0.5 V,  $\times$  : 1.0 V, \* : 2.0 V). The lower frequency component was always set to  $f_1 = 12 \text{ Hz}$ . The case without a higher frequency component is shown as  $f_2 = 0 \text{ Hz}$  here, and in order to have comparable conditions the amplitude was set to  $\hat{U}/2$ .

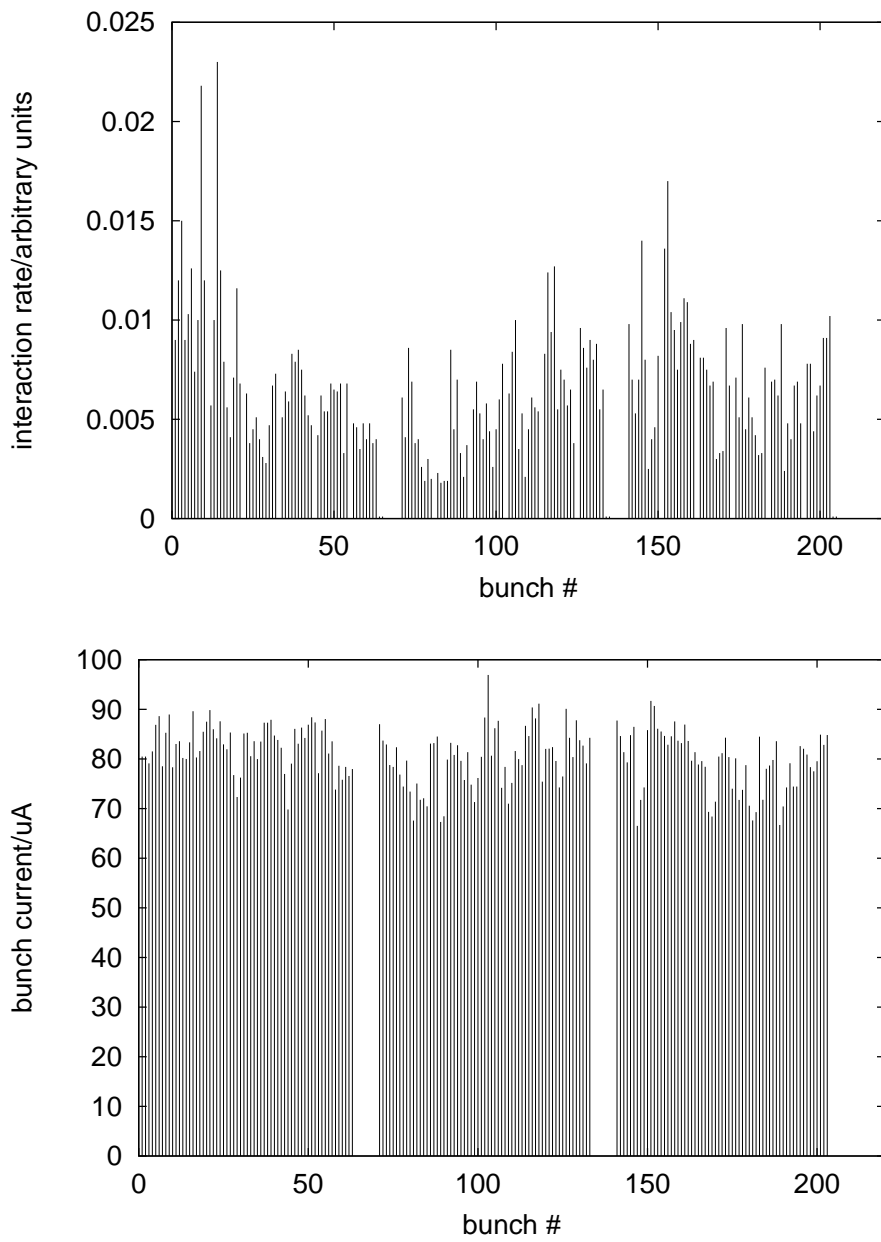


**Figure 9.3:** HERA–B interaction rates per bunch (top) and bunch currents of the corresponding electron bunches. Note that the last two proton bunches (“pilot bunches”) in each 60 bunch train that have no counterpart in the electron beam practically do not contribute to the interaction rate.

study period in August/September 2000. This has to be investigated after the luminosity upgrade shutdown. Nevertheless, tune modulation clearly improves the interaction rate stability at the HERA-B wire target.

## 9.4 Acknowledgments

We would like to thank M. Lomperski and M. Schmitz for assistance with the measurements.

# 10 Measurement Setup for Bunched Beam Echoes in the HERA Proton Storage Ring

by E. Vogel, W. Kriens, and U. Hurdelbrink, DESY Hamburg

Date: 2000, Sep. 2, 1pm to Sep. 2, 9pm, Logbook XLV, p. 73–74

Echo experiments are one of the most powerful tools for determination of diffuse processes in many body systems. Within the scope of beam dynamics experiments for examination of the longitudinal behavior of the bunched HERA proton beam, we started to establish beam echo measurements. These first required some tests on the RF system to provide sufficiently short and powerful RF kicks. For the detection of the beam response we used the real time single shot bunch phase and length measurement [22] with a modified timing scheme. From these measurements we were able to determine the values for the Landau damping times at 40 GeV and at 920 GeV in HERA for the first time. Furthermore the measured data showed a clear relation between the elapsed time from the dipole to the quadrupole kick and the echo strength. So far measurements with well controlled RF noise have not resulted in a uniform response of the echo amplitude.

## 10.1 Introduction

Normally, in microscopic many body systems of identical particles, one cannot stimulate and measure an individual particle. On the contrary one always stimulates and measures an ensemble. Provided the behavior of the particles are slightly different, because of varying surroundings, the response of the ensemble is influenced by this difference. The measurement of the ensemble compared to the measurement of a single particle can differ extremely. Echo experiments are methods to eliminate the different behavior of the particles. These techniques exist in plasma physics, have become very sophisticated in solid states physics, and have been recently used in proton accelerator physics [23, 24, 25].

In the case of a proton bunch we have the following situation: A sufficiently short kick on the RF phase e.g. a quarter of the synchrotron oscillation period, causes a phase oscillation. Shortly after the kick all protons oscillate in phase and as a result the bunch center oscillates. The synchrotron frequency of a single proton depends on its maximum oscillation amplitude because of the flatter bucket potential at higher oscillation amplitudes. The larger the maximum amplitude is the lower is the synchrotron frequency. Because of this dependence the kicked protons lose their phase relation after a certain time and the bunch center stops oscillating. This damping of the bunch center oscillation is called Landau damping.

The single proton still oscillates and carries the information about the phase kick. From an RF amplitude kick it is possible to reconstruct a part of the initial

phase dependence of the protons and thus obtain a bunch center oscillation. This is called the echo.

Some of the single protons loose their information about the phase kick by scattering processes. When there is a long time between the phase kick and the amplitude kick, more information is lost. This influences the reconstruction, i.e. the echo will become smaller.

This method only makes sense, if the Landau damping time is smaller than the time constant of the scattering processes. However this is normally true in a proton accelerator.

One can develop bunch shape oscillations in a series of modes. The first mode is a bunch center oscillation called the dipole mode and the second one a bunch length oscillation called the quadrupole mode. Thus we refer to the RF phase kick as a dipole kick, because the dipole mode is excited, and to the RF amplitude kick as a quadrupole kick.

## 10.2 RF Kick Production

At injection energies of the HERA proton storage ring at 40 GeV the RF buckets are mainly built up by the two 52 MHz RF cavities. So it is most effective to produce the necessary RF kicks by modulating the RF of one of the 52 MHz cavities. During acceleration to 920 GeV the RF amplitude of the 208 MHz cavities is increased such that at 920 GeV these systems mainly build up the RF buckets. In this case the RF kicks must therefore be produced by an intervention into the RF system of one 208 MHz cavity.

The technical assembly of both RF systems is different, this requires two different techniques for the RF kick production. To determine the particular solution, some tests and small modifications to the RF system were necessary. These changes were not inside the control loops but rather at connection points between the control system front end computers (FECs) and the analog control loops. We observed no negative influences on normal operation of the storage ring caused by these modifications.

To generate two rectangular signals with programmable amplitude, width, and time separation between them, we used the four channel digital delay / pulse generator from Stanford Research System model DG535. We controlled it via a GBIB connection to a UNIX workstation. This generator also provided a trigger signal to the real time single shot beam diagnostic. Because we are just starting to establish beam echo measurements in HERA the control software for the kick production with the Stanford DG535 and the control software for the single shot beam diagnostic were implemented on two different computer platforms. Thus the recording time of the measurement series was dominated by the time of personal communication.

### 10.2.1 52 MHz RF-System

The 52 MHz RF system provides a feed forward compensation input for an additional RF signal to compensate beam loading. Since HERA started running in 1992, this

input has never been used. In order to enable this signal path, one had to set the corresponding property in the low level control system available in the proton RF control electronic room.

After doing this one can add any RF signal to the RF control signal which drives the final stage amplifier for the cavity. We used two 52 MHz RF bursts produced with an I/Q modulator. For the LO signal we took the 52 MHz RF reference. By supplying the I/Q demodulator at the I input with the first rectangular signal from the Stanford DG535 and the Q input with the second one we produced two RF bursts with a phase relation of  $90^\circ$ . The observation of the cavity voltage by sampling the output signals of an I/Q demodulator indicated the necessary adjustment of the cable length and therewith the phase between RF control signal and the added RF bursts. We chose the cable length so that the first burst produced a dipole kick and the second one a quadrupole kick. For the technical setup see figure 10.1.

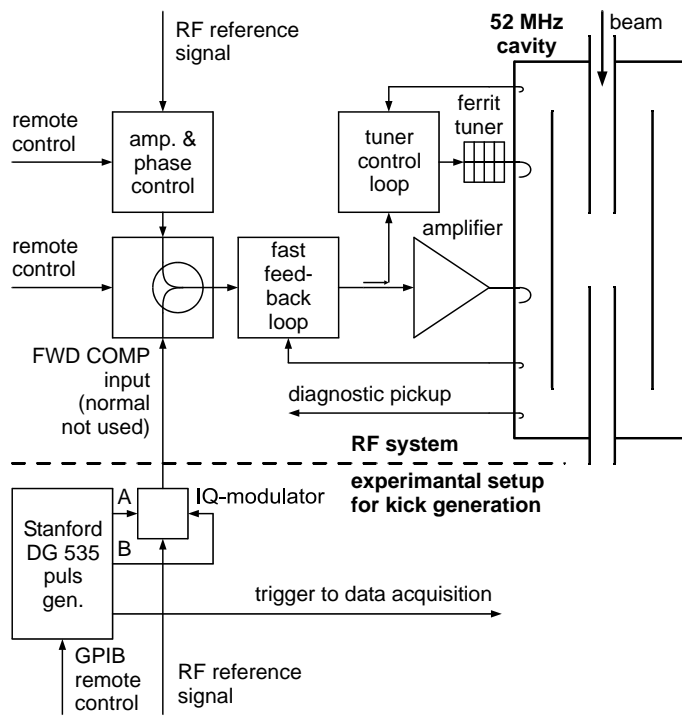


**Figure 10.1:** The 52 MHz RF System for an accelerating cavity and the intervention for the RF kick production.

Amplitude and Phase are set at the 52 MHz RF system via an open loop control. Therefore the kicks produced by using the feed forward compensation input are not suppressed by a control loop.

Figure 10.2 shows the angular pointer of the 52 MHz Cavity No 1 taken by I/Q demodulation of the diagnostic pickup signal. Note that the two RF bursts act relatively cleanly as pure phase and amplitude kicks.

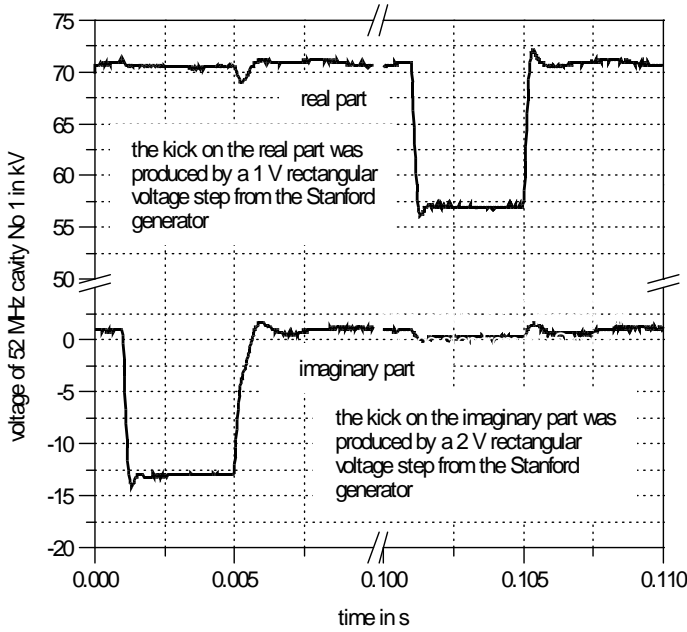


**Figure 10.2:** The I/Q demodulated 52 MHz pickup signal shows a dipole kick followed by an quadrupole kick.

### 10.2.2 208 MHz RF-System

The first idea was to produce the RF kicks at the 208 MHz RF system in the same way as at the 52 MHz system i.e. via the feed forward compensation input, which is not yet used. In contrast to the 52 MHz system an amplitude and phase closed loop control is implemented. It turned out that this control loop has a time constant shorter than the necessary kick duration of about 4 ms. This means that it suppresses kicks produced by adding RF bursts via the feed forward compensation input.

A way out of this dilemma was a change of the set point of the amplitude and phase regulation loop [26], see figure 10.3.

The philosophy for normal operation of the storage ring is to change the RF values only adiabatically. For this reason the input for the phase at the loop was provided with a low pass filter realized with a capacitor. For the kick production we had to remove this capacitor. Under normal conditions the phase value set from the control system for a single 208 MHz cavity is zero during the whole operation. So it was possible to unplug the control system at this point and plug in the Stanford DG535 signal for the dipole kick.

One is able to add an amplitude modulation to the amplitude set point chosen via the control system at the condition unit. This unit followed the same philosophy e.g. only adiabatic changes were used. A capacitor used for low pass filtering was also removed. Finally we were able to supply kicks with sufficient rise times and power see figure 10.4.

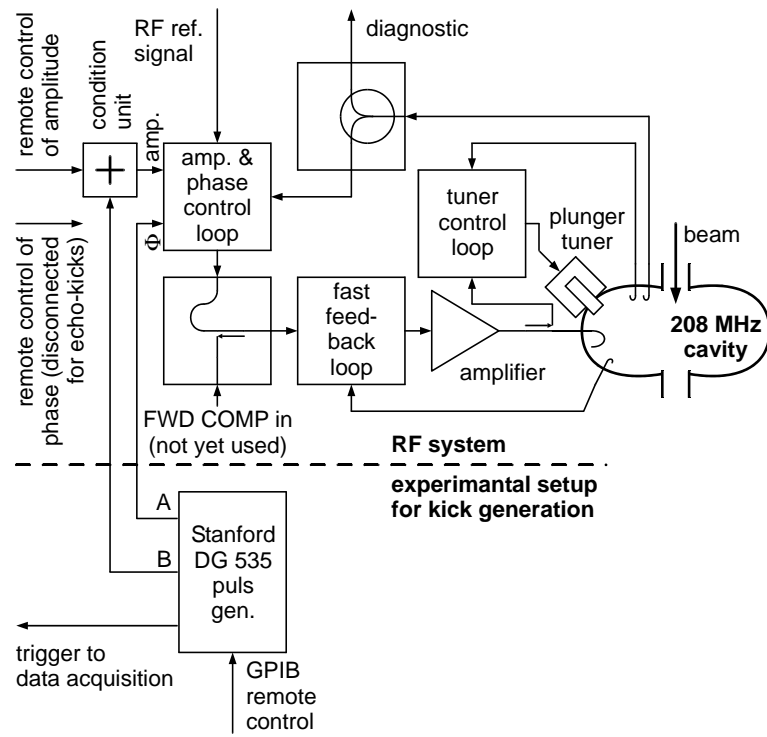


**Figure 10.3:** 208 MHz RF system of one cavity and the setup for the kick production.

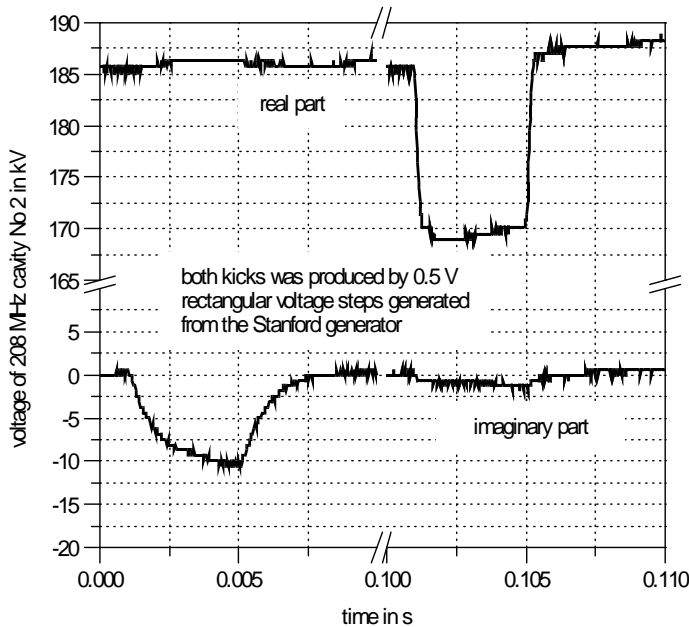


**Figure 10.4:** I/Q demodulated 208 MHz pickup signal with dipole and quadrupole kick.

### 10.3 Measurement of Beam Properties

The reader can find a detailed description of the real time single shot bunch phase and length measurement at HERA in [22]. Here we will only give a sketch of the principles used.

#### 10.3.1 Single Bunch Phase and Length

A bunch passing a resistive gap monitor leads to a broadband RF pulse whose shape is identical with the longitudinal bunch shape. This signal is analyzed by analog signal processing, see figure 10.5.

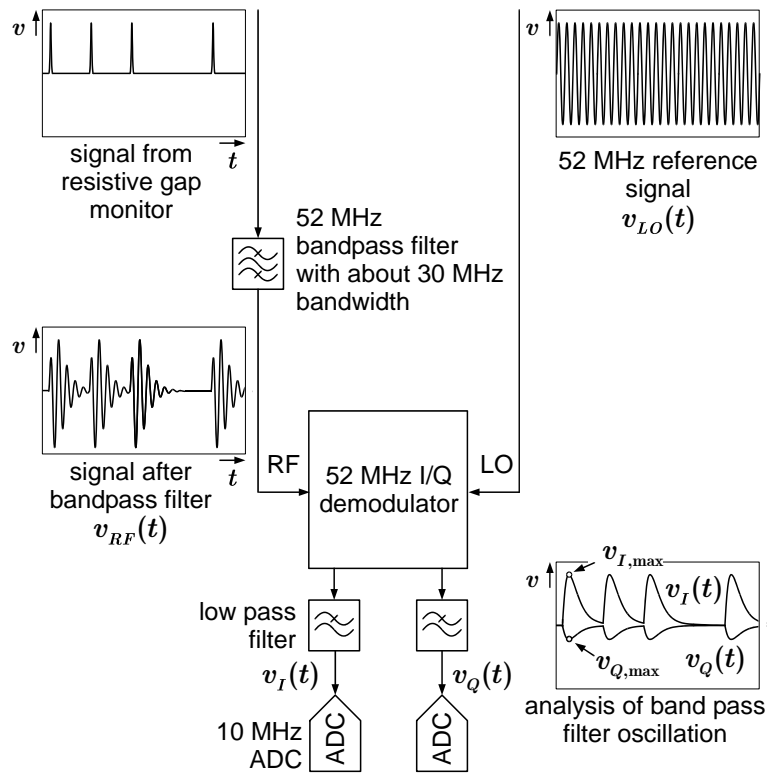


**Figure 10.5:** Principle of bunch phase measurement with a special designed 52 MHz band pass filter.

With this bunch signal one excites an oscillation in a 52 MHz band pass filter, whose properties are chosen so that the oscillation stops when the signal from the next bunch arrives. This oscillation is down converted by an I/Q demodulator to the real and imaginary part from the angular pointer of this oscillation. By sampling these real and imaginary parts at maximum value of the pointer length one gets via the arctangent the bunch phase  $\Delta\phi$  and via the absolute value the 52 MHz bunch

Fourier coefficient  $A_{52}$

$$\Delta\phi = \arctan \frac{v_{Q,\max}}{v_{I,\max}} + \Delta\phi_{cal} \quad (10.1)$$

$$A_{52,meas} \equiv \sqrt{(v_{I,\max})^2 + (v_{Q,\max})^2} \quad (10.2)$$

$$A_{52} = A_{52,cal} A_{52,meas}. \quad (10.3)$$

$\Delta\phi_{cal}$  and  $A_{52,cal}$  are calibration constants.

Assuming a Gaussian bunch shape, one can calculate the bunch length from the Fourier coefficients  $A_1$  and  $A_2$  for two different frequencies  $\omega_1$  and  $\omega_2$  of the longitudinal bunch shape

$$l_{FWHM} = c \cdot 2 \sqrt{\ln 4} \sqrt{\frac{2}{\omega_2^2 - \omega_1^2}} \sqrt{\ln \frac{A_1}{A_2}}. \quad (10.4)$$

The coefficient  $A_1$  of the first frequency 52 MHz is delivered by the assembly of the phase measurement. For the determination of  $A_2$  the direct measurement of the 208 MHz bunch Fourier coefficient with a 208 MHz band pass filter and an RF diode is used, see figure 10.6.

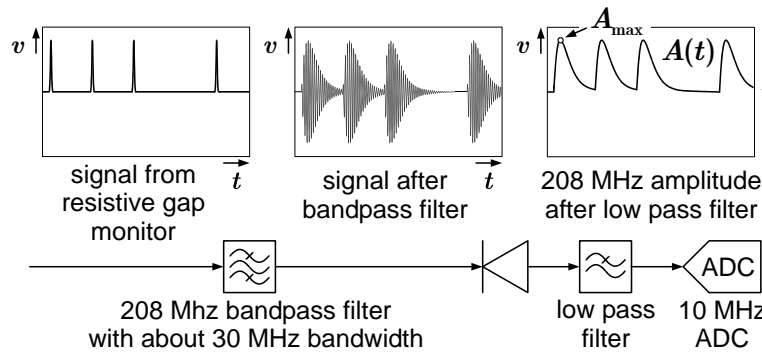


**Figure 10.6:** Principle of 208 MHz bunch Fourier coefficient measurement for calculating back the bunch length.

### 10.3.2 Timing

In contrast to the measurement of multi-bunch oscillations in [22] we here measured only one bunch. This leads to a good flexibility at the observation times because of the relatively high amount of ADC memory available. For example we were able to observe the synchrotron oscillations of the bunch over a time of about 72 s without any gap. By reducing the observation time we can increase the time resolution.

To measure the bunch phase and length at a certain time, we first sampled the signals in the dump gap and directly afterwards we measured for the first bunch the signals from the phase and the 208 MHz Fourier coefficient. By doing this we were able to carry out signal offset corrections for all offset errors taking place at longer

time scales than the time between the measurement in the dump gap and the first bunch, i.e. longer than about  $1\ \mu\text{s}$ .

Performing such bunch phase and length measurements every 13th turn yielded a sample frequency of 3.64 kHz. This was sufficiently high to observe typical synchrotron oscillations with frequencies of 20 Hz to 40 Hz and bunch length oscillations with frequencies of 40 Hz to 80 Hz. In addition this high sample frequency provides good conditions for digital filters.

### 10.3.3 Errors of Measured Signals

For an estimation of the errors we took data from measurements of the bunch phase and bunch length of a quiet bunch. By plotting the number of measurements with a certain deviation from the average over the deviation, one gets the distribution function of the error of single shot measurements. One can reduce the measurement error by low pass filtering. In figure 10.7 the error distribution before and after filtering of bunch phase data is shown.

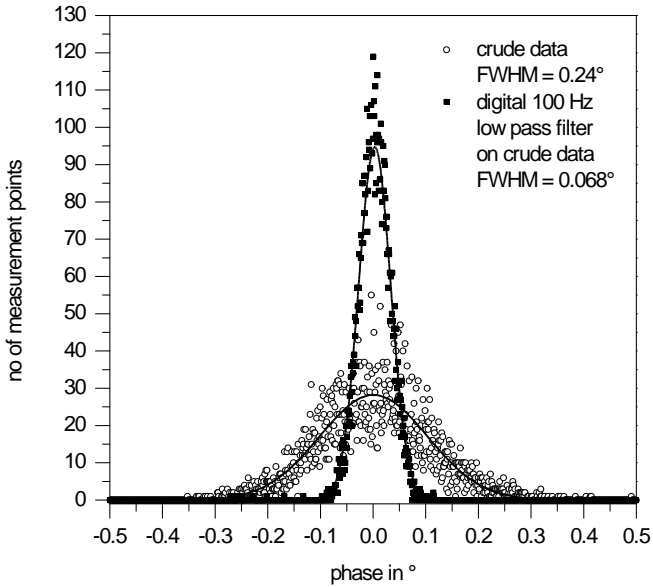


**Figure 10.7:** Error distribution of bunch phase measurement.

In figure 10.8 one can see the error distribution of the bunch length measurement from the crude data and after filtering.

## 10.4 Observed Beam Echoes

In figure 10.9 and 10.10 typical beam echo signals in the HERA proton storage ring at 920 GeV are shown.

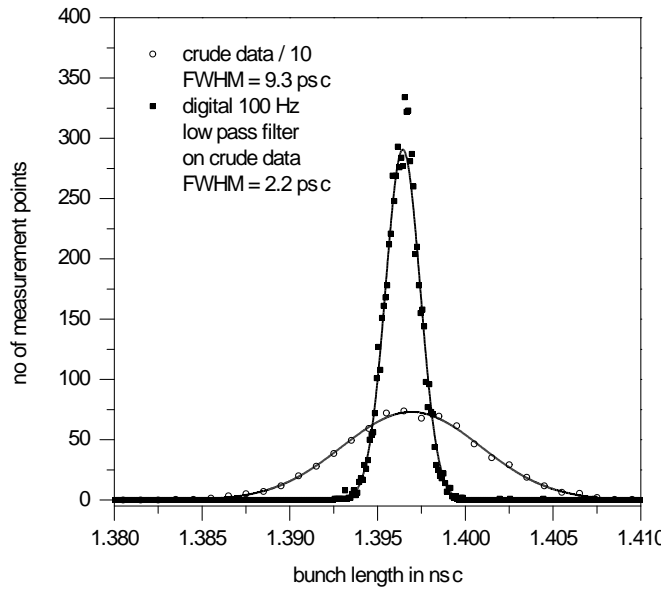


**Figure 10.8:** Error distribution of bunch length measurement.

Both kicks were 4 ms long. The dipole kick strength was about 40 kV and the quadrupole kick about 65 kV. With a sum voltage of approximately 600 kV one obtains the kick angle for the dipole kick

$$\Delta\phi_{\text{kick}} = \arctan \frac{40 \text{ kV}}{600 \text{ kV}} = 3.8^\circ . \quad (10.5)$$

This means with a phase kick of  $3.8^\circ$  over a time period of a quarter synchrotron oscillation cycle, we get a maximum amplitude of the synchrotron oscillation of about  $3.8^\circ/4 = 0.95^\circ$ . This agrees well with the measured values, see figures 10.9 and 10.11. In the measurement shown the dipole kick was applied 1 s after the trigger started the measurement and the quadrupole kick at 1.8 s so that one can observe the echo at the time  $1 \text{ s} + 2 \times 0.8 \text{ s} = 2.6 \text{ s}$ . Filtering the data with a 100 Hz low pass filter delivers much clearer conditions for further data analysis.

Figures 10.11 and 10.12 show a zoomed view of the beam response.

Both kicks act very clean. This means, that the dipole kick only excited dipole oscillations, there is no oscillation signal of the bunch length. The quadrupole kick only excites a quadrupole oscillation and no dipole oscillation.

In figure 10.10 you can see a light bunch lengthening at the time of the dipole kick. This is caused by the onset of the filamentation process.

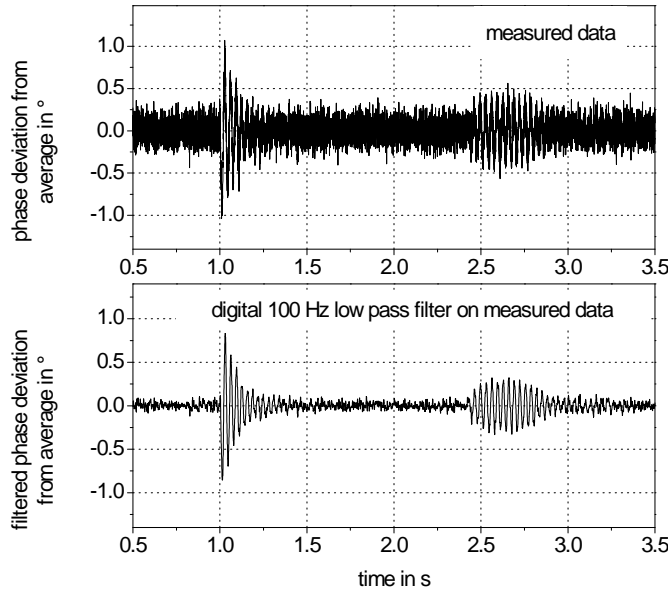


**Figure 10.9:** Bunch phase oscillation during a beam echo measurement.

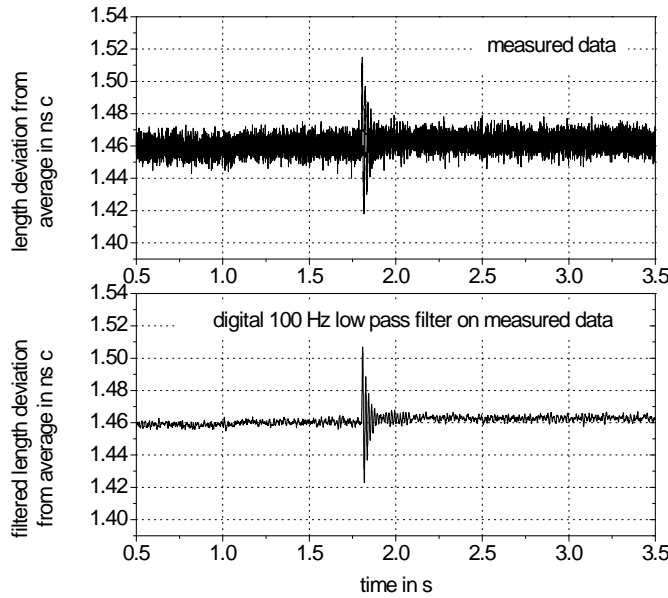


**Figure 10.10:** Bunch length oscillation during a beam echo measurement.

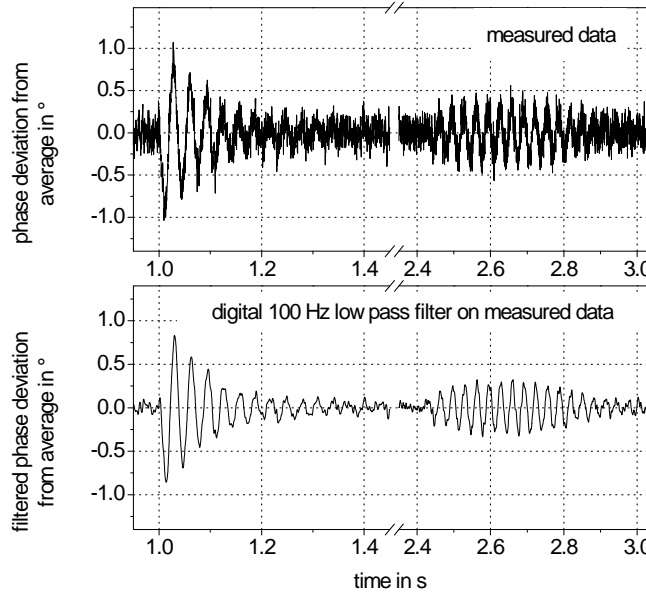


**Figure 10.11:** Zoomed view of bunch phase oscillation during a beam echo measurement.

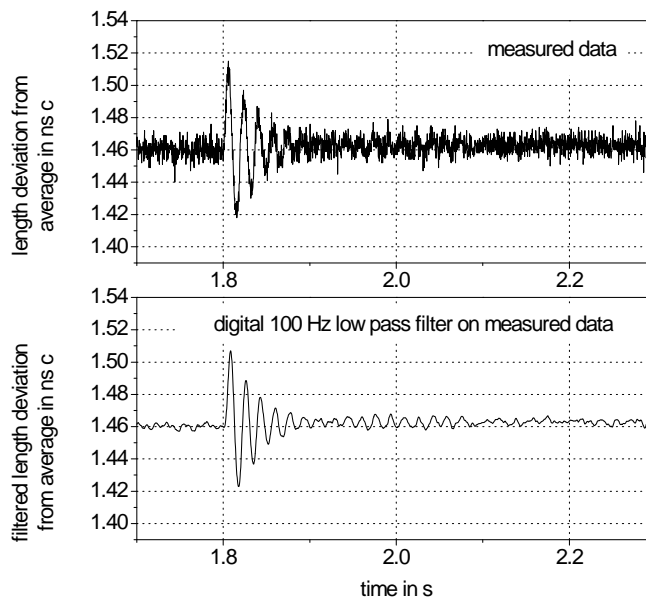


**Figure 10.12:** Zoomed view of bunch length oscillation during a beam echo measurement.

## 10.5 First Analysis

The measurements presented here are the first beam echo measurements made in the HERA proton storage ring. Therefore the final goal of these studies was to prove that we have all relevant technical details under control for future beam echo studies. During previous studies many parameters which are important for an accurate data analysis were not controlled. For example we had no exact measurement of the cavity voltages etc. Here are many possibilities for further improvement. It will be interesting to see the results of these improvements when the luminosity upgrade is finished and the HERA proton storage ring is in operation again.

### 10.5.1 Landau Damping

An important effect for the longitudinal stability of a proton storage ring is Landau damping. The value of the landau damping time is supplied in passing by the echo experiments. By fitting

$$\Delta\phi = e^{-t/\tau_{\text{Landau}}} \sin(\omega_{\text{synchrotron}} t) \quad (10.6)$$

to the beam phase oscillation response to the dipole kicks one obtains the damping time  $\tau_{\text{Landau}}$ , which we used here to quantify the Landau damping. This formula is not exact but is used to simplify the first data analysis.

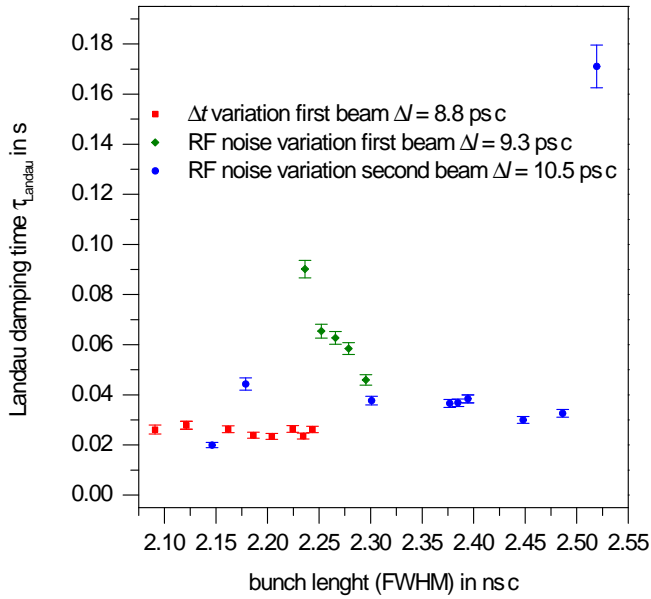


**Figure 10.13:** Zoomed view of bunch phase oscillation during a beam echo measurement.

Figure 10.13 shows Landau damping values at 40 GeV determined from different series of beam echo measurements. At this energy we deal with a very nonlinear

bucket because both RF systems are switched on. The 52 MHz system builds up the bucket and at the 208 MHz system three of the four cavities are in phase and one runs with a phase shift of  $180^\circ$  and compensates most of the voltage of these three cavities. The remaining 208 MHz voltage leads to a strong non-linearity in the bucket. The more nonlinear a buckets is, the bigger is the Landau damping.

At 920 GeV the buckets are built up from three in-phase 208 MHz cavities and the 52 MHz cavities contain less voltage than at 40 GeV. The result is a more linear bucket and one observes less Landau damping, see figure 10.14.

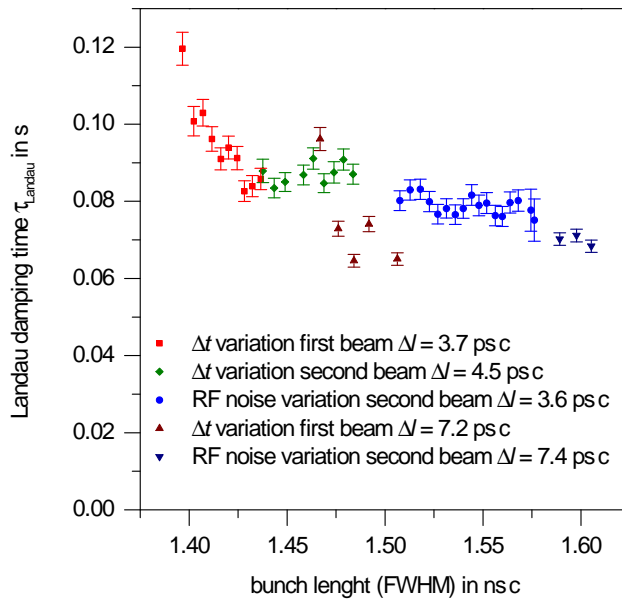


**Figure 10.14:** Landau damping time at 920 GeV.

One would expect a dependence of the Landau damping time on the bunch length. The longer a bunch is, the more nonlinear is the behavior. This means that the bigger the oscillation amplitude of a single proton is, the lower is its synchrotron frequency. A bigger spread of synchrotron frequencies inside a bunch leads to more Landau damping. At 920 GeV one can see a dependence of the damping time on the bunch length, see figure 10.13. Why this is not the case at 40 GeV is not yet clear. Perhaps the special bucket shape plays a role.

### 10.5.2 Echo Strength over $\Delta t$

The main motivation to set up beam echo measurements was to measure the dependence of the beam echo strength on the time deviation between the dipole and quadrupole kick  $\Delta t = T_{\text{quadrupole}} - T_{\text{dipole}}$ . We hope to learn more about diffusive processes from the measured curve, such as intra-bunch scattering, processes caused by RF noise etc.

Unfortunately the shape of the echo amplitude is very sensitive to the quadrupole kick strength [24, figure 16]. Thus the maximum amplitude of the echo per maximum amplitude of the initial dipole oscillation is not a very good indicator for the echo strength. The integral over the echo amplitude seems to depend less on the quadrupole kick strength [24, figure 16]. For data analysis we used the ratio of the integrals over the absolute value of the oscillations instead. This means that for the dipole kick response we took the value

$$\Sigma_{\text{dipole}} = \int_{T_{\text{dipole}}}^{T_{\text{quadrupole}}} |\Delta\phi(t)| dt \quad (10.7)$$

and for the echo strength the value

$$\Sigma_{\text{echo}} = \int_{T_{\text{quadrupole}}}^{T_{\text{quadrupole}} + 2 \Delta t} |\Delta\phi(t)| dt. \quad (10.8)$$

We first subtracted the noise

$$\frac{\Sigma_{\text{noise}}}{s} = \frac{\int_{T_0}^{T_{\text{dipole}}} |\Delta\phi(t)| dt}{T_{\text{dipole}} - T_0} \quad (10.9)$$

from the strength of the dipole kick

$$\Sigma_{\text{dipole,corr}} = \Sigma_{\text{dipole}} - (T_{\text{quadrupole}} - T_{\text{dipole}}) \frac{\Sigma_{\text{noise}}}{s} \quad (10.10)$$

and the echo

$$\Sigma_{\text{echo,corr}} = \Sigma_{\text{echo}} - 2 \Delta t \frac{\Sigma_{\text{noise}}}{s} \quad (10.11)$$

before calculating the ratio between direct response and echo

$$\frac{\Sigma_{\text{echo,corr}}}{\Sigma_{\text{dipole,corr}}}. \quad (10.12)$$

The fluctuation of the noise amplitude is equivalent to the uncertainty of the calculated kick strength.

Figure 10.15 shows the echo strength divided by the dipole kick strength versus the time deviation between the two RF kicks at 40 GeV.

At 920 GeV we took three measurement series with different parameters and got the result shown in figure 10.16.

As previously mentioned, the dipole kick always causes bunch lengthening. While the filamentation process depends on the bunch length it depends also on the bunch lengthening. Therefore the averaged value of the lengthening per dipole kick for each measurement series is indicated.

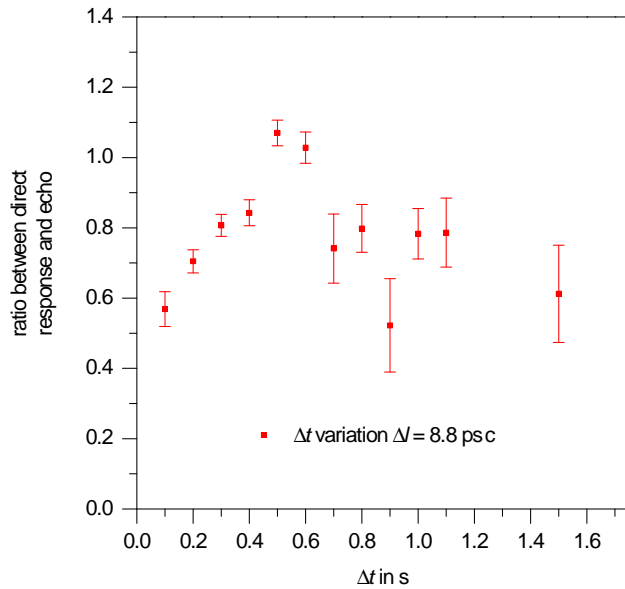


**Figure 10.15:** Echo strength as a function of the time delay between the two RF kicks at 40 GeV.

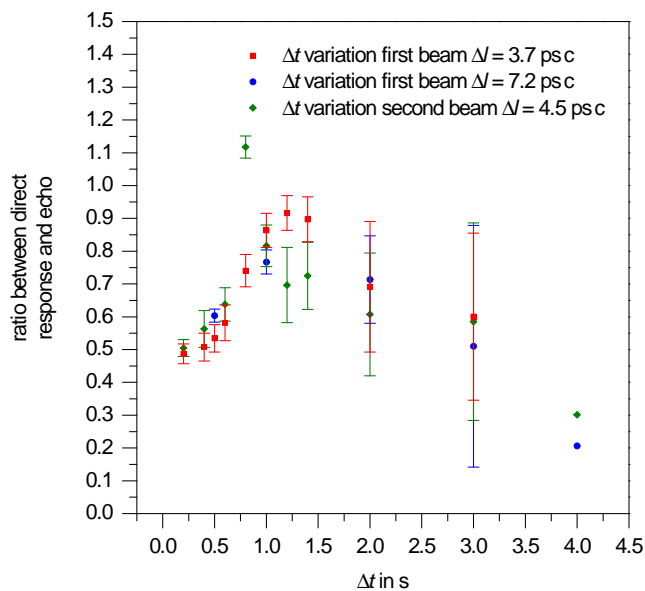


**Figure 10.16:** Echo strength over the time delay between the two RF kicks at 920 GeV.

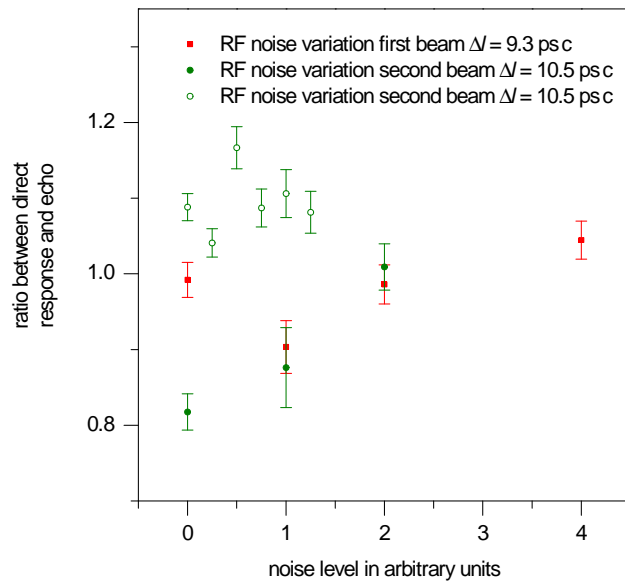
### 10.5.3 Echo Strength over RF Noise

In view of the coasting beam problems at the experiment HERA-B, the question came up whether RF noise could cause coasting beam.

In principle one can analyze the influence of RF noise on the bunched beam by observing the ratio of coasting beam current to bunched beam current over long time periods during an application of RF noise to a random modulation of the set points of the RF systems. Such measurements take a lot of time. If one could observe the effect of RF noise on the echo strength, beam echo measurements could be used as a complementary examination method which would be much faster.

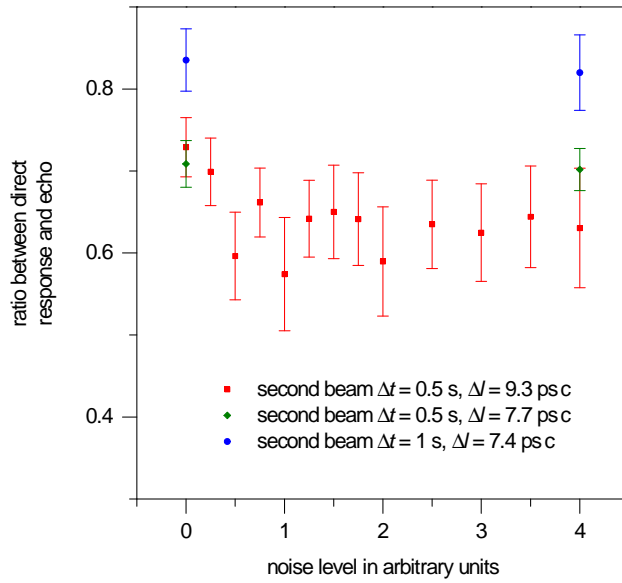
We checked whether we can observe a change of the echo strength with constant time deviation between the kicks as a function of RF noise. One would expect smaller echo strength at higher RF noise levels. Higher RF noise causes more protons in a bunch to lose information about the initial dipole kick through scattering processes, and therefore the echo will be smaller.

Figure 10.17 shows the echo strength over RF noise at 40 GeV and figure 10.18 the situation at 920 GeV.



**Figure 10.17:** Echo strength over RF noise at 40 GeV.

Both figures show a constant behavior i.e. we observed no influence. This could be due to the relatively short time delay between the kicks in combination with the relatively low noise levels. In future one should try to increase the time delay between the kicks until one can measure no longer echoes.



**Figure 10.18:** Echo strength over RF noise at 920 GeV.

## 10.6 Conclusion

We have shown that we have longitudinal bunched beam echo experiments at the HERA proton storage ring under control. The signal quality received is rather good and indicates that good measurement results could be reached by a further development of these experiments.

We measured at 40 GeV and at 920 GeV. In both cases the Landau damping times were obtained. When we changed the time delay between the RF kicks we have seen a noticeable dependence of the echo strength on this time delay. By using an automated measurement setup one could expect good enough results to compare them with theory. The dependence on RF noise resulted in a non uniform picture. Here we should increase the time deviations between the kicks and repeat the measurements.

## Acknowledgments

We would like to thank Richard Wagner and Jozef Baran from the proton RF group for their support by modifying the RF control loops, as well as Hong Gong Wu from the machine software group for adding the needed special features to the ADC server software.

# 11 Measurement of Multi Bunch Oscillations at Different Fill Patterns of the HERA Proton Storage Ring

by Elmar Vogel, DESY Hamburg

Date: 2000, Jun. 8, 3am to Jun. 8, 6am,

Date: 2000, Sep. 2, 8am to Sep. 2, 1pm, Logbook XLI, p. 73–74

If one classifies longitudinal multi bunch oscillations in storage rings, one gets as many oscillation modes as RF bucket positions are occupied. Just by symmetric considerations one would expect a change of the appearing multi bunch oscillations by leaving bucket positions unoccupied [27].

Furthermore in the HERA proton storage ring the delay times of the RF fast feedback loops are in the range of 200 ns and 250 ns. With a time delay of 96 ns between the bunches, this means that the signal which corrects the beam loading transient of a bunch is applied to the second subsequent bunch. This should cause a next to nearest neighbor action. By leaving for example two or more bucket positions after a bunch unoccupied one would expect a big difference for the resulting multi bunch oscillations.

## 11.1 Supplying Different Fill Patterns

Unconventional fill patterns in the HERA proton storage ring must be prepared by special operations of the pre accelerators. The proton accelerator complex at DESY is shown in figure 11.1.

Under normal conditions the DESY III synchrotron accelerates 11 bunches from 50 MeV to 6.6 GeV, from these, 10 bunches are transferred to the PETRA proton storage ring. For the here described studies single bunch transfer from the DESY III to PETRA was used for the arrangement of the needed fill patterns in PETRA. For doing that one had to shift the hole timing from PETRA by hand after each single bunch transfer from DESY. This was only possible by switching off the PETRA auto pilot which is used during standard operation. Since the proton beam lifetime in PETRA at injection energies is about a few minutes, it was necessary to train the procedure to create the fill patterns sufficiently quickly. After acceleration of the special fill patterns in PETRA from 6.6 GeV to 40 GeV they were transferred to the HERA proton storage ring by using the standard transfer technique.

We were able to create HERA fill patterns consisting of 18 and 9 proton bunches in this way.

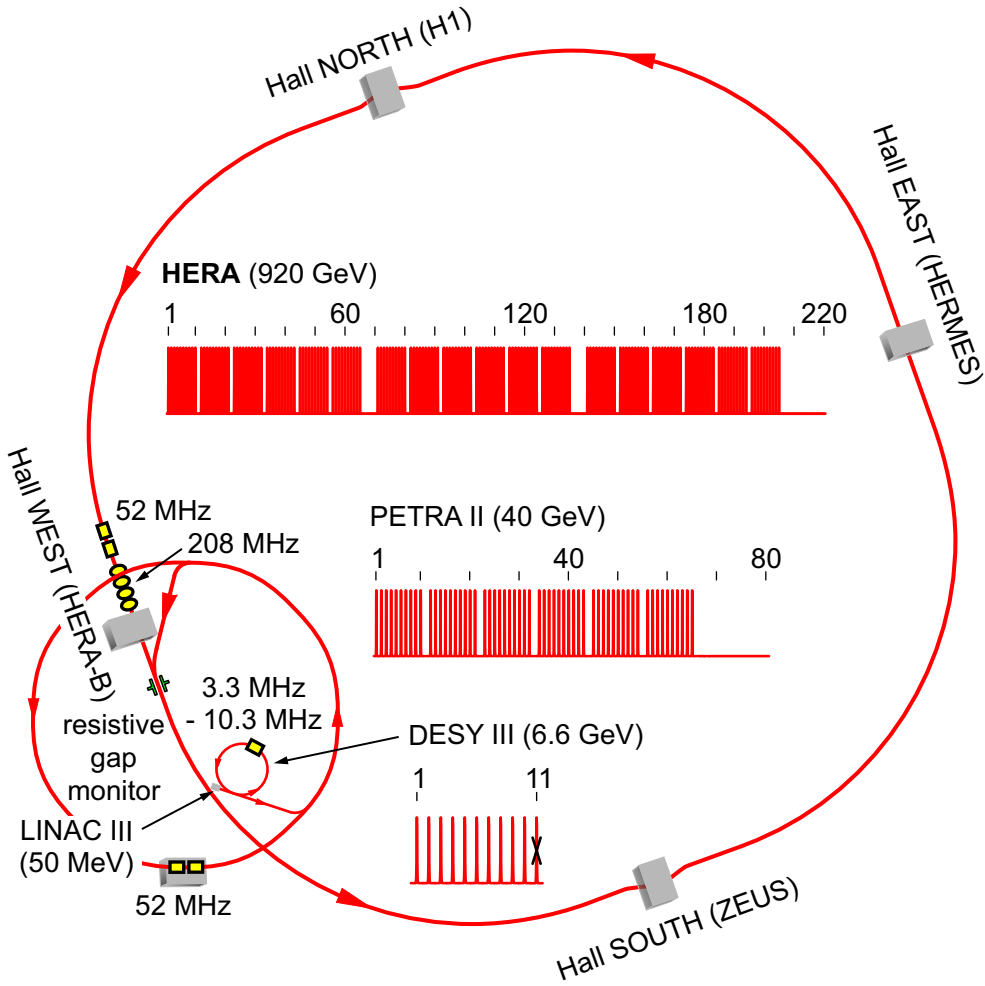


**Figure 11.1:** The proton accelerator complex at DESY with the occupied positions for bunches during standard operation.

## 11.2 Performed Measurement

With the newly installed fast longitudinal beam diagnostic in the HERA proton storage ring [22] one can record the bunch phase and length of all bunches simultaneously. During ramping from 40 GeV to 920 GeV one always observes multi-bunch oscillations. An evaluation of the multi bunch situation is made possible with the new diagnostic by a colored pixel plot. The two axes are the bucket positions and time. The phase deviation from the average bunch phase gives the pixel color in figure 11.2. For bunch length oscillations a similar display exist.

We started with performing multi bunch measurements at different fill patterns of the storage ring shown in figure 11.3.

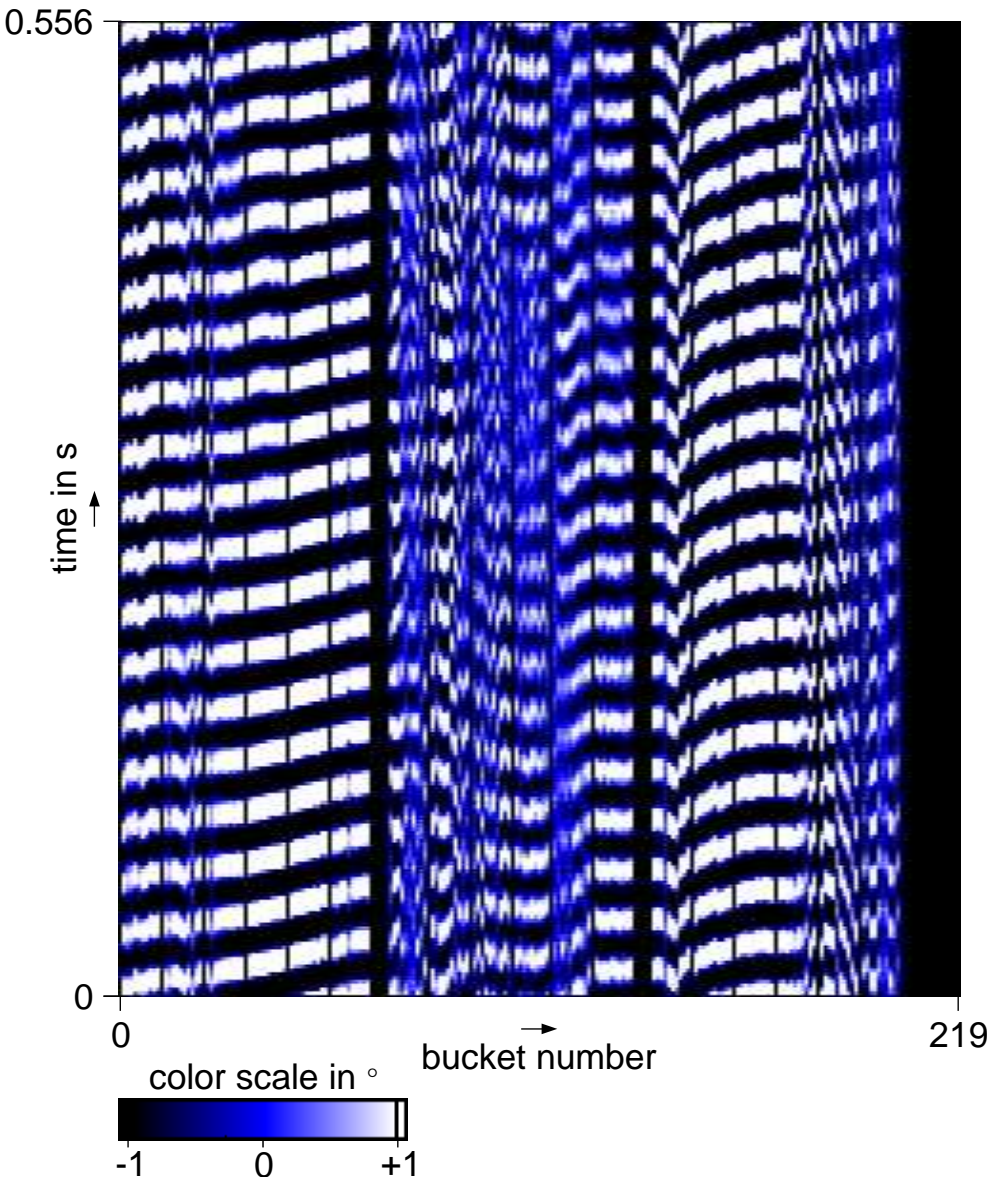


**Figure 11.2:** Multi bunch oscillation of 180 bunches in the HERA proton storage ring.

### 11.3 Results

One would expect a reduction of multi bunch oscillations during the acceleration from 40 GeV to 920 GeV in fillings consisting of 18 or 9 bunches as compared to fillings consisting out of 180 bunches. For the small number of bunches, the bunch length should be observably reduced at 920 GeV. The first view on the data showed neither a significant reduction of the oscillation amplitudes nor a significant reduction of the bunch length. A careful data analysis is necessary.

Determination of other fill patterns than those with 18 and 9 bunches, e.g. 90 bunches, requires initially the development of hard and software for creating these patterns by single bunch transfers from DESY to PETRA automatically.

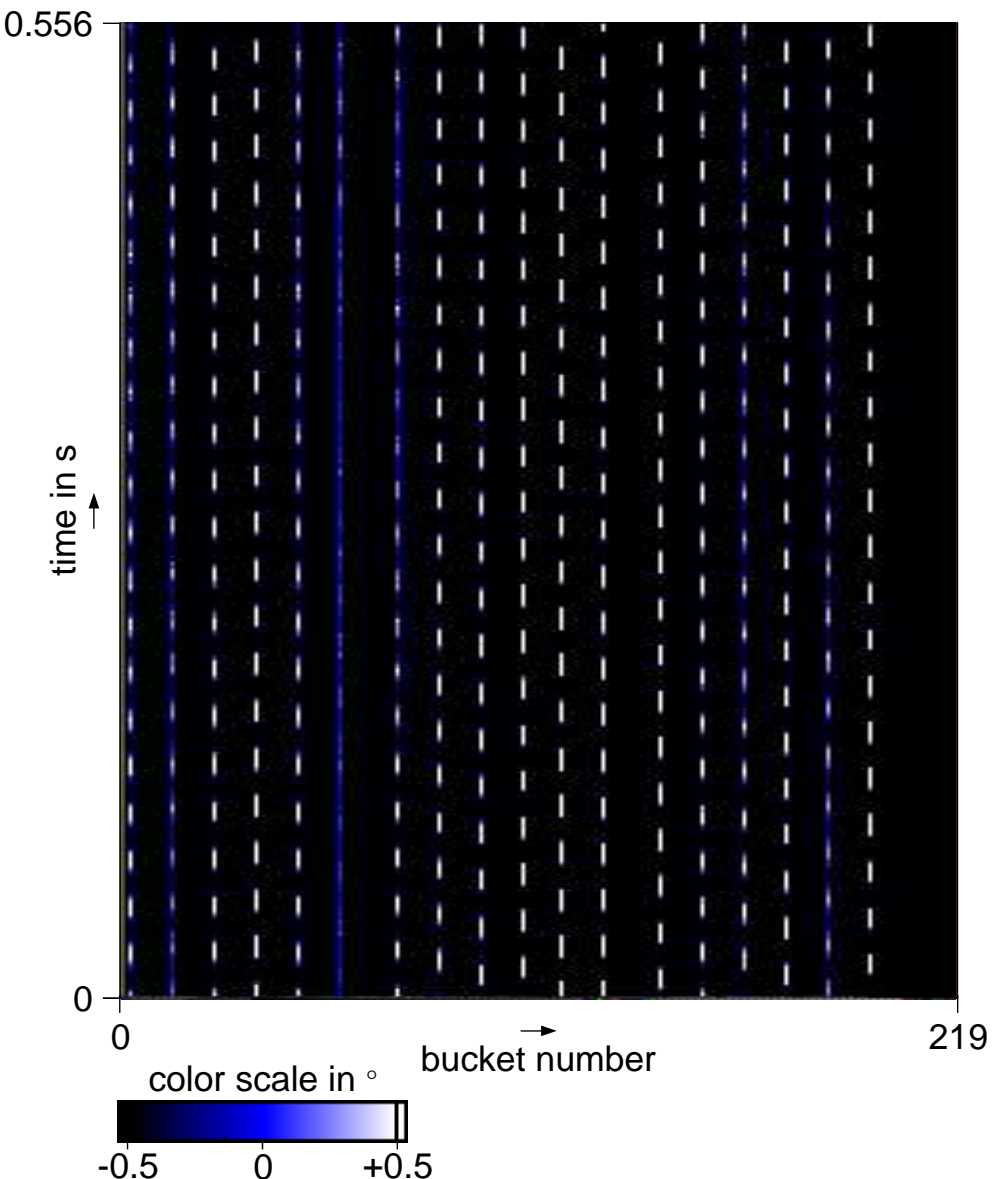


**Figure 11.3:** Multi bunch oscillation of 18 bunches in the HERA proton storage ring.

### Acknowledgments

I would like thank W. Kriens as well as the shift crew for supplying the unconventional fill patterns by the special operation of the pre accelerators DESY and PETRA.

## 12 Measurement of Dynamic Aperture and Resonant Terms at HERA-p at Injection Energy

by W. Fischer, BNL, F. Schmidt, R. Tomás, CERN,  
S. Herb, M. Werner, DESY Hamburg

Date: 2000, Sep. 1, 11pm to Sep. 2, 7am, Logbook XLV, p. 68–71

Date: 2000, Sep. 2, 11pm to Sep. 3, 7am, Logbook XLV, p. 72–73

Date: 2000, Sep. 3, 11pm to Sep. 4, 7am, Logbook XLV, p. 74–75

The single particle dynamics in circular accelerators is dominated by resonances which are driven by nonlinearities due to magnet imperfections or needed for correction systems. A good control of these resonances is essential for optimal machine performance. Recently it has been demonstrated that FFT spectra of turn-by-turn pick-up data can be used to measure resonance driving terms. Controlled experiments are needed to demonstrate the usefulness of these techniques. The HERA proton ring is particularly interesting for these studies since its performance at injection is limited by field errors due to large persistent currents of the superconducting dipoles and quadrupoles.

### 12.1 Introduction

The following method for the determination of the resonance driving terms is based on the Fourier analysis of time series of pick-up data and the Normal Form theory. From the time series of two consecutive pick-ups the linearly normalized Courant-Snyder variables [28] ( $\hat{x}, \hat{p}_x$ ) are obtained. If the motion is regular, we get after N turns:

$$\hat{x}(N) - i\hat{p}_x(N) = \sum_{j=1}^{\infty} a_j e^{i[2\pi(m_j \nu_x + n_j \nu_y)N + \psi_j]} \quad m_j, n_j \in \mathbf{Z} \quad (12.1)$$

Where  $\nu_x$  and  $\nu_y$  are the tunes and the  $a_j$  and  $\psi_j$  are the measurable amplitude and phase of the corresponding spectral line. In [29] the expression of equation (12.1) is obtained using Normal Form theory to first order,

$$\begin{aligned} \hat{x}(N) - i\hat{p}_x(N) &= \sqrt{2I_x} e^{-i(2\pi\nu_x N + \psi_{x0})} - \\ &2i \sum_{jklm} j f_{jklm} (2I_x)^{\frac{j+k-1}{2}} (2I_y)^{\frac{l+m}{2}} e^{i[(1-j+k)(2\pi\nu_x N + \psi_{x0}) + (l-m)(2\pi\nu_y N + \psi_{y0})]}, \end{aligned} \quad (12.2)$$

where  $I_x$  and  $I_y$  are the horizontal and vertical invariants. The  $f_{jklm}$  factors are the so called generating function coefficients. These are related to the resonance driving terms by

$$f_{jklm} = \frac{h_{jklm}}{1 - e^{i\{2\pi[(j-k)\nu_x + (l-m)\nu_y]\}}} . \quad (12.3)$$

The  $a_j$  and  $\psi_j$  are related to the corresponding driving terms by comparing the equations (12.1) and (12.2) and using equation (12.3). In reference [29] it is shown how to determine resonance driving terms in an approximate order by order procedure.

The first goal of the experiment was to check the theoretical model of HERA-p by measuring the  $\beta$ -functions at different locations of interest. The non-linear part of this model is tested with a measurement of the amplitude dependent detuning, in fact the sextupoles configuration in the simulation model has been adjusted such that the theoretical detuning agreed with that found in the experiment. The resonance driving terms were measured according to the above theory using pick-up data from different kick amplitudes and compared with predictions of the tracking model. It was the main goal of the experiment to measure the dynamic aperture and compare it with the stability border as found by tracking simulations with SixTrack [30].

### 12.1.1 Participants in the experiment

The experiment and its analysis has been performed by the following participants:

- Preparation of the instruments:  
S. Herb, M. Lomperski, M. Wendt, M. Werner and K. Wittenburg, DESY.
- Experimenters:  
M. Bieler, S. Herb, F. Maschewski, B. Pawlowski, J. Rothenburg, M. Werner, P. Wesolowski and F. Wohlenberg, DESY, F. Schmidt, R. Tomás, CERN.
- Tracking model and simulation:  
G. H. Hoffstaetter, DESY, W. Fischer, BNL, F. Schmidt, CERN.
- Analysis:  
R. Tomás, CERN.

## 12.2 HERA-p Experiment

In table 12.1 the beam parameters during the experiment are listed. Before starting the experiment we measured the tune ripple spectrum due to power supplies. An upper limit of the total tune ripple was found to be some  $10^{-4}$  (absolute value). The limited accuracy of the measurement did not allow to identify individual spectrum lines with smaller amplitudes. The accuracy of these measurements could have been significantly improved by applying the phased looked loop signal of the tune measurement to the beam excitation kickers.

**Table 12.1:** Beam parameters for the experiment at the HERA proton ring.

Energy E[GeV]	40
$1\sigma$ norm. emittance (after scraping) $\epsilon_n$ [ $\mu\text{m}$ ]	$\approx 1.2$ hor. and ver.
Number of bunches	10
Intensity I [mA]	$\approx 5$
Closed orbit rms [mm]	$\leq 2$
Fractional Horizontal tune $Q_x$	0.292
Fractional Vertical tune $Q_y$	0.297
Chromaticity	$\leq 1$ hor. and ver.

Apart from the  $\beta$ -beating measurements that will be explained in the next section, a standard procedure was followed throughout the experiment: After injection the tunes are placed at the desired values. The coupling lines and the width of the tune peaks in the spectra are minimized. A pencil beam was created by scraping the total intensity down to 1 mA. Particles were placed at larger betatron amplitudes by applying a horizontal kick with the injection kicker. The transverse distributions before and after the kick were measured with wire scanners. 1024 turns of selected BPMs were saved for later analysis and the beam was dumped for a new injection.

In figure 12.1 the horizontal and the vertical wire scans before and after a horizontal kick of  $5\sigma$  are shown. Since the tunes were close, coupling caused excitation in the vertical plane although the kick is only horizontal. This fact also explains why the beam profile evolves to another Gaussian distribution instead of to the expected double peak structure in the horizontal plane. The experiment was limited by the physical aperture, which we tried to increase by local bumps but we lacked the necessary time for optimizing it sufficiently, in fact in 1994 experiment a full 8 hour shift had been dedicated for this purpose.

It was decided to separate further the horizontal and vertical tunes to reduce the coupling. The new working point selected was (0.28, 0.31) which has been chosen for the LHC at injection to optimize the dynamic aperture. It is clear from the horizontal and vertical wire scans, figure 12.2, that the coupling disappeared since there is no more emittance growth in the vertical plane and in the horizontal plane the expected double peak structure appears.

The analysis of the BPM data was influenced by limitations of the BPM system. In figure 12.3 we show two typical problems: fake points and noisy pick-ups. About 20% of the pick-ups with a high noise level had to be discarded from the analysis.

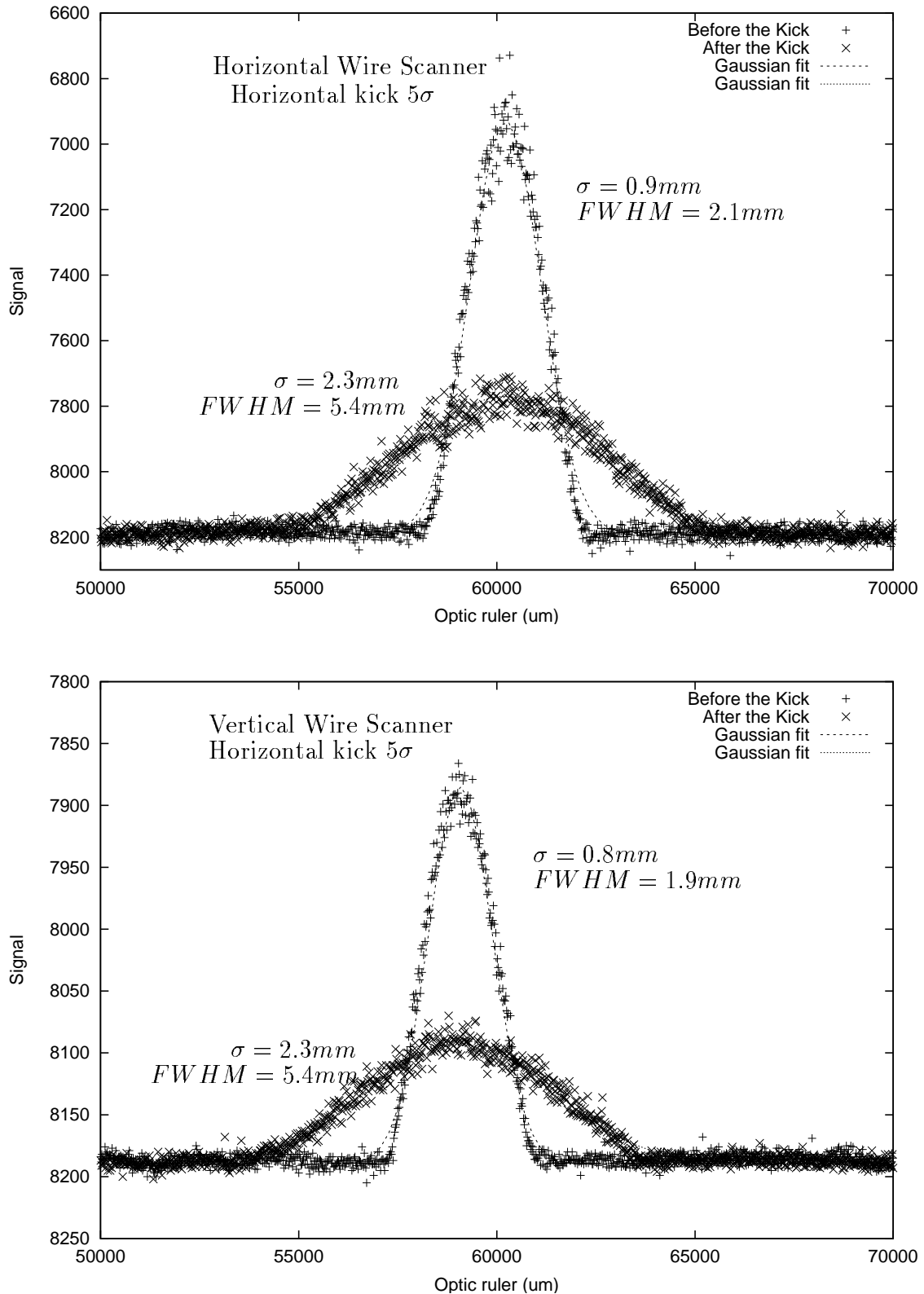


**Figure 12.1:** Horizontal (top) and vertical (bottom) wire scan before and after a horizontal kick of  $5\sigma$  for the working point  $(0.292, 0.297)$ .

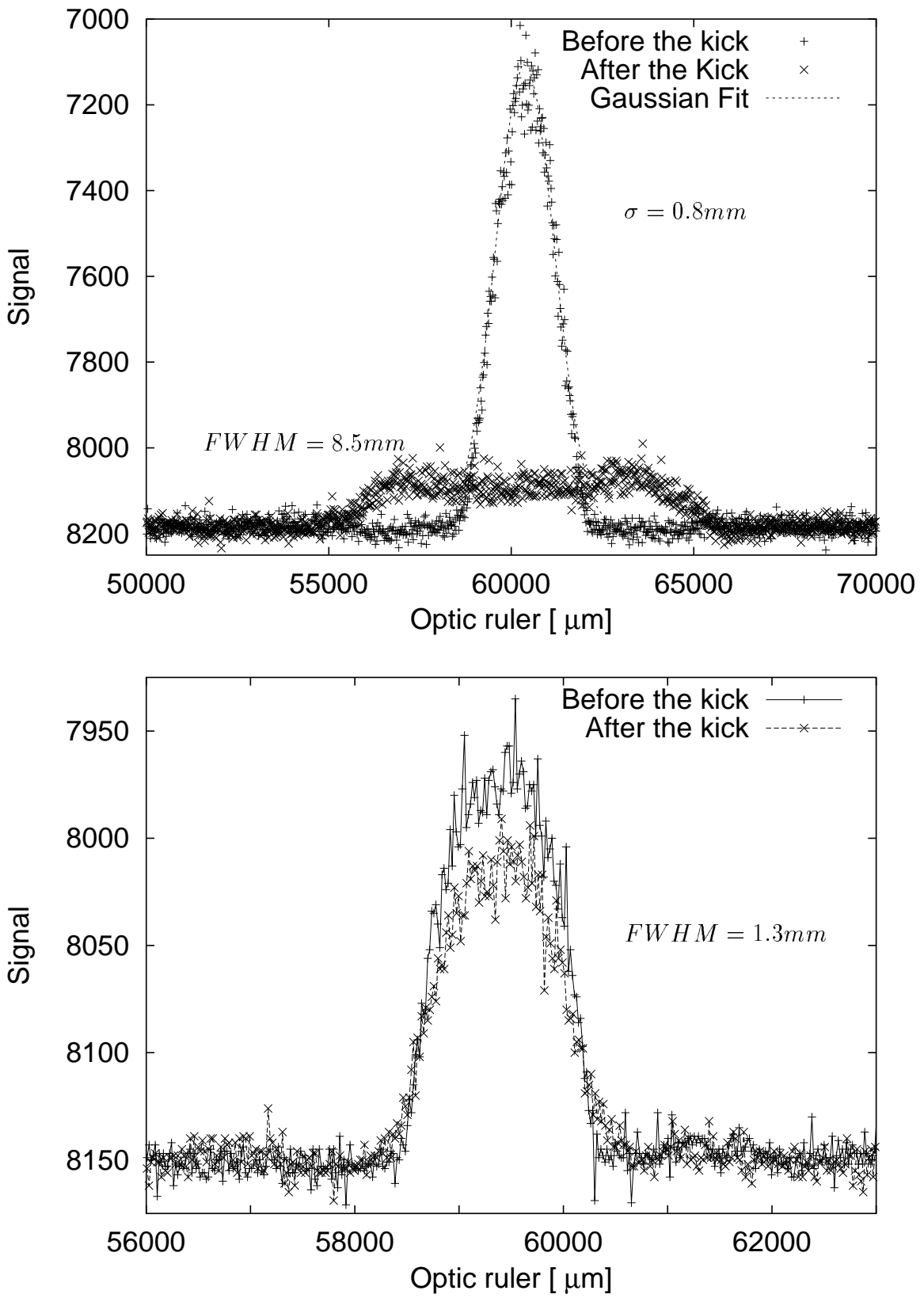


**Figure 12.2:** Wire scans before and after a kick of  $5\sigma$  in the horizontal (top) and vertical (bottom) respectively, for the working point (0.28, 0.31).

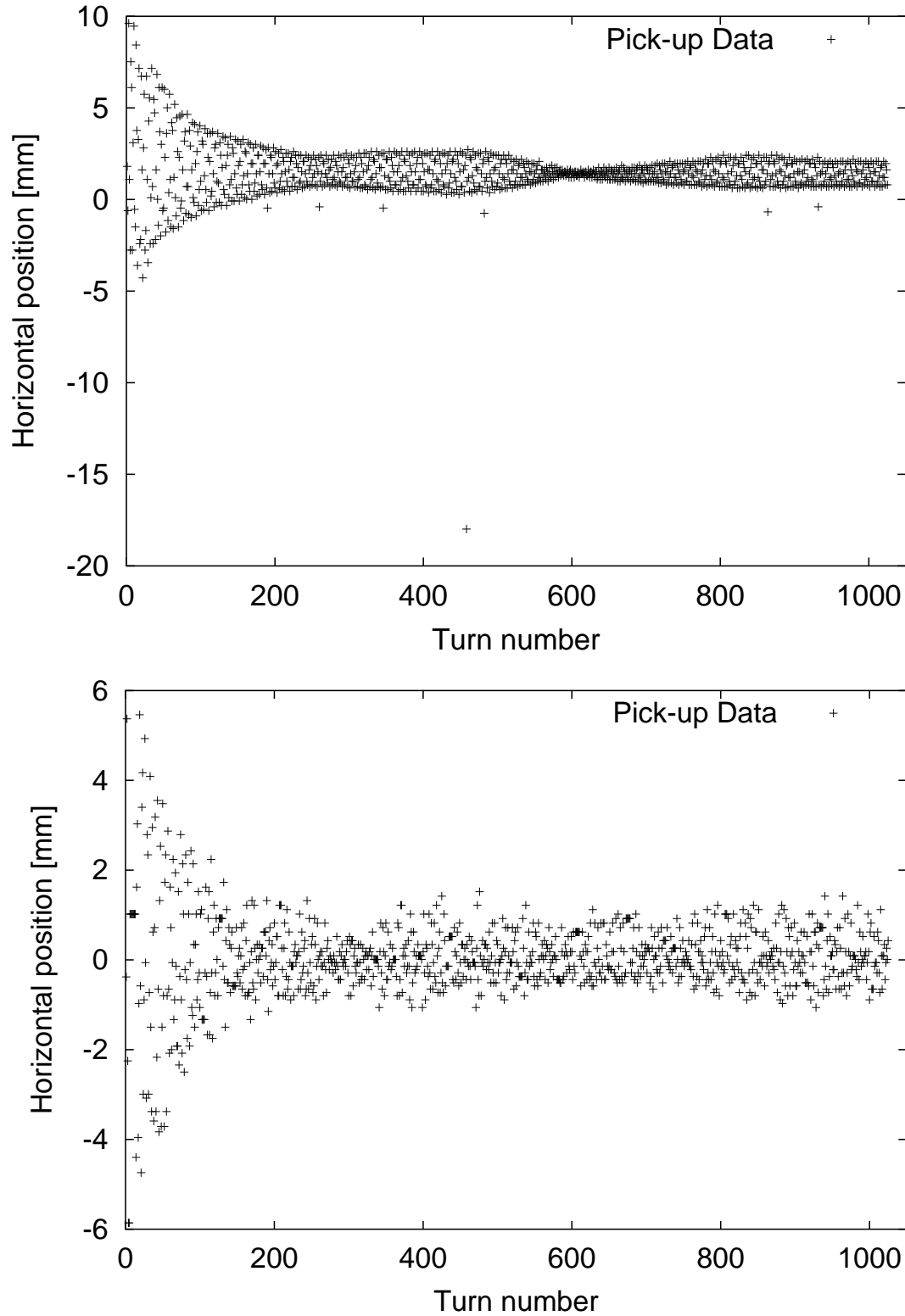


**Figure 12.3:** Example of raw data from the pick-up WR767X (top) and SR767X (bottom). The data from WR767X show occasional large excursions, e.g. turn number 450, and at SR767X the data are very noisy.

Lens	experimental results		theoretical values		% $\frac{\Delta \bar{\beta}_x}{\bar{\beta}_x}$ $\frac{\Delta \bar{\beta}_y}{\bar{\beta}_y}$	
	$\bar{\beta}_x[m]$	$\bar{\beta}_y[m]$	$\bar{\beta}_x[m]$	$\bar{\beta}_y[m]$		
QR52WEST	$72 \pm 5$	$45 \pm 3$	69.21	57.35	0.4%	20%
QR54WEST	$29 \pm 8$	$231 \pm 13$	34.93	265.5	17%	8%
QR56WEST	$196 \pm 11$	$26 \pm 4$	236.9	25.57	17%	0%
QR57WEST	$176 \pm 3$	$3 \pm 5$	177.4	14.46	0%	70%
QP58WEST	$3 \pm 4$	$95 \pm 13$	8.245	101.8	12%	7%

**Table 12.2:** Summary of measured and theoretical  $\beta$ -functions

## 12.3 Realistic model of HERA-p

### 12.3.1 $\beta$ -beating

The usual procedure for the measurement of the  $\beta$ -function was followed. Once the beam is injected we vary the power applied to single quadrupole lenses and measure the horizontal and vertical tunes. The general expression that relates the tune shift and the change in the quadrupole gradient reads,

$$\Delta Q = \frac{1}{4\pi} \int \beta(s) \Delta K(s) ds. \quad (12.4)$$

In our case, several nearby magnets are powered in series constituting a quadrupolar lens. Considering constant  $\beta$ -functions in the quadrupoles the former expression is reduced to

$$\Delta Q = \frac{1}{4\pi} \sum_{m=1}^n \beta_m L_m \Delta K_m , \quad (12.5)$$

where the sum is extended over all the magnets of which the lens is composed of ( $n$  is the number of magnets),  $K_m$  is the gradient of each magnet and  $L_m$  is its length. The different magnets of the lens are powered with the same current so we express each strength as  $L_m K_m = k_m I$  ( $k_m$  is a known calibration constant). The expression that relates the tune with the current is:

$$\Delta Q = \frac{1}{4\pi} \left( \sum_{m=1}^n \beta_m k_m \right) \Delta I = \frac{n}{4\pi} \left( \sum_{m=1}^n \beta_m \frac{k_m}{\bar{k}} \right) \bar{k} \Delta I \equiv \frac{n}{4\pi} \bar{\beta} \bar{k} \Delta I , \quad (12.6)$$

where  $\bar{k}$  is the mean value of the calibration constants  $k_m$  of the lens composed of the different quadrupoles and  $\bar{\beta}$  is the weighted average shown in the second parentheses. Of course we have to compare  $\bar{\beta}$  in the model and experiment instead of the  $\beta$  values at a single longitudinal location. This  $\bar{\beta}$  has been measured for the following lenses: QR52WEST, QR54WEST, QR56WEST, QR57WEST and QP58WEST. All of them are composed of more than one quadrupole, for example, the QR52WEST consists of two magnets of type QR and one of type QT with predicted  $\beta$ -functions

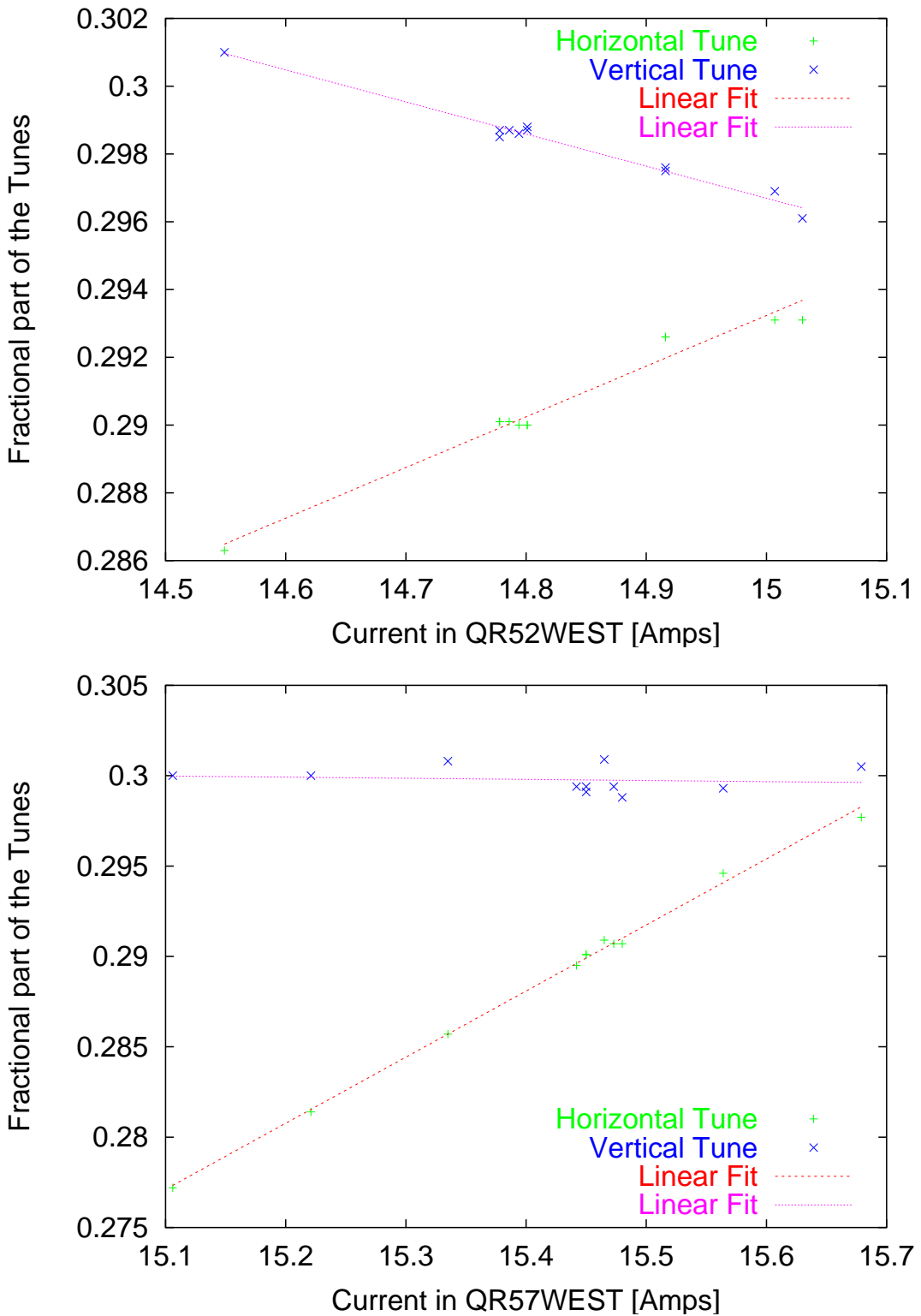


**Figure 12.4:** Fractional tunes versus current for the quadrupoles QR52WEST (top) and QR57WEST (bottom) respectively. The measured data are represented as symbols and the lines are a linear fit to the data.

at each magnet:  $\beta_{(x,y)QR1} = (69.94, 48.13)$ ,  $\beta_{(x,y)QR2} = (69.88, 60.64)$ ,  $\beta_{(x,y)QT} = (65.42, 74.95)$ . Combining all calibration curves we obtain

$$L_{QR}K_{QR} = \frac{I}{22.44 p} , \quad L_{QT}K_{QT} = \frac{I}{65.95 p} , \quad (12.7)$$

$$L_{QP}K_{QP} = \frac{I}{27.00 p} , \quad (12.8)$$

with  $I$  in [A],  $p$  in [ $GeV/c$ ],  $L$  in [m] and  $K$  in [ $m^{-2}$ ]. In figure 12.4 we show the graphs  $Q(I)$  obtained for the 2 lenses QR52WEST and QR57WEST, by plotting the horizontal and vertical tunes versus the applied current. Equation 12.6 and the appropriate calibration constants can be used to determine the values of  $\overline{\beta_x}$  and  $\overline{\beta_y}$ . In table 12.2 the measured and the theoretical values of the  $\beta$ -function are listed. As a possible measure of the precision to which the measured  $\beta$ -functions agree with the theoretical expectations, the averages and the standard quadratic deviations of the last two columns of table 12.2 are calculated to be:

$$\left\langle \frac{\Delta\overline{\beta_x}}{\overline{\beta_x}} \right\rangle = (4 \pm 7)\% , \quad \left\langle \frac{\Delta\overline{\beta_y}}{\overline{\beta_y}} \right\rangle = (11 \pm 9)\% . \quad (12.9)$$

### 12.3.2 Detuning

The machine non-linearities introduce a dependence of the tunes on the transverse oscillation amplitudes. In [31] we find complete expressions from Normal Form theory relating the tune shifts and the non-linearities. Octupolar (to first order) and sextupolar (to second order) fields produce a linear dependence of the tunes on the emittances. Since these are usually the dominant non-linearities the tune shifts can be expressed with three coefficients ( $\alpha_{12} = \alpha_{21}$ )

$$\begin{aligned} \Delta\nu_x &= \alpha_{11}\epsilon_x + \alpha_{21}\epsilon_y , \\ \Delta\nu_y &= \alpha_{12}\epsilon_x + \alpha_{22}\epsilon_y , \end{aligned} \quad (12.10)$$

where the factors  $\alpha_{ij}$  depend on the octupolar and sextupolar fields and the phases and  $\beta$ -functions at their longitudinal locations. Notice that  $\epsilon_x$  and  $\epsilon_y$  are twice

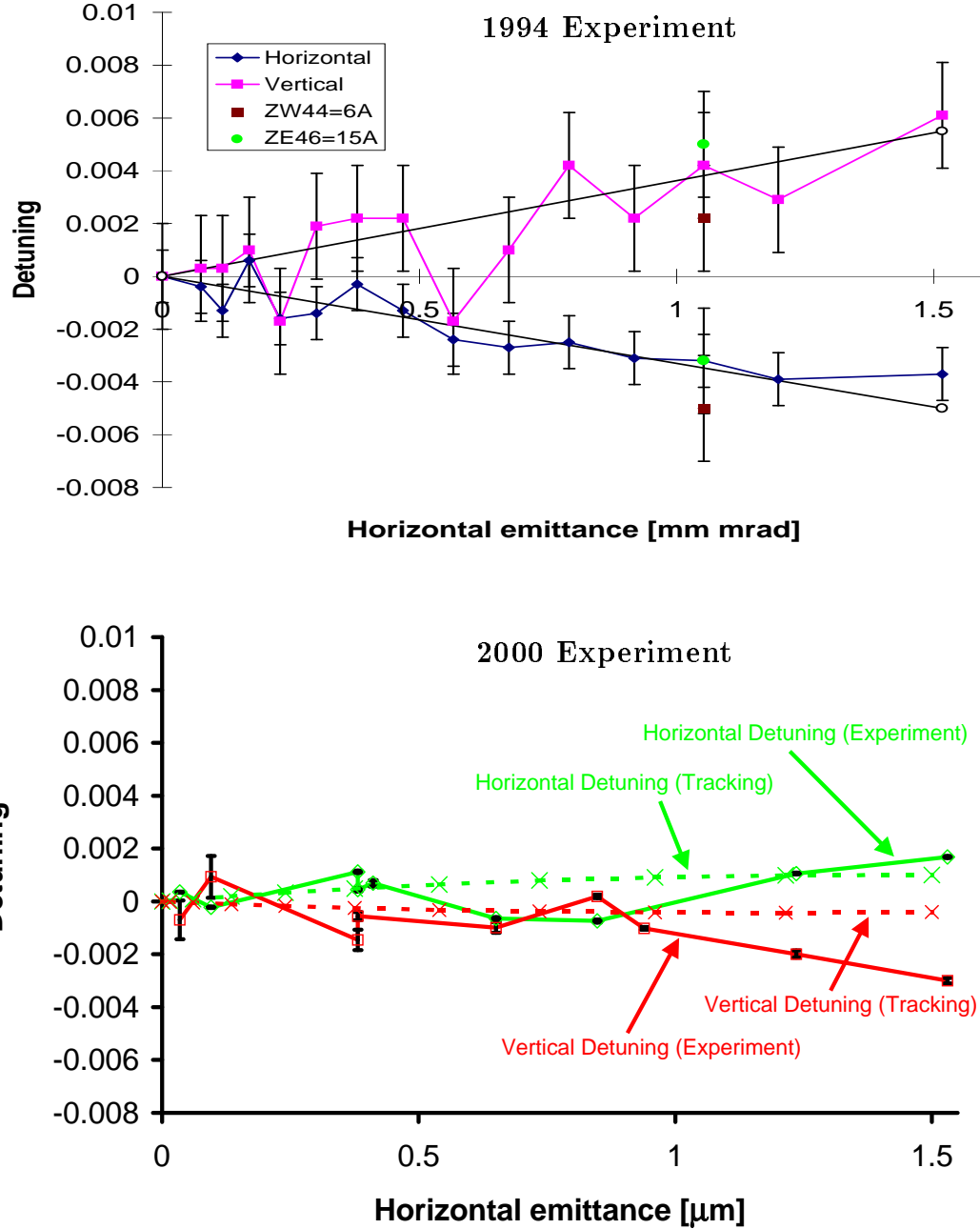


**Figure 12.5:** Detuning as a function of emittance for the HERA-p experiment in 1994 (top) and 2000 (bottom) respectively.

the linear action invariants of the single particle dynamics and are related to the oscillation amplitude  $A_n$  by the expression  $A_n = \sqrt{\epsilon_n \beta_n}$ .

The sextupolar configuration of the model has been adjusted to reproduce the measured amplitude detuning since the real sextupolar content of the machine is not exactly known. In figure 12.5 (bottom) the detuning versus amplitude is depicted for the 2000 experiment and the tracking simulations. Compared to the results from 1994 [32], figure 12.5 (top), we observe a change of sign of both, horizontal and vertical detuning as well as a reduction by roughly a factor of 5.

## 12.4 Discussion of results

### 12.4.1 Dynamic aperture study

In the experiment we found abrupt losses already at small kick amplitudes. From this we conclude that the physical aperture in the machine is too small to measure the dynamic aperture. If we assume that there exists a single fixed physical aperture responsible for the biggest part of the immediate intensity losses, one can compute the distance<sup>1</sup> from the limiting object to the centroid of the beam knowing the sigma of the beam and the intensity loss. If this assumption is correct the distance should reduce linearly with kick strength.

Considering a Gaussian beam before the kick,

$$\rho(a, \phi) = \frac{1}{2\pi} a e^{-a^2/2}, \quad (12.11)$$

where  $a = \sqrt{\epsilon_x \beta_x} / \sigma_x$ . The normalized distribution in amplitude  $a$  and phase  $\phi$  after a kick of amplitude  $Z = \beta_x \Delta x' / \sigma_x$  is

$$\rho_k(a, \phi) = \frac{1}{2\pi} a e^{-(a^2 + Z^2 - 2aZ \cos(\phi))/2}. \quad (12.12)$$

The normalized distribution after integration over the phase  $\phi$  reduces to

$$\rho_k(a) = a e^{-(a^2 + Z^2)/2} I_0(Za) \quad (12.13)$$

where  $I_0(Za)$  is the modified Bessel function of index 0. Considering an obstacle at amplitude  $a_{obs}$  (in units of sigma) all particles with  $a$  larger than  $a_{obs}$  will be lost in a few turns. The loss ratio is expressed as

$$\frac{I_{loss}}{I_{init}} = \int_{a_{obs}}^{\infty} da a e^{-(a^2 + Z^2)/2} I_0(Za). \quad (12.14)$$

From the measured loss ratio  $I_{loss}/I_{init}$  and the kick  $Z$  the obstacle amplitude  $a_{obs}$  can be calculated. In figure 12.6 the quantity  $(a_{obs} - Z)\sigma_0/\sqrt{\beta_0}$  ( $\sigma_0$  and  $\beta_0$  are values at the wire scanner) is plotted as a function of kick amplitude in units of  $[\sqrt{\mu m}]$ . As expected from the presence of an obstacle the relative distance from the center of the kicked beam to the transverse distance of this obstacle decreases linearly with kick amplitude. Notice that this relative distance is zero when kick amplitude and obstacle amplitude are equal.

The slope of the fit is  $-0.78 \pm 0.03$  and the obstacle amplitude in units of  $[\sqrt{\mu m}]$  can be taken from the figure 12.6 as

$$\sqrt{\epsilon_{x,obs}} = 1.054 \sqrt{\mu m}. \quad (12.15)$$

---

<sup>1</sup>This distance is expressed in  $\mu m / \sqrt{\beta_{obs}}$  with  $\beta_{obs}$  being the  $\beta$ -function at the unknown location of the obstacle.

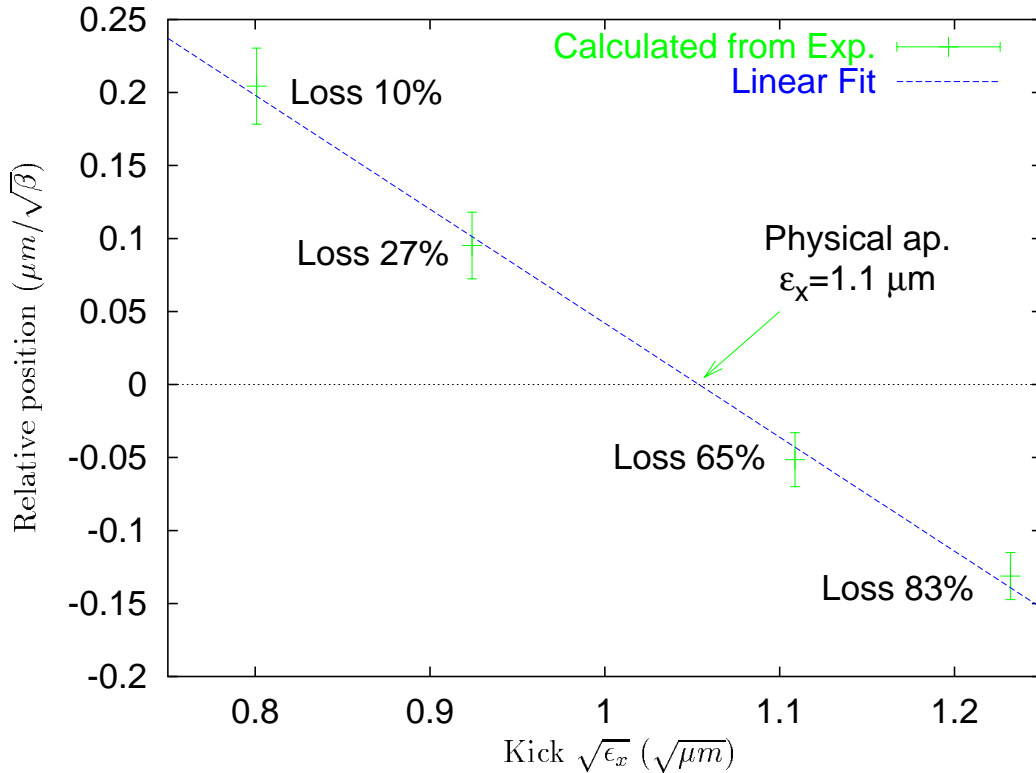


**Figure 12.6:** Calculated distance from the centroid to the obstacle to reproduce the loss versus kick. Experimental data and linear fit.

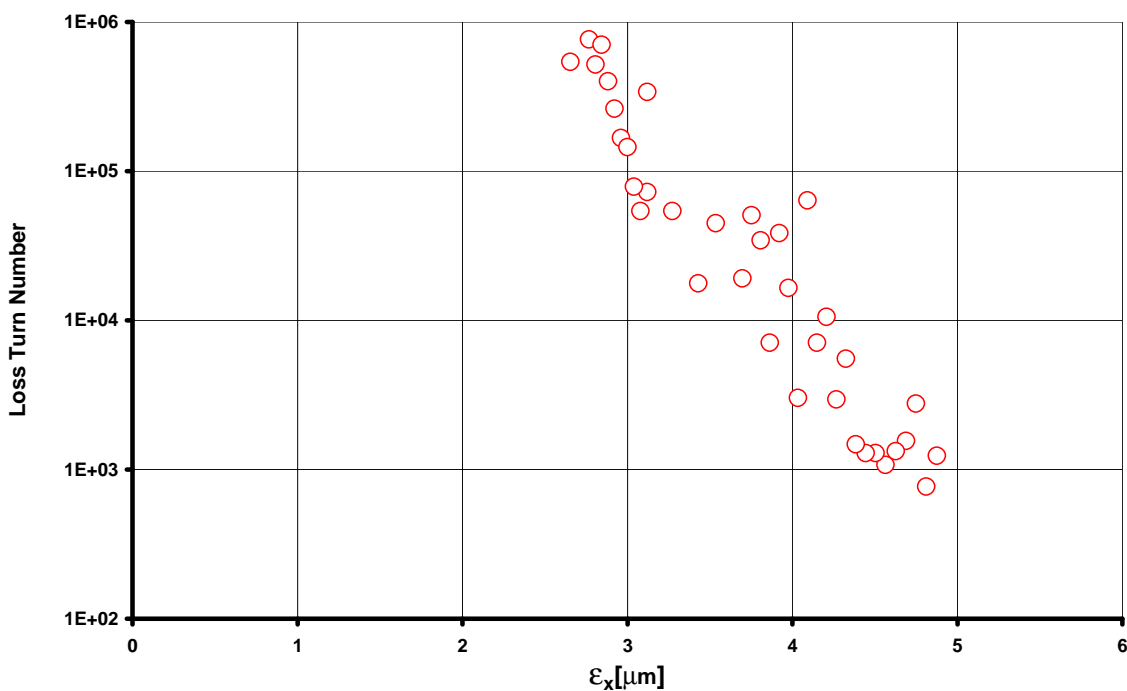


**Figure 12.7:** Survival Plot for the HERA Model in 2000.

In figure 12.7 the loss turn number is depicted versus the emittance of the particle from tracking studies. The minimum emittance without loss (called the dynamic aperture) over  $10^6$  turns or 21 [s] of store time is around  $2.6\mu\text{m}$  which is by far larger than the measured physical aperture of  $\epsilon_{x,obs} = 1.1\mu\text{m}$ .

### 12.4.2 Resonant terms

The resonance driving terms are calculated from the Fourier spectrum of the 1024 turn pick-up data. In this spectrum the lines appearing due to non-linearities will have a frequency which is the sum of integer multiples of the tunes. Moreover, as shown in reference [29] for each combination of multiples of the fundamental tunes ( $-nx, -ny$ ) there is a corresponding resonance  $(nx-1, ny)$  and  $(nx, ny-1)$  in horizontal and vertical plane respectively.

We first study the coupling resonance  $(1,-1)$  which is observable as the  $(0,1)$  line in the horizontal and  $(1,0)$  in the vertical plane. Averaging over different sets of data we find that these secondary lines are as large as 57% compared to the tune lines which indicates large linear coupling between the transverse planes.

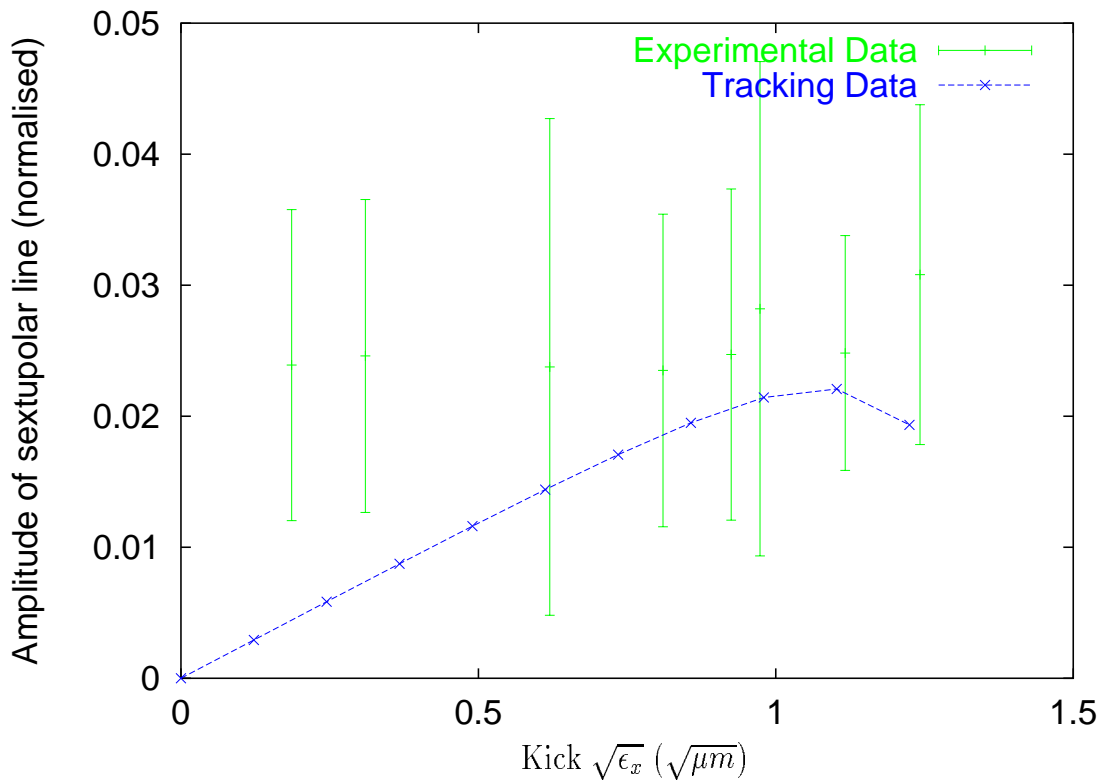


**Figure 12.8:** Amplitude of normalized  $(-2,0)$  line versus square root of emittance. The data (crosses) are shown together with their large error bars. From simulation the line with the (x) symbol is expected.

The most important line coming from the sextupolar fields of the machine in the case of horizontal plane is the line (-2,0), i.e. the (3,0) resonance. The amplitude of this line normalized to the tune line should be linear in the kick strength to first order. Figure 12.8 shows this normalized amplitude of the line (-2,0) versus the kick amplitude for the experiment and for the tracking simulations. To reduce the pick-up noise we have averaged the (-2,0) line over all reliable pick-ups and the error bars are the standard deviation of this set. The big error bars are probably due to the low resolution of the pick-ups. The measurement is therefore not very reliable in particular at small kick amplitudes. However, the measurements are not inconsistent with theoretical predictions.

## 12.5 Conclusion

In a relatively short time the machine and the beam conditions have been set up appropriately for the planned measurement. The  $\beta$ -functions have been measured at relevant places. We found that the BPM resolution was too low to measure the third order resonances with sufficient precision. Nevertheless, the experimental data are not inconsistent with the theoretical expectations.

With respect to the dynamic aperture studies we were limited by the fact that the physical aperture was too small after a standard closed orbit correction. A careful centering of the beam in the available physical aperture is mandatory to measure the dynamic aperture. In 1994 this has been done with local bumps around the machine but this year time did not permit this lengthy adjustment.

A new simulation model for the tracking has been prepared which includes all measured multipole errors. This model has been adjusted to this year's detuning which is smaller by roughly a factor of 5 compared to that of 1994. The calculated dynamic aperture is, however, not very different for both models.

It would probably be very useful to repeat these measurements after the HERA-p upgrade to optimize the dynamic aperture at injection. However, it is mandatory that more time is allocated for a good centering of beam in the physical aperture. Moreover, it should be investigated if the BPM system can be improved.

## Acknowledgments

The authors are thankful to F. Willeke for making this experiment possible, G. H. Hoffstaetter for support on site. All the colleagues, engineers, technicians and operators which were involved in the preparation and realization of the experiment are thanked for many discussions, help and their hospitality.

# 13 Energy Loss Measurement at HERA-p

by H. Burkhardt, CERN,  
U. Hurdelbrink and W. Kriens, DESY Hamburg

Date: 2000, Sept. 3, 7am to 11 pm, Logbook XLV, p. 74–78

## 13.1 Introduction

Synchrotron radiation is well known and measured for highly relativistic particles like electrons and positrons at several GeV (Lorentz factor  $\gamma$  of order several thousand). The spectrum is dominated by hard (ultraviolet or x-ray) photons, emitted in the forward direction in a narrow cone of roughly  $1/\gamma$  opening angle. The total energy loss scales as  $E^4$  or, equivalently, the relative energy loss  $\Delta E/E$  as  $\gamma^3$  (where  $\gamma$  is the Lorentz factor).

The aim of this experiment is a measurement at moderately relativistic energies ( $\gamma$  of order hundred). The synchrotron radiation at these energies is dominated by rather soft photons, corresponding to wavelengths of order mm and emitted in a larger cone. Already in 1945, J. Schwinger predicted, that the low energy spectrum of the synchrotron radiation would be suppressed due to the presence of conducting materials (like the beam pipe) [33]. The shielding of soft synchrotron radiation appears to be poorly known with little or no experimental data. Recently, it gained importance in the context of coherent synchrotron radiation for short bunches.

Measurements of the total energy loss including synchrotron radiation of moderately relativistic protons and lead ions have been performed previously in the SPS [34]. The beam was left coasting, with the radio frequency turned off. The energy loss of the debunched beam was observed as shift in revolution frequencies on a Schottky monitor. The SPS-measurements are limited in precision by a relatively poor quality and knowledge of the vacuum (of order 10e-8 mbar). It was therefore suggested to perform similar measurements at HERA-p, where the vacuum conditions are much more favorable.

## 13.2 Schottky Signal Detection

At HERA-p no dedicated longitudinal Schottky monitor is installed which could be used for an accurate measurement of the revolution frequency. But sufficient Schottky signal measurements have been performed using a standard wall current monitor [35], although this monitor has a rather poor sensitivity for an unbunched beam. The signal processing is concentrated on the 1268th revolution harmonic at 60 MHz using a crystal filter with a few kHz of bandwidth. This needs high amplification and excellent noise suppression. For spectral analysis with FFT the Schottky signal has to be down converted into the baseband and the absolute stability of the reference frequency used for this task has to be stable in the order of 1e-9 during one measurement cycle of about 2 hours.

### 13.3 Beam Preparation

In order to resolve a frequency shift from the measured spectrum, the spectral density must be high. To achieve such good signal conditions, the longitudinal emittance of the proton beam should be preserved during the injection process, the energy ramp, and during the preparation for debunching.

The coasting beam has been produced by debunching an initially bunched beam in HERA-p. The debunching procedure starts with an adiabatic reduction of the 208 MHz RF voltage down to a value matched to the 52 MHz voltage of the second RF system. Then the driving power of the 208 MHz is switched off and the cavity impedance stays compensated due to the fast feedback system. The 52 MHz voltage is now reduced also adiabatically to a value where the lifetime begins to drop. For technical reasons the 52 MHz system could not be switched off with the impedance compensation staying active. This may have an influence on the overall parasitic mode loss.

The resulting spectral distribution of the unbunched beam can be seen in the upper pictures of figure 13.1. The two curves in these pictures show the spectral distribution at the beginning and at the end of the study periods for the three different energies.

### 13.4 Revolution Frequency Measurement

Before debunching the beam, the beam spectrum at the output of the Schottky monitor was shifted into the center of the FFT frequency span by tuning a reference frequency (60 MHz) which is used for the transformation of the 1268th revolution harmonic into the baseband. The FFT frequency span is chosen from 0 Hz to +200 Hz overlapping the spectrum of the coasting beam and containing 1600 display lines resulting in a resolution of 0.125 Hz.

The frequency drift of the spectral distribution versus time is shown in the lower pictures of figure 13.1. In this case the center of gravity of the spectrum is used to define a representation for the drift.

### 13.5 Dipole Field Measurement

The revolution time of the protons depends on their energy and on the strength of the dipole field. In order to deduce the energy loss from the measured revolution frequency, one needs to take into account possible drifts of the dipole fields. At HERA such drifts are mostly due to power supply regulation and persistent currents in the super-conducting coils.

In two types of reference magnets (ZANON, ABB) NMR probes are installed for precise field measurements. The magnetic field drift as recorded by these probes is shown in figure 13.2. The ZANON values appear to be more noisy and were not available at 132 GeV. Originally it was planned to have the lowest energy at 120 GeV, but it turned out that at this energy, neither the ABB nor the ZANON probe are designed to lock at this energy. At the two higher energies, the long term drift

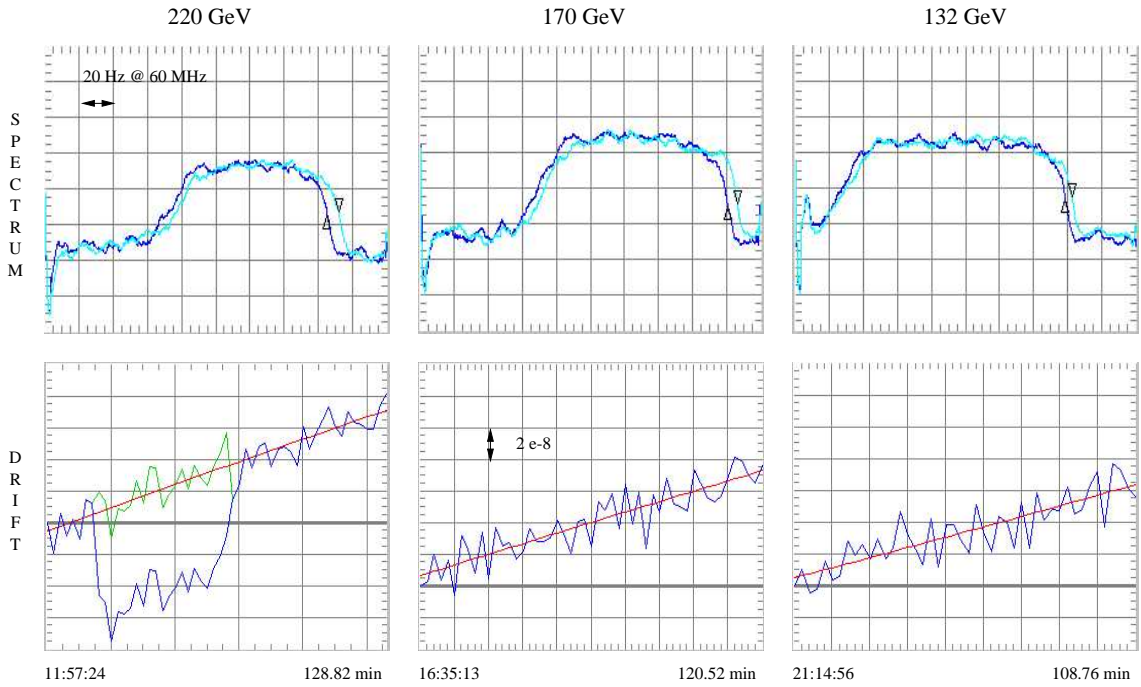


**Figure 13.1:** Schottky spectra of the unbunched beams measured at the 1268th harmonic of the revolution frequency which is about 60 MHz. The upper pictures show the spectral density in logarithmic scale (dBV) at the beginning (dark blue) and at the end of the measurement. A mean of 50 data points surrounding every display point was taken to smooth the curves. The horizontal scale is 20 Hz/div. The relative frequency drift of the spectrum (center of gravity) versus time is shown in the lower pictures. A tripping power supply for some correcting coils was the reason for a temporarily deviation from the normal drift at 220 GeV in the lower left picture. The vertical scale is 2e-8/div for all energies and the horizontal scale indicates the starting time and the duration of the measurement.

recorded by both probes looks rather similar. It appears therefore reasonable to assume, that the drift as recorded by the ABB-NMR approximately represents the change of the field integral in the whole ring.

## 13.6 Beam Energy Loss

The energy loss of the unbunched protons in HERA changes the revolution frequency to higher values. At energies above 200 GeV synchrotron radiation has the main contribution. The time dependence of the energy loss due to synchrotron radiation in free space is

$$-\frac{1}{E} \frac{dE}{dt} = 6.42 \cdot 10^{-18} [\text{m}] \cdot \frac{f_0 \gamma^3}{\rho}, \quad f_0 = 47 \text{ kHz}, \quad \rho = 584 \text{ m}, \quad (13.1)$$

where  $f_0$  is the revolution frequency and  $\rho$  is the bending radius.

The real change of the proton energy can be estimated from the measurement of the revolution frequency and the dipole field applying the following relation for the

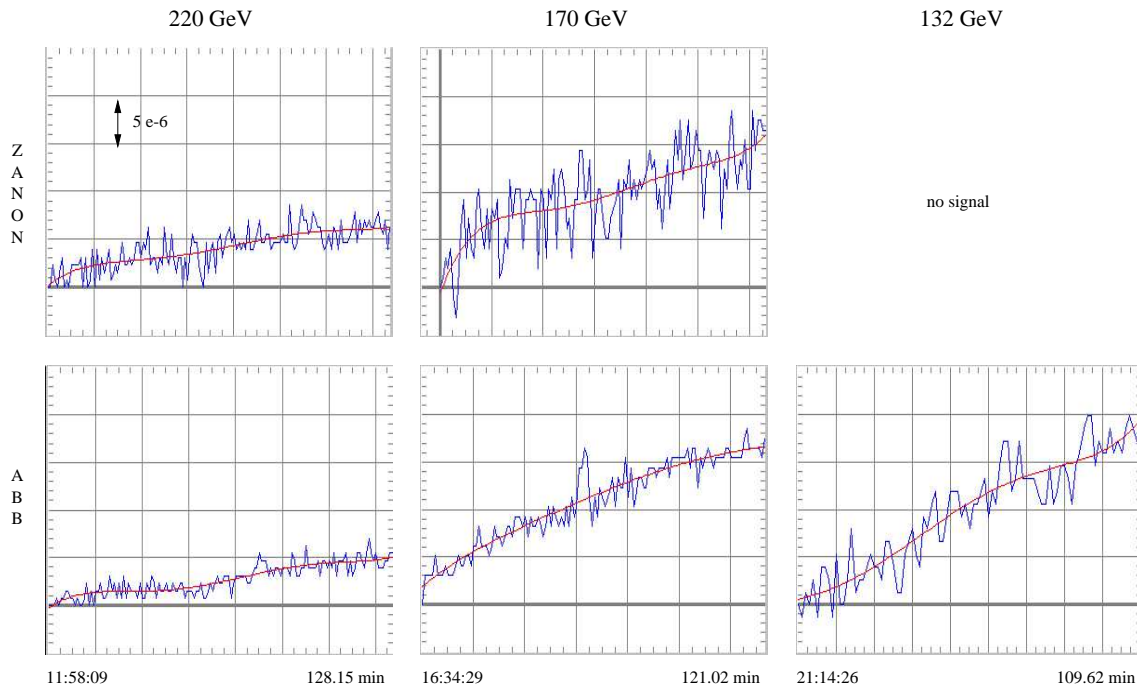


**Figure 13.2:** NMR dipole field measurements. The vertical scale is  $5e-6$ /div of relative field change for all pictures. In correspondence with the frequency measurement, the starting time and the duration is indicated at the horizontal scale. With ramp times at 7:55 at 220 GeV, 15:40 at 170 GeV and 20:09 at 132 GeV, there was much more time for persistent currents to decay at 220 GeV than at the lower energies. This matches the observation with larger drifts at the two lower energies. The ABB data are used applying a polynomial fit for representing the total drift of the HERA-p dipole fields during the measurement.

relative momentum change:

$$\frac{\Delta p}{p} = \frac{\alpha}{\eta} \cdot \frac{\Delta B}{B} - \frac{1}{\eta} \cdot \frac{\Delta f}{f}, \quad \alpha = 1.28 \cdot 10^{-3}, \quad \eta = \alpha - \gamma^{-2}. \quad (13.2)$$

With  $\alpha$  the momentum compaction factor and  $\eta$  the slip factor.

In figure 13.3 the results of the measured  $\Delta p/p$  per hour are displayed in comparison with synchrotron radiation calculated from the upper formula.

### 13.7 Conclusion

A very small but still significant energy loss of coasting protons was observed in HERA at three energies of about 132, 170 and 220 GeV. The total energy loss clearly increased with the beam energy and is compatible with being largely due to synchrotron radiation.

The complete analysis with an estimate of the energy loss by other sources (scattering on the rest gas, resistive wall losses etc) and an estimate of all systematic uncertainties is still in progress, and it will be premature to draw any definite conclusions.

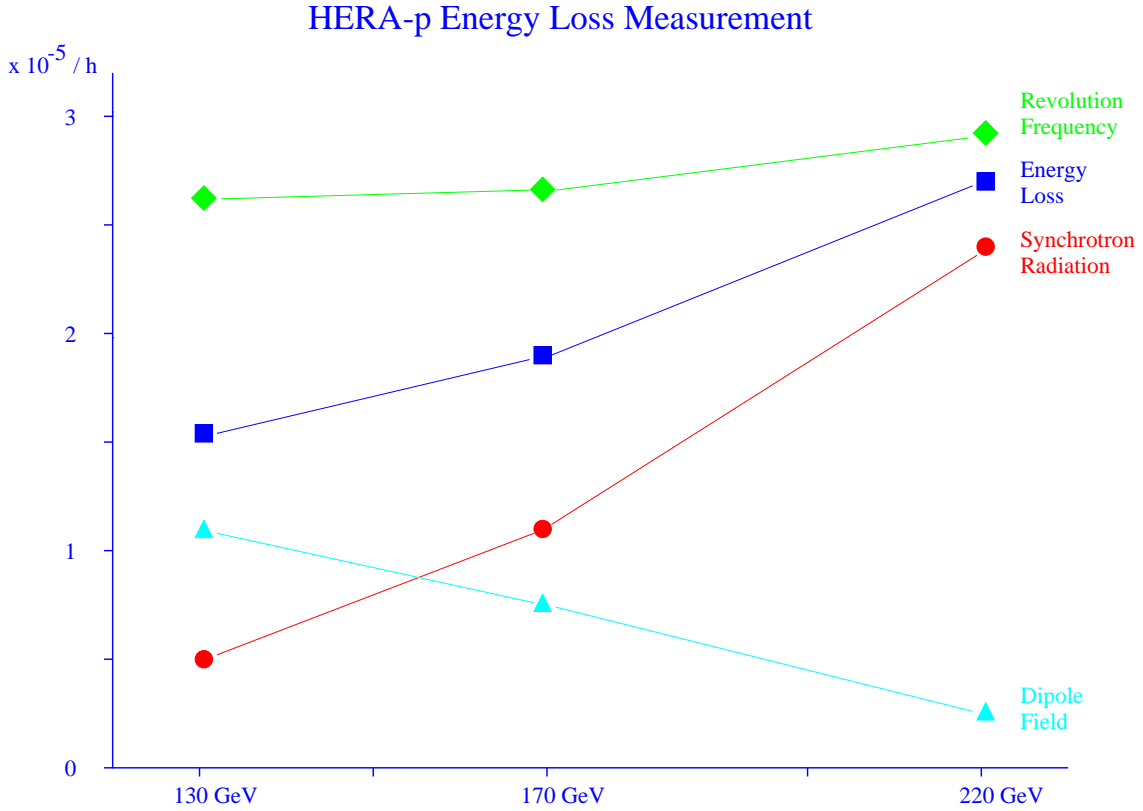


**Figure 13.3:** The measured change of the revolution frequency divided by the slip factor  $\eta$  (green top curve) and the change of the dipole field times the momentum compaction factor  $\alpha$  divided by  $\eta$  (light blue bottom curve) is normalized to one hour and displayed over the energy of the protons. The energy loss is calculated from their difference (middle blue curve). For comparison the synchrotron radiation in free space for HERA-p is also shown (red curve).

Still, it is already interesting to see in figure 13.3 that the increase in the total measured energy loss appears to be similar to the increase in free space synchrotron radiation. It will be very interesting to continue the detailed analysis and to attempt to obtain first limits on the amount of shielding.

Even if this first attempt to measure the small energy loss of the coasting beams in HERA has already been quite promising, it is also likely that the uncertainty could still be further improved by a more dedicated longitudinal monitoring and an improved magnet drift monitoring or simpler longer measurement times in particular at the lower energies.

## Acknowledgments

H. Burkhardt would like to express his thanks to the DESY HERA staff for the excellent and pleasant collaboration. The authors together would like to thank F. Willeke who kindly reserved machine time for this project and G. Hoffstaetter, M. Minty, and F. Willeke for helpful discussions.

## References

- [1] U. Schneekloth (ed.), The HERA Luminosity Upgrade, *Report DESY-HERA-98-05* (1998)
- [2] G. H. Hoffstaetter, Future Possibilities for HERA, *Proceedings EPAC2000, Vienna* (2000)
- [3] G. H. Hoffstaetter and F. Willeke, Electron Dynamics in the HERA Luminosity Upgrade Lattice of the Year 2000, *Proceedings PAC99, New York* (1999)
- [4] S. van der Meer, *CERN ISR-PO/68-31* (1968)
- [5] D. P. Barber, The generalization of the van der Meer method to include the case of bunched collinear beams, *Daresbury Nuclear Physics Laboratory, CERN Preprint* (1973)
- [6] E. Keil, Beam-Beam Dynamics, *CERN SL/94-78 (AP)* (1994)
- [7] G. H. Hoffstaetter (ed.), HERA Accelerator Studies 1999, *Report DESY-HERA-00-02* (2000)
- [8] M. Bieler, E. Gianfelice, G. Hoffstaetter, T. Limberg, M. Minty, and F. Willeke, Experiments about the Beam-Beam Effect at HERA, *in [7]* (2000)
- [9] M. Bieler, E. Gianfelice-Wendt, G. H. Hoffstaetter (ed.), B. Holzer, S. Levonian, T. Limberg, M. Lomperski, M. Minty, Ch. Montag, R. Wanzenberg, M. Wendt, F. Willeke, and K. Wittenburg, HERA Machine Studies December 1998, *Report DESY-HERA-99-03* (1999)
- [10] G. H. Hoffstaetter, New Beam Optics for HERA-e: Theoretical Investigations and Experimental Tests, *Reprot DESY-HERA-99-04* (1999)
- [11] A. Meseck, Tail Scan Experiments I at HERA-e, *in [7]* (2000)
- [12] A. Meseck, Tail Scan Experiments II at HERA-e, *in [7]* (2000)
- [13] G. H. Hoffstaetter, The Emittance in HERA-e for Different RF Frequencies, *in [9]*
- [14] J. Kewisch et al., *Phys. Rev. Letts.*, vol.62, N<sup>o</sup>4, p. 419 (1989)
- [15] D. P. Barber, M. Berglund, and E. Gianfelice, *in Proceedings of the Desy Accelerator Seminar 2000*, Grömitz 2000, in preparation.
- [16] B. Autin, Y. Marti, Closed Orbit Correction of A.G. Machines using a small Number of Magnets, *CERN ISR-MA/73-17* (1973)

- [17] Y. Alexahin, F. Brinker, G. H. Hoffstaetter, Detection of Localized Sources of Coupling and Focusing Perturbations from the Injected Beam First Turn Trajectories, *in [7]* (2000)
- [18] J. Irwin, C. X. Wang, Y. T. Yan, K. Bane, Y. Cai, F. Decker, M. Minty, G. Stupakov, F. Zimmermann, "Model-Independent Analysis with BPM Correlation Matrices", *SLAC-PUB-7863* (1998)
- [19] J. Safranek, "Experimental determination of storage ring optics using orbit response measurements", *NIM A388 p. 27-36* (1997)
- [20] C. Montag, K. Ehret, and S. Issever, Stabilization of HERA-B Interaction Rates Using Tune Modulation, *in [7]* (2000)
- [21] O. Brüning, An Analysis of the Long-Term Stability of the Particle Dynamics in Hadron Storage Rings, *Report DESY-94-085* (1994)
- [22] E. Vogel, Real Time Measurement of Single Bunch Phase and Length at the HERA Proton Storage Ring and the Observation of Multi Bunch Oscillations, *Report DESY-HERA-00-08* (2000)
- [23] A. W. Chao and M. Tigner, *Handbook of Accelerator Physics and Engineering*, World Scientific (1999)
- [24] G. Stupakov and S. Kauffmann, Echo Effect in Accelerators, *Report SSCL-587* (1992)
- [25] O. Bruening et. al., Beam Echoes in the CERN SPS, *Proceedings PAC97, Vancouver* (1997) and *Report CERN-SL-97-023-AP* (1997)
- [26] R. Wagner, private communication, DESY (August 2000)
- [27] S. Ivanov, private communication, IHEP, Protvino (2000)
- [28] E. D. Courant and H. S. Snyder, The theory of alternating-gradient synchrotron, *Ann. Phys.*, 3, pp. 1-48 (1985)
- [29] R. Bartolini and F. Schmidt, Normal Form via tracking or Beam Data, *Report: LHC Project note 132* (revised December 1999), and *Part. Accelerators 59*, pp. 93-106 (1998), and <http://wwwslap.cern.ch/frs/report/lines97.ps.Z>
- [30] F. Schmidt, SIXTRACK Version 3, Single particle tracking code treating transverse motion with synchrotron oscillations in a Symplectic manner, *Report: CERN/SL/94-56 (AP)* (1994)
- [31] J. Bengtsson and J. Irwin, Analytical Calculations of Smear and Tune Shift, *Report: SSC-232* (1990)

- [32] O. Brüning, W. Fischer, F. Schmidt and F. Willeke, A Comparison of Measured and Calculated Dynamic Aperture of the HERA Proton Ring at Injection Energy, *Report: CERN SL/95-69 (AP)*, and *Report: DESY-HERA-95-05* (1995), and <http://wwwslap.cern.ch/frs/report/dyna94.ps.Z>
- [33] J.Schwinger, On Radiation by Electrons in a Betatron, Preprint from 1945, transcribed by M. A. Furman in 1998, available from <http://www.lbl.gov/~miguel>, *Report LBNL-39088 and CBP Note-179* (1998) burkhardt98
- [34] J. Arnold et al., Energy Loss of Proton and Lead Beams in the CERN-SPS, *Proceedings PAC97, Vancouver*, pp. 1813–1815 (1997)
- [35] W. Kriens, M. Minty, Longitudinal Schottky Signal Monitoring for Protons in HERA, *Proceedings EPAC00, Wien* (2000)